LASER SURFACE TEXTURING OF BIOMATERIALS: FROM CONCEPTUALIZATION TO IMPLEMENTATION

Afif Batal

A thesis submitted to the University of Birmingham for the degree of

Doctor of Philosophy

December 2020

Department of Mechanical Engineering

School of Engineering

College of Engineering and Physical Sciences

The University of Birmingham

ABSTRACT

Laser surface modification and more specifically laser surface functionalization is widely being considered as a way to efficiently give the surfaces of innovative high value products added or enhanced surface properties. The technology offers a number of desired advantages over competing technologies, of which: selectivity, relatively high processing speeds and the absence of waste or harmful by-products. Nevertheless, the full range of potential applications and suitable target materials is not yet explored, and some feasibility and implementation challenges remain open-ended concerns. With the limited literature available on laser surface texturing of cobalt chrome alloys, a prevalent implant material, the research presented in this thesis aims to address the suitability of this technology in that context and compare it with the current state-of-the-art in the orthopaedics industry. Furthermore, the transferability of the laser surface texturing process from 2D planar test samples to actual 3D parts will be assessed and the effects of 3D laser processing disturbances on the surface functionality evaluated. Finally, a method for laser processing complex surfaces productively is presented and validated on additively manufactured spherical parts.

ACKNOWLEDMENTS

I would like to dedicate the first few words of my thesis to everyone that made it possible. A huge thank you goes to my supervisor, Professor Stefan Dimov, without whom none of this would have come to be. His tremendous support and guidance during the past 6 years both as boss and as mentor were indispensable for ‘carrying out the work’. I would also like to thank my second supervisor Dr Rachel Sammons and my colleagues in both the schools of engineering and dentistry at the University of Birmingham.

I would not have been able to accomplish this feat without the encouragement, laughs and love of my friends, old and new. To my best friend, confidant and colleague, Antonio (Tony) García Girón, Birmingham would have been a much greyer place without you. To our many adventures and discussions, whether in the UK, Spain or Slovenia (and to many more to come). I would like to express my warmest appreciation to Anabel, her beautiful soul and our numerous introspective, long, friendly debates (*están todas apuntadas en mi libreta)*. A special thanks to my Lebanese mates, Nahil and Hiba, the life of every party and source of all shenanigans. My sincere gratitude goes to all the wonderful friends, companions, pals and partners I made along the way, namely, Maritina, Andrea, Ane, Deyala, Ermano, Davide, Irene, Giovanni, Aleksandra, Hannah, Pavel and Tahseen. A heartfelt thanks also goes to the original gang scattered all over the globe: Majd, Hasan, Hassib, Ramzi, Waddah and Haytham, in the hope of reuniting in Beirut someday.

I would also like to show my genuine appreciation to Ilaria Bernardi for reminding me of the beautiful side of life far from science and academia and for being such an inspiration. *Grazie per la musica*.

Last, but in no means least, I am grateful for my supportive and loving family who stood by me through thick and thin. Randa, Moustapha, Dana (froo), Jana, Sima and Kayan no words can express what you mean to me. This thesis is dedicated to you, بحبكن .

TABLE OF CONTENTS

LIST OF TABLES

Chapter 2

Chapter 3

Chapter 4

Chapter 5

LIST OF FIGURES

Chapter 1

Chapter 2

Chapter 3

Chapter 4

Chapter 5

LIST OF ACRONYMS

LPBF	Laser Powder Bed Fusion
AM	Additive Manufacturing
LST	Laser Surface Texturing
LIPSS	Laser Induced Periodic Surface Structures
LP	Laser Polishing
FOD	Focal Offset Distance
BIA	Beam Incidence Angle
FoV	Field of View
SEM	Scanning Electron Microscope
AFM	Atomic Force Microscope
FV	Focus Variation
B	Blasted
P	Polished
NT	Nano-textured
FS	Femtosecond
NS	Nanosecond
HA	Hydroxyapatite
RTQ	Removal Torque

LIST OF PUBLICATIONS AND PRESENTATIONS

The following publications and conference presentations are a result of the research carried out during the thesis.

Journal article publications

- Batal, A., Michalek, A., Penchev, P., Kupisiewicz, A., & Dimov, S. (2020). Laser processing of freeform surfaces: A new approach based on an efficient workpiece partitioning strategy. International Journal of Machine Tools and Manufacture, 156, 103593..
- Batal, A., Michalek, A., Garcia-Giron, A., Nasrollahi, V., Penchev, P., Sammons, R., & Dimov, S. (2020). Effects of laser processing conditions on wettability and proliferation of Saos-2 cells on CoCrMo alloy surfaces. Advanced Optical Technologies, 9(1-2), 67-78..
- Batal, A., Sammons, R., & Dimov, S. (2019). Response of Saos-2 osteoblast-like cells to laser surface texturing, sandblasting and hydroxyapatite coating on CoCrMo alloy surfaces. Materials Science and Engineering: C, 98, 1005-1013.

Conference presentations

- Industrial Laser Symposium (ILAS), Crewe UK, March 2019 (Presentation)
- World Congress on Micro and Nano Manufacturing (WCMNM), Portorož Slovenia, September 2018 (Presentation)
- CIRP Design Conference, Cranfield UK, May 2017 (Presentation)
- The European Society for Precision Engineering and Nanotechnology (euspen), Nottingham UK, June 2016 (Poster)

Other publications as co-author

- Piccolo, L., Sorgato, M., **Batal, A.**, Dimov, S., Lucchetta, G., & Masato, D. (2020). Functionalization of Plastic Parts by Replication of Variable Pitch Laser-Induced Periodic Surface Structures. Micromachines, 11(4), 429.
- Garcia-Giron, A., Romano, J. M., **Batal, A.**, Michałek, A., Penchev, P., & Dimov, S. S. (2020). Experimental investigation of processing disturbances in laser surface patterning. Optics and Lasers in Engineering, 126, 105900.
- Nasrollahi, V., Penchev, P., **Batal, A.**, Le, H., Dimov, S., & Kim, K. (2020). Laser drilling with a top-hat beam of micro-scale high aspect ratio holes in silicon nitride. Journal of Materials Processing Technology, 281, 116636.
- Michalek, A., Qi, S., **Batal, A.**, Penchev, P., Dong, H., See, T. L., & Dimov, S. (2020). Sub-micron structuring/texturing of diamond-like carbon-coated replication masters with a femtosecond laser. Applied Physics A, 126(2), 144.
- Masato, D., Sorgato, M., **Batal, A.**, Dimov, S., & Lucchetta, G. (2019). Thin-wall injection molding of polypropylene using molds with different laser-induced periodic surface structures. Polymer Engineering & Science, 59(9), 1889-1896.
- Garcia-Giron, A., Romano, J. M., **Batal, A.**, Dashtbozorg, B., Dong, H., Solanas, E. M., ... & Dimov, S. S. (2019). Durability and wear resistance of laser-textured hardened stainless steel surfaces with hydrophobic properties. Langmuir, 35(15), 5353-5363.
- Bhaduri, D., Penchev, P., **Batal, A.**, Dimov, S., Soo, S. L., Sten, S., ... & Dong, H. (2017). Laser polishing of 3D printed mesoscale components. Applied Surface Science, 405, 29-46.

CHAPTER 1: INTRODUCTION

1.1 Motivation

Laser-based surface modifications have attracted significant interest from both industry and research in recent years. The technology allows new surface properties to be “imprinted” on substrate materials, in particular to improve their inherent surface properties or integrity, i.e. surface roughness, hardness and residual stresses. The surface modifications mechanisms achievable through laser processing, involve changes in surface topography, microstructure, chemistry or possible combinations of them. The surface functionalities investigated and reported by researchers include hydrophobicity/hydrophilicity, antifouling/antibacterial, improved tribological properties and osteoconductivity (bone cells growth and proliferation on the surface), to name a few.

Laser processing offers several advantages over other competing technologies such as chemical etching and conventional machining, especially when used as a surface modification technology. First, there are no limitations in regard to the type of materials that can be processed, from refractory metals, to polymers, ceramics and even transparent materials such as glass. Second, it is a selective process and therefore the technology can be employed to “imprint” surface properties only where they are needed. Third, being a non-contact and a very flexible material processing method, the technology is a cost-effective alternative to conventional and other non-conventional machining technologies which suffer from high cost of tooling and other consumables [1, 2]. Fourth, laser processing does not involve any material wastage (the material is directly evaporated or sublimed), unlike chemical (e.g. etching),

abrasive (e.g. blasting) or conventional machining processes (e.g. milling) where by-products can be harmful or time consuming and expensive to recycle.

Orthopaedics is a particularly interesting application area for laser surface modifications. Having no residues, by-products or requiring harmful chemicals, it could be easier for the developed laser processing solutions to get the necessary regulatory approvals and thus to be implemented in practice quicker. Furthermore, taking into account their potential to improve implants' osseointegration and anchorage, laser processing could reduce the need for painful and costly implant revisions and thus improve patients' quality of life. Finally, the technology could become a viable alternative to widely-used coating solutions such as hydroxyapatite. Especially, coatings have several limitations such as: a relatively high cost associated with their applications; can lead to potential failures at the interfaces (delamination); the technology is energy intensive and not environmentally friendly; add one more processing step to the production process; and usually the coating operations are subcontracted to dedicated service providers. Therefore, the potential elimination/bypassing of this addition processing step would lead to functional, environmental, and economic advantages.

Laser surface modification processes such as texturing or polishing have been extensively researched on planar samples in order to assess their capabilities in laboratory environments, where they have been properly validated and well characterised. However, taking this technology commercially and applying it to real complex parts is not a trivial task and requires further research; the transferability of the process from 2D to 3D needs to be quantified and solutions for 3D processing need to be developed and optimised accordingly. Especially, most implant designs are characterised by flowing curves and planar surfaces are rare as shown in Figure 1.1.

Figure 1.1 Total knee replacement courtesy of Johnson & Johnson Medical Devices Companies

1.2 Research aims and objectives

The overall aim of this research is to investigate the capabilities and limitations of laser surface modification processes, namely Laser Surface Texturing (LST) and Laser Polishing (LP), when applied on biomaterials, specifically cobalt chromium and titanium alloys. In particular, the reported PhD research investigates: 1) the processes in “ideal” conditions on planar samples, ie. In-focus at normal beam incidence; 2) assesses the capabilities of different LST strategies and laser sources when applied on biomaterials; 3) quantifies the transferability/application of LST processes onto 3D surfaces; and 4) proposes a methodology to efficiently apply laser surface modification ‘recipes’ onto complex parts.

The aim of this PhD research is achieved through the following objectives:

1. Investigate the biological (Saos-2 cells proliferation) and wetting properties of LST surfaces and compare them with those achievable after polishing, blasting and hydroxyapatite (HA) coating when applied on a surgical cobalt chromium molybdenum alloy (CoCrMo). Especially, 3 different LST approaches were investigated: microgrooves produced with nanosecond (ns) pulsed lasers, microgrooves produced with femtosecond (fs) pulsed lasers and bioinspired sub-micron textures produced with femtosecond pulsed lasers.
2. Investigate the influence of 3D processing disturbances on the resulting surface topography and functionality of sub-micron LST patterns on CoCrMo substrates. Specifically, Laser Induced Periodic Surface Structures (LIPSS) on CoCrMo substrates are investigated to analyse and quantify the effects of 3D processing disturbances, i.e. Focal Offset Distance (FOD), Beam Incident Angle (BIA) and initial surface quality, on LIPSS profiles, surface wettability and Saos-2 cells proliferation. In addition, interdependences and potential correlations between surface wettability and biological performance are studied.
3. Develop a generic methodology for applying laser surface modifications, e.g. LST and LP operations, on complex parts and freeform surfaces. Especially, an efficient patching method based on commonly used surface tessellation algorithms is proposed. The method employs 3D processing tolerances (max FOD & max BIA) as input parameters to efficiently partition 3D surfaces into laser processing fields. Finally, a pilot application of the proposed method is conducted where it is implemented for LP and LST additively manufactured spherical Ti-6Al-4V parts.

1.3 Thesis Organisation

Chapter 1 outlines the motivation behind the work, its potential impact and provides an overview of the research aims and objectives, and finally presents the thesis organisation.

Chapter 2 reviews the state of the art in the relevant research fields which this thesis builds upon, i.e. laser material interactions, laser surface modifications, laser processing of complex shapes and more.

Chapter 3 reports an investigation into the functional responses of surfaces processed with 3 different LST methods. The results are compared to the performance of the current state-of-the-art, i.e. blasting and HA (hydroxyapatite) coating. The advantages and limitations of investigated LST approaches are discussed.

Chapter 4 reports an investigation into the influence of 3D processing disturbances, i.e. FOD, BIA and initial surface quality, on resulting LIPSS on CoCrMo alloy substrates and their added functionality. The use of wettability as a means for predicting the biological performance of biomaterials is discussed. too.

Chapter 5 proposes a novel method for partitioning complex surfaces into laser processing fields based on commonly used surface triangulation algorithms while 3D processing tolerances (max FOD & max BIA) are employed to drive the surface tessellation process. A pilot application of the method for laser polishing and texturing 3D printed spherical parts is reported to demonstrate its capabilities.

Chapter 6 summarises the contributions to knowledge, highlights the main conclusions of this research and finally discusses potential future research directions.

References

1. Bigot, S., Nestler, J., Dorrington, P., & Dimov, S. (2011). A costing methodology for products based on emerging micro and nano manufacturing technologies. Micro and Nanosystems, 3(3), 254-262.
2. Dimov, S., Brousseau, E. B. J. P., Minev, R., & Bigot, S. (2012). Micro-and nano-manufacturing: Challenges and opportunities. Proceedings of the Institution of Mechanical Engineers, Part C: Journal of Mechanical Engineering Science, 226(1), 3-15.

CHAPTER 2: LITERATURE REVIEW

2.1 LASER

Light Amplification by Stimulated Emission of Radiation, or LASER, has been an integral technology in modern society since its invention in 1960 by Theodore H. Maiman [1]. It found numerous applications in physics, chemistry, medicine and manufacturing. Due to laser's unique properties of which monochromaticity and high spatial coherence [2], it is indispensable in many scientific advances such as the Laser Interferometer Gravitational-Wave Observatory (LIGO) for instance [3]. Laser is also indispensable to spectroscopy, where most of our knowledge about the structure of atoms and molecules comes from [4].

Laser sources are commonly classified by their respective gain mediums. Active laser mediums can be gas, liquid and solid, they affect the laser's wavelength tuning potential, pulse generation, achievable output powers and energy consumption. Alternatively, lasers can be classified by their central wavelength, commonly ranging from hundreds of nanometres up to a few microns, or by their emission duration i.e. pulse duration (femtosecond, picosecond, nanosecond, and millisecond) or continuous wave [5].

In manufacturing, laser offers many advantages over other subtractive machining processes such as milling, WEDM or abrasive waterjet. First, it is an unconventional process, or non-contact, thus tooling cost is minimal [6, 7]. Second there are no limitations to the types of materials that can be processed (insulators, polymers, transparent, ceramics…) [8]. Third, it is a clean process with no resulting by-products or waste material. Fourth, laser spots can be a few microns in size, and they are accurately controlled using galvanometer scanners, thus allowing the machining for

extremely small feature sizes in the order of microns [9]. Therefore, laser processing setups have become an integral tool in advanced manufacturing labs and shop floors [10].

For the previously mentioned advantages and for its accurate selectivity, laser surface processing is the technology of choice when it comes to surface modification, as it will be shown in the following sections. Surface modification allows for the embedment of new properties that are foreign to the underlying substrate material or the enhancement of existing properties. This can be achieved using laser by changing the surface chemistry (oxidation) [11], the material's microstructure (grain refinement) [12], the surface topography (patterning) or some combination of them [13].

2.1.1 Basic principles

Laser ablation or photoablation is the process of material removal by laser beam irradiating. When a target material absorbs laser energy, it heats, melts and finally evaporates or sublimates. The process of ablation is much dependent on the laser beam and the target material. The laser parameters affecting ablation are mainly the laser power level, the irradiation exposure time (pulse duration or continuous wave), wave polarization and the central wavelength of the laser source.

The irradiation exposure time is a crucial parameter that determines the ablation regime and resulting part quality. Long exposure such as continuous wave mode or longer pulse durations in the order of millisecond result in a thermal ablation process characterised by high heating, heat affected zone (a region in the material affected by the rapid heating and cooling resulting from the laser ablation, characterised by surface discoloration and grain refinement), melting, a recast layer (recast molten material that resolidifies on the surface) and micro cracks whereas short exposure

time such as ultrashort pulses result in direct sublimation of the target material and none of the heat related downsides, hence it is known by the term ‘cold ablation’ (Figure 2.1).

In machining, the differences in the ablation regimes is manifested in increased amorphization and induced stress when using nanosecond pulses as opposed to femtosecond, when processing silicon wafers [14]. In metals, Mathew et al. showed that a femtosecond laser showed no sign of HAZ, or recast molten material as opposed to a nanosecond source when machining molybdenum. Moreover the shorter pulse duration resulted in a much better surface finish at 0.187 µm Ra as opposed to 1.89 µm using nanosecond pulses when machining the same dimension groove [15]. When processing polymers, Shibata highlighted that the use of femtosecond pulses may lead to the dissociation of the C=O bonds and also results in a more pronounced change in the polymer’s crystallinity when compared to nanosecond pulses, which didn’t alter the polymer’s composition as much. This was mainly explained by the two-photon absorption manifested in femtosecond laser processing [16].

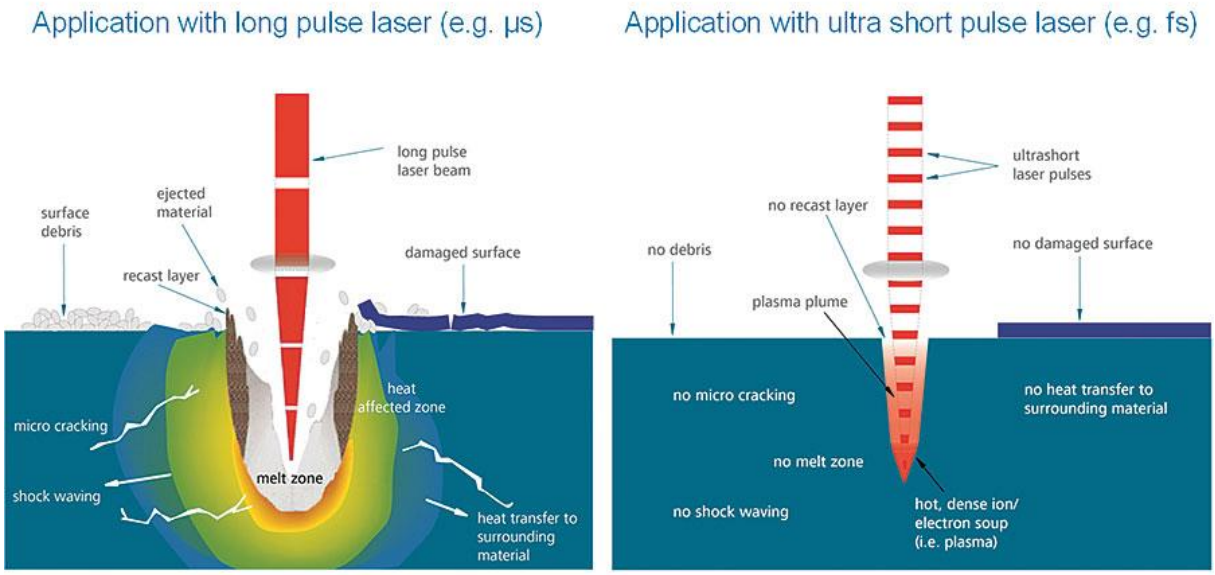

Figure 2.1 Schematic of laser-matter interaction for short and ultrashort pulse durations [17]

However, ablation is a two-way relationship and is heavily dependent on the target material as well. Different elements reflect, absorb, transmit and scatter different laser wavelength differently thus affecting the ablation process and the resulting part's quality and accuracy. Therefore careful consideration should be made when choosing a laser source based on the required processing task and target material, this also explains the trend towards smaller laser wavelengths as they are better absorbed by the majority of engineering materials as shown in Figure 2.2 [18].

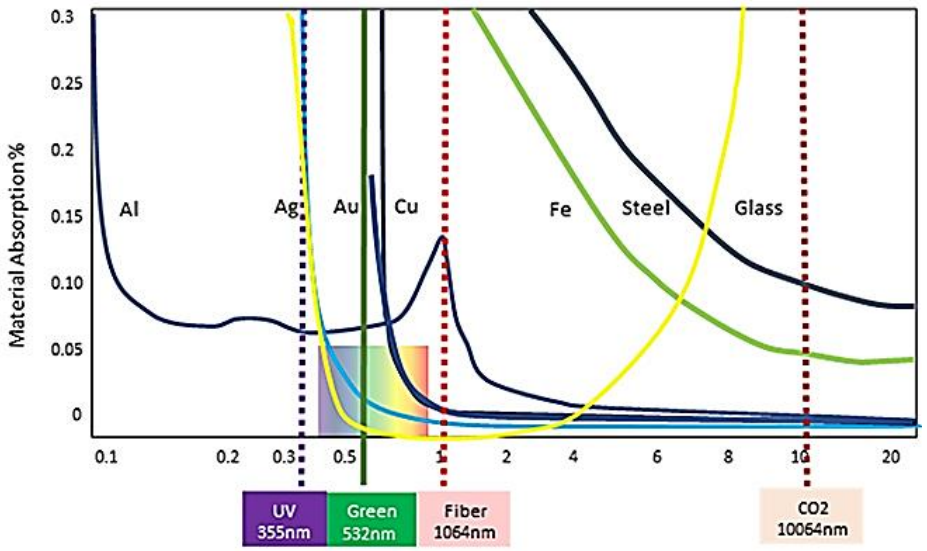

Figure 2.2 Absorption of common materials vs. wavelength courtesy of Control Laser Corporation

2.1.2 Beam delivery and machining setups

Laser processing setups are extremely modular and vary in complexity and cost. Nevertheless, the basic principles still apply, the laser beam should travel from the source to the part, where one or the other or both are moved in order to process large areas. However, a number of components can be added along the way for more control on the ablation process and for improved overall efficiency.

(i) Optical mirrors are the most used optical element in laser processing setups, choosing the right type is crucial for the performance, quality and reliability of the process. The type of coating will depend on the laser source's wavelength and exposure duration, they can be metallic (gold, copper), dielectric (magnesium fluoride, silicon dioxide) or ultrafast amongst others [19].

(ii) Depending on the quality of the beam coming out from the laser source and the length of the beam path, a collimator might be needed to ensure minimal

beam divergence, and therefore to ensure the process performance. This is typically done using a single aspheric lens.

(iii) A beam expander, either Keplerian (convergent image) or Galilean (divergent image) telescope, might be added to a laser processing system in order to control the spot size, and therefore the laser fluence and processed feature size [20].

(iv) For added control on the ablation process, a beam polarizer can be installed to modify the wave polarization. Changing the laser polarization can have effects on the material removal as well as the crater shape [21].

(v) For some applications, changing the beam intensity profile to top-hat or donut-shaped can be beneficial. For such applications a laser beam shaper based on the spatial phase modulation of the wave is fitted to the beam path [22].

(vi) In order to efficiently and rapidly process 3D parts, a dynamic focusing module (DFM), or Z module, can be included for the dynamic repositioning of the focal plane, thus the laser can be focused along the varying surface heights of the workpiece. DFMs can be in designed in 2 configurations: a translating optic which moves coaxially along the optical beam path, which can be either convergent or divergent to avoid focusing inside the beamline, especially in higher power systems [23] (Figure 2.3).

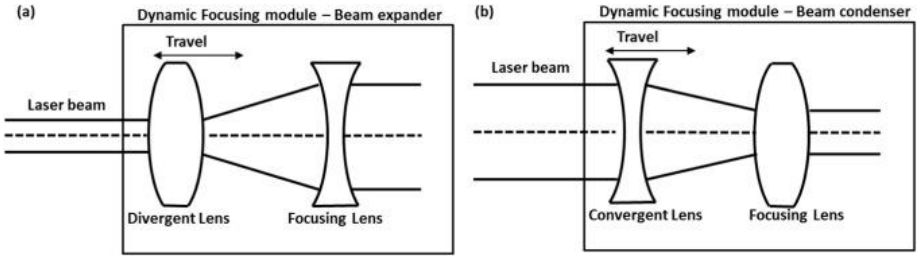

Figure 2.3 DFM configurations: (a) beam expander DFM and (b) beam condenser DFM

(vii) Prior to the focusing lens, a galvanometer scanner, or X-Y scan head is used to deflect the beam in 2 linear motions X and Y over the surface of the workpiece. Essentially those scanners are composed of motorized low-inertia mirrors, giving them tremendously high speeds and incredible accuracy and precision. For higher speeds and throughputs, new developments in polygon scanning technologies allow for scan speeds of up to 100m/s.

(viii) The final optical element in common laser setups is a focusing lens, which focuses the laser intensity in a small spot for ablation to occur. Common focusing lenses are F-theta which have a planar image field and produce a linear displacement, i.e constant scan rate. They are suitable for most laser scanning applications, but they can be upgraded to telecentric lenses which focus the beam normally to the working surface regardless of the input beam angle.

(ix) The last piece of any laser setup is the workpiece holding and positioning system. They usually consist of a stack of mechanical stages, typically, 3 linear stages X, Y and Z along with 2 rotary stages A and C. With achievable accuracy and repeatability of under 0.2 μm, although slower than optical

beam movement, mechanical stages are crucial for high precision micro scale manufacturing.

In Figure 2.4 an example is given of a modular laser processing setup typically used in research.

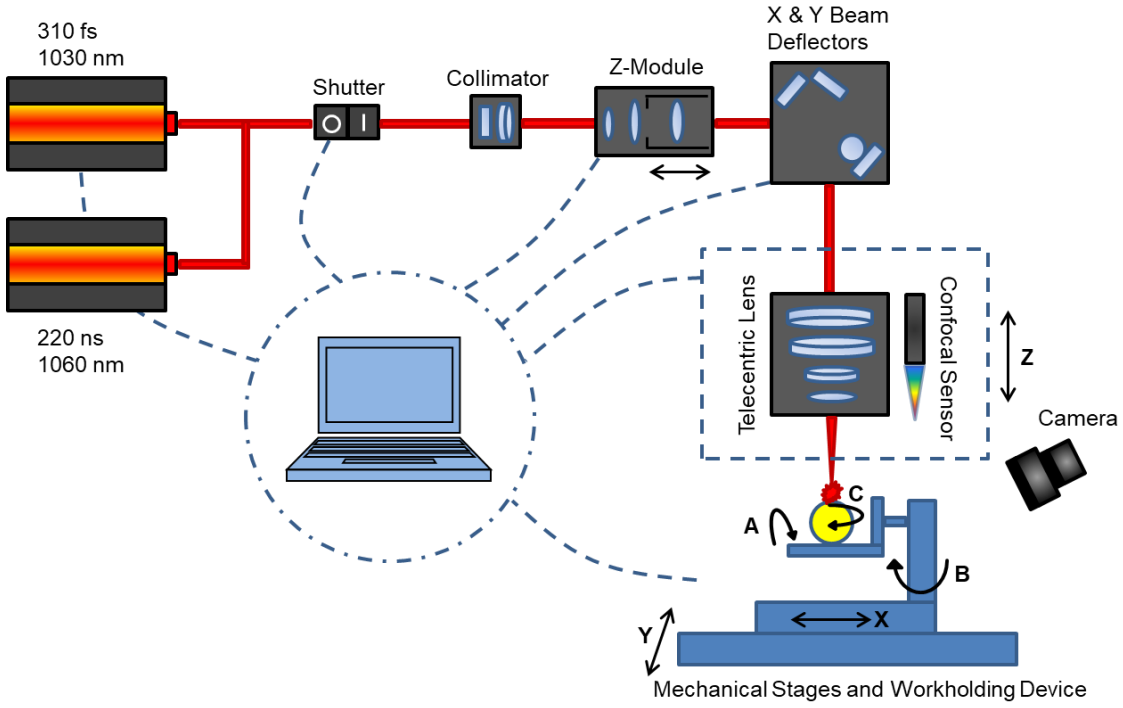

Figure 2.4 Example of modular laser processing setup [24]

2.2 Surface functionalization

Surface functionalization has become integral to the design of innovative products, especially to differentiate them from the competition by giving them added functionalities. The advantages of using laser technology for this type of applications were highlighted in section 2.1. Although laser surface processing provides many advantages over other material processing technologies, to be adopted by industrial manufacturers, it has to be capable of matching the performance of commercially used coatings while being economically viable. The performance of the technology is

dependent on the specific coating/laser process as well as the desired surface property. However, the economic viability of laser surface processing is constantly improving as the initial cost of laser systems is continuously decreasing, as shown in Figure 2.5 [25]. Moreover, when used in conjunction with mass production processes such as injection moulding, laser surface processing becomes a highly appealing addition to any process chain. For example, several researchers have already demonstrated the production of high-volume textured polymer parts with hydrophobic surface properties [26-28]. It is also worth noting that although the use of coatings is widely spread, they are several limitations associated with their broad use, those include high manufacturing costs and potential failures at the interface (delamination) [29].

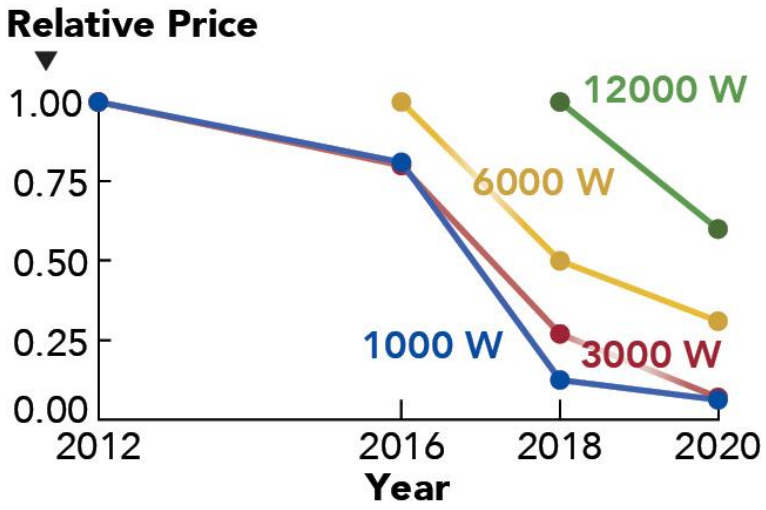

Figure 2.5 The price trend for fibre lasers sold in China courtesy of Industrial Laser Solutions

2.2.1 Surface properties

Surface engineering or modification is the addition or enhancement of certain surface properties of a material independently of its underlying substrate. The applications may be in diverse areas and can be aesthetic, optical properties, wettability, corrosion resistance or tribological to name a few [30]. In this section, we will go through some

of the latest developments in some of the most common application areas of surface engineering.

(i) In tribology, surface engineering is used to reduce the friction coefficient of the surfaces of engineering components. This is used to reduce part wear as well as improve the efficiency of mechanical systems. According to Holmberg et al. approximately 23% of the world's total energy consumption originates from tribological contacts [31], hence the great importance of tribology research. Ezhilmaran et al. reported that textured piston rings (micro dimples) using a pulsed nanosecond laser exhibited a friction reduction of up to 69% under high loading conditions [32]. In another study, Vlădescu et al. have shown that micro scale pockets produced with an ultraviolet fibre laser exhibited up to 70% reduced friction in reciprocating sliding when compared with non-textured specimens [33].

(ii) Optical characteristics of surfaces can be purely aesthetic such as logos, decorative design, product information [34] or more functional such as counterfeit protection and diffractive optical elements like Fresnel Zone Plates (FZP). Jwad et al. proposed a low-cost method to fabricate FZPs on titanium coated glass by selective oxidation using a nanosecond fibre laser source (Figure 2.6) [35]. Hermens et al. produced diffractive elements (potential applications in counterfeiting protection) on freeform surfaces by manipulating the orientation of laser induced periodic surface structures, or LIPSS [36].

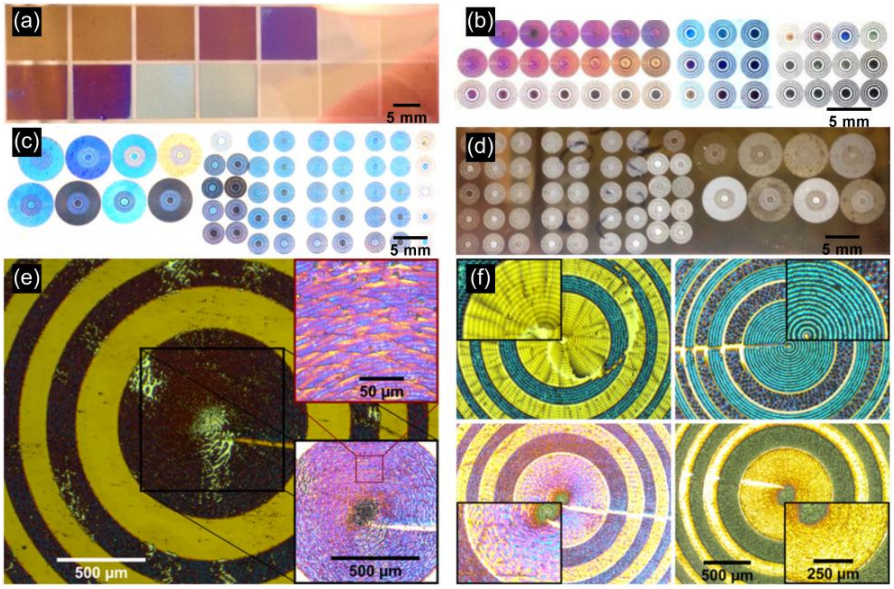

Figure 2.6 FZPs fabricated with the direct nanosecond laser writing: (a) fields associated with different TiO2 thicknesses; (b) and (c) lenses fabricated for a range of wavelengths with different combinations of TiO2 thicknesses; (d) the back view of the sample shown in (c); (e) microscopic image of the FZP lens, which performance was analyzed; and (f) microscopic images of lenses with defects/shortcomings [35]

(iii) The wettability of a surface characterises its interaction with a liquid. The first studies on wettability were published back in 1805 by Thomas Young [37]. In 1936, Young's equation was modified by Robert Wenzel to consider the roughness of the surface adding the factor *r*, defined as the true area of the solid compared to its nominal [38]. In 1944, Cassie and Baxter extended the effect of roughness on the contact angle where the liquid does not penetrate the asperities and leaves air gaps, resulting in more hydrophobic surfaces [39]. This physical phenomena is particularly interesting and can lead to interesting application areas such as self-cleaning surfaces [40], anti-icing surfaces [41] and can act as a predictor of the biological performance of biomaterials [13]. Ranella et al. has shown that the adhesion of fibroblast cells on silicon surfaces can be tuned by

changing surface chemistry and roughness, it appeared that cells had a general tendency of adhering to more hydrophilic surfaces [42]. Whereas other researchers identified an optimal CA value where cell adhesion is maximum and falls off away from this value, the CA values were 70 and 64° respectively for [43] and [44]. Jin et al. produced super-hydrophobic (water contact angle > 160 °) on polydimethylsiloxane (PDMS) surfaces (Figure 2.7) using laser etching (micro-channels and Nano roughness) by method of replication [45]. Trdan et al. studied the time dependency of wetting properties on laser textured (micro-channels) stainless steel. A strong correlation was found between water repellence and corrosion resistance [46].

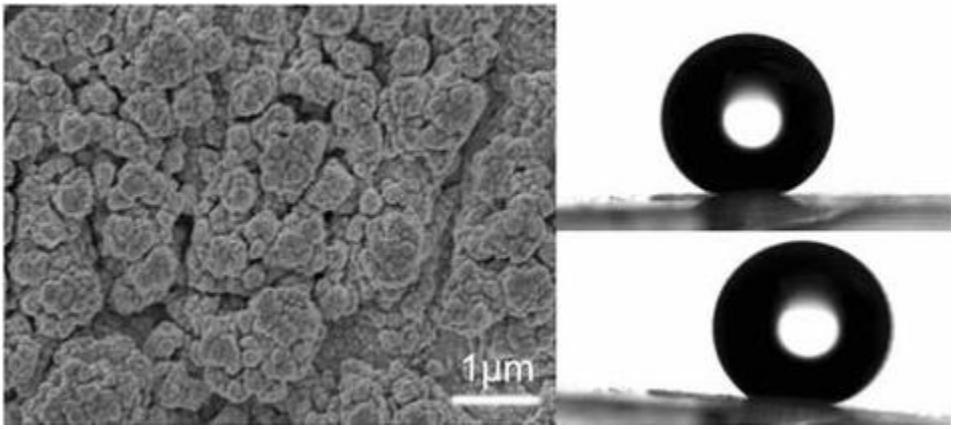

Figure 2.7 Etched PDMS surface containing micro-, submicro-, and nano-composite structures shows a self-cleaning effect with water CA as high as 162° and SA lower than 5° [45]

(iv) The biological performance of biomaterials is characterised by the surface's osteoinductive, osteoconductive and anti-bacterial properties. Osteoinduction is the process by which osteogenesis (the transformation of immature cells into bone cells, ie. osteoblasts) is induced, osteoconduction is the ability of bone to grow on a surface [47] and finally antibacterial properties refer to the surface's ability to inhibit biofilm formation and growth.

Irradiating titanium specimens with a blue-violet semiconductor laser source have shown to improve the surface's osteoconductivity and antibacterial properties [48]. More recently, Balla et al. reported that surface melting of medical grade 316L stainless steel using an Nd:YAG laser resulted in improved proliferation of human fetal osteoblast cells as well as enhanced corrosion resistance, making laser surface modification a potential treatment of medical implants [49].

Table 2.1 Highlight of main surface properties and achievable improvements with laser

Surface property	**Type of laser texture**	**Achieved Improvements**	**Reference**
Friction reduction	Micro pores	69% reduction	[32]
	Micro pockets	70% reduction	[33]
	Scale-like microstructures	80% reduction	[50]
Hydrophobic	Micro channels + nano roughness	> 160° CA	[45]
	Micro/nano protrusions	153° CA	[51]
	Micro roughening	155° CA	[52]
Hydrophilic	Micro grid pattern	< 12° CA	[53]
	Micro grid pattern	< 60° CA	[54]
	Micro honeycomb structure	< 5° CA	[55]
Osteoconduction (bone cell growth)	Nano roughening	> 20% improvement	[56]
	Micro grooves	> 13% improvement	[57]
	LIPSS	> 170% improvement	[58]
Anti-bacterial (growth suppression/adhesion reduction)	Micro grid pattern	> 93% adhesion reduction	[59]
	Micro/nano roughening	> 30% adhesion reduction	[60]
	LIPSS	> 99% adhesion reduction	[61]

2.2.2 Different laser methods for surface functionalization

(i) The first and most common method for functionalising a surface is by changing its topography, ie. introducing a sort of pattern or texture. This can be done at a meso, micro or even nano scale with lasers. For instance, Lu et al. compared different mesoscale (>100 μm) patterns' performance in terms of friction and wear reduction on chromium alloys. It was observed that a micro-grid pattern achieved the highest wear rate reduction at 57% following reciprocating sliding using silicon nitride balls [62]. At a micro scale different interactions can be achieved from a surface, for example Garcia-Giron et al. demonstrated that super-hydrophobic surfaces can be created by producing micro-scale grooves (~30 μm width and 10 μm depth) on carburised, nitrided and untreated stainless steel specimens using a nanosecond near infrared fibre laser source [63]. When irradiating a work piece with a linearly polarized femtosecond laser source in air, laser-induced periodic surface structures (LIPSS) form on the surface of the target material, and they generally have a spatial periodicity close to the laser wavelength λ [64] (Figure 2.8). The length-scale of those structures is particularly interesting to a variety of applications, but especially biological ones.

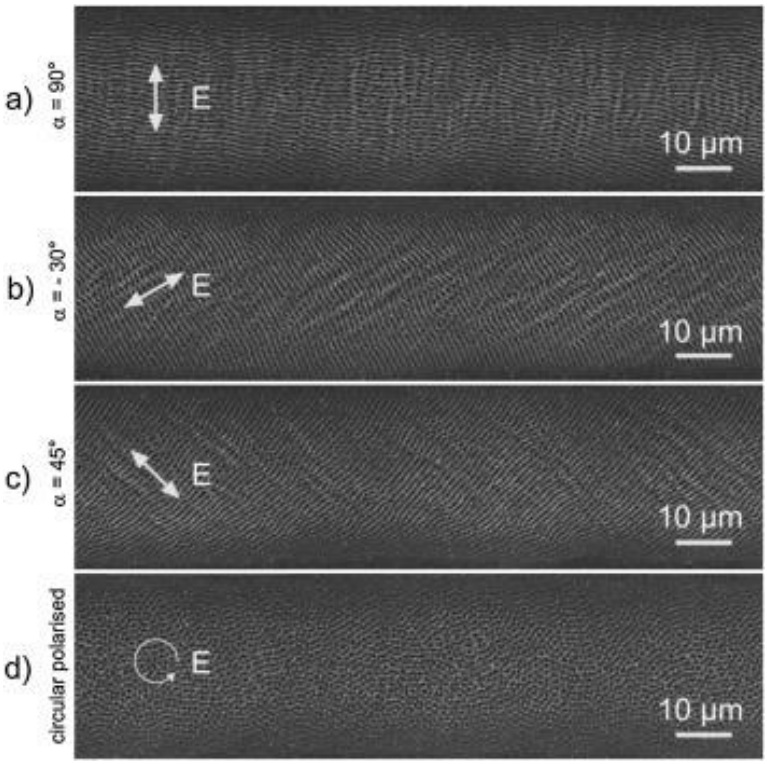

Figure 2.8 Polarization dependence of LIPSS on polished stainless steel surfaces, λ=1025 nm [65]

Epperlein et al. demonstrated that LIPSS with a periodicity of 700 nm produced on stainless steel using a Ti:sapphire femtosecond laser with a central wavelength λ=790 nm gave the surface anti-adhesion properties when *Escherichia coli* K12 was colonized on the steel samples. It was also shown in the same study that *Staphyolococcus aureus* favors LIPSS-treated areas for colonization [66]. Therefore, the response of the surface can be tailored based on the structure as well as the specific organism (Figure 2.9).

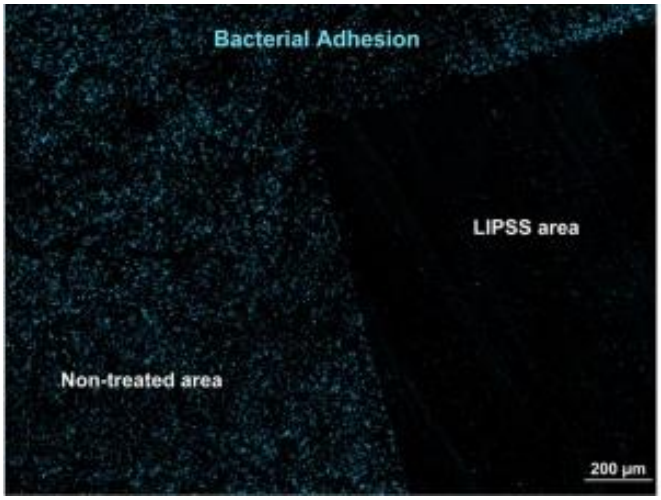

Figure 2.9 Fluorescence microscope images of samples colonized with E. coli. [66]

(ii) The second approach to alter the surface properties is by changing its chemistry using laser irradiation. In polymers this can be due to the breaking up of specific bonds and ablation of certain groups while in metals this is generally attributed to surface oxidation as shown in the following examples. Pazokian et al. exhibited that polyethersulfone (PES) films treated with a nanosecond argon fluoride (ArF) laser, λ=193 nm, below the target material's ablation threshold, result in a change in the surface chemistry, in particular, a new polymer group (C=O group) forms on the surface. This change in surface chemistry is associated with an improvement in the PES films' biocompatibility; a reduced number of blood platelets adhered on the laser treated surfaces [67]. Another example in surface chemistry change is surface oxidation. Jwad et al. proposed a novel method to colour the surface of titanium to a high resolution by producing titanium oxide using a nanosecond fibre laser to a high degree of spatial and thickness control. This method allows for the printing of highly detailed intricate images (Figure 2.10) [11].

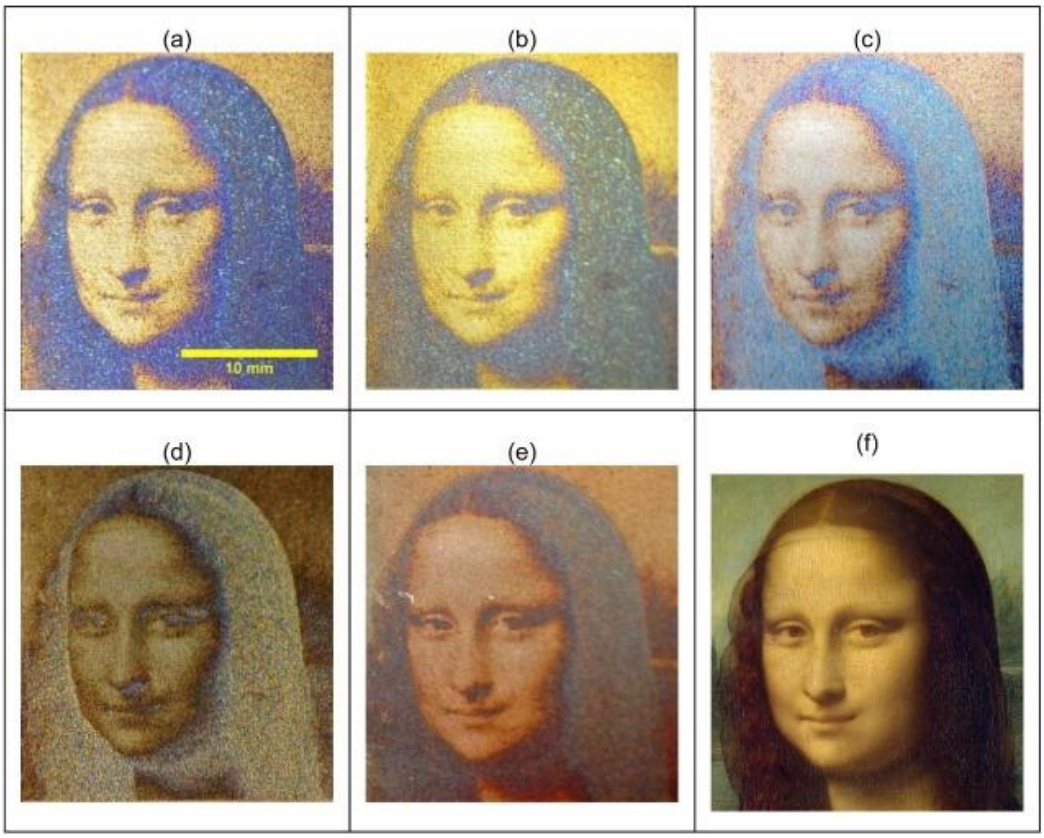

Figure 2.10 Imprinted image shown in different incident and azimuthal angles. (a) Both normal, (b) different incident, (c–e) different azimuthal angles, while (f) is the original image [11]

(iii) Finally, the last method for functionalising surfaces using laser sources is by triggering material changes in the sub-surface. When milling BS EN ISO 4957–X40CrMoV5-1 tool steel with a nanosecond laser source for instance (λ=511 nm, P=10 W, τ= 17 ns), a grain refinement is triggered up to a depth of 50 μm from the surface due to localized heating and its quick dissipation into the bulk. The change in microstructure translated into an improvement in surface micro hardness, up to 3.8 times the original value measured on the untreated specimen [12]. Alternatively, irradiating metallic parts with high energy laser beams can relieve them from negative tensile residual stresses and instead induce beneficial compressive stresses that limit crack propagation and improve fatigue life [68]. Kalentics et al. used Laser Shock Peening (LSP) to treat selective laser melted

(SLM) stainless steel parts, a maximum compressive residual stress of 798 MPa was observed at a depth of 247 μm from the surface when irradiating the part with an Nd:YAG laser with the following parameters: 532 nm wavelength, 7.1 ns pulse duration, 1mm spot diameter, 80% pulse overlap and a power density of 7.2GW/cm^2 [69].

2.3 Laser for applications in orthopaedics

Now that we went over the different applications of laser surface modification, including biological, as well as the different methods of functionalising surfaces with lasers, in this section we will examine how those come together when applied in orthopaedics. In particular, the state of the art in laser treatment of implants will be highlighted below.

In 2003 Cho et al. tested the removal torque (RTQ, an indication of an implant's attachment/anchorage to the bone) of laser treated screw-shaped pure titanium implants and compared their performance with that of machined implants. The laser treatment strategy was a micro scale roughening process yielding a surface resembling a honeycomb structure characterised by micro-pores 25 μm in diameter and 20 μm deep. Eight weeks after the implants were placed in rabbits' tibia the removal torque was measured and was 23.58±3.71 N.cm and 62.57±10.44 N.cm for the machined and laser treated implants respectively [70]. The reason behind the substantial improvement in performance of the laser treated implants is the enhanced mechanical interlocking from the micro-pores as well as the increased bone/implant contact area.

More recently in 2019, Park et al. compared the performance of hydroxyapatite (HA) blasted pure titanium implants with that of laser treated ones in rabbits femurs. The

laser modification was once again surface roughening using an Nd:YAG laser, resulting in a uniformly porous surface (Figure 2.11). The implants' removal torques measured were 24.0±10.2 N.cm and 46.6±16.4 N.cm for the control and laser treated specimens respectively [71]. Removal torques can be interpreted as biomechanical indicators of osseointegration of implants. Therefore, it can be said that laser surface modification may be used to improve the osseointegration of titanium implants.

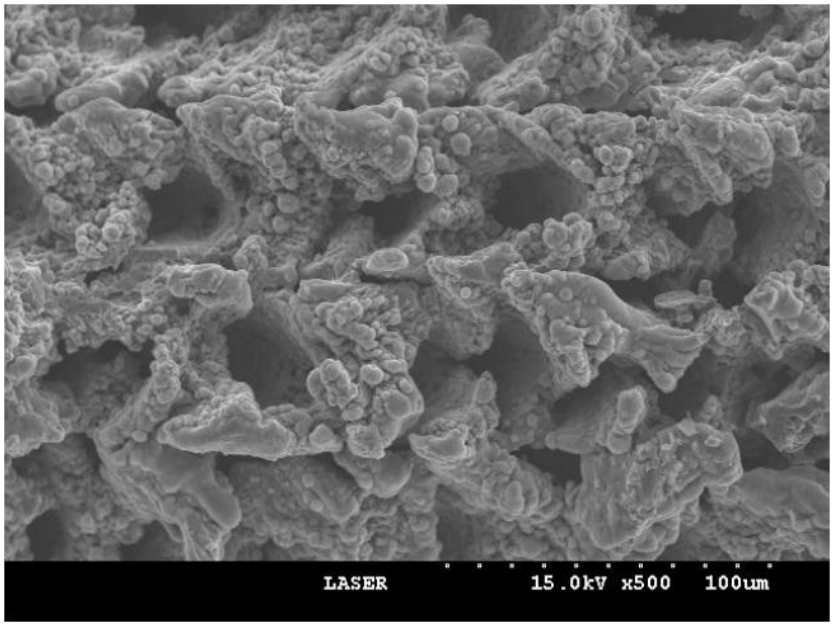

Figure 2.11 FE-SEM image of laser treated titanium implant [71]

In their study, Schröder et al. examined the use of an ultra-short pulsed Ti-Sapphire laser source to produce sub-micron spikes with nano features on the surface of Ti90/Al6/V4 implants. The implants were placed in rat tibia and tested for their antibacterial behaviour. Their results concluded that although the laser treatment did not reduce the bacterial load on the surface, it did however promote a higher eukaryotic cellular colonization as well as a better integration in the bone [72]. This research suggests that both micro and nano-scale topographies offer great potential as an implant surface modification technology.

Most research in this field is conducted on titanium and its alloys because of their present popularity in orthopaedics. At the time of writing of this thesis, no published in-vivo research was found on the performance of laser treated cobalt chromium alloy (CoCrMo) implants. However, CoCrMo implants are still widely used in several applications where high stiffness and wear-resistance are required. Some of the common uses of the material are total knee arthroplasty, dental prosthetics and scoliosis rods [73]. That being said, a few in-vitro studies have been published and the most recent of which will be highlighted below.

Qin et al. examined the effects of micro-patterning CoCrMo using a near infrared diode laser on its surface wettability and MC3T3-E1 osteoblast-like cells proliferation. No significant difference in the MC3T3-E1 cells proliferation was observed during the 48h incubation period between the different samples and control group [74].

In 2014 Matsugaki et al. reported that LIPSS on the surface of CoCrMo samples produced using a Ti:sapphire laser source had a strong effect on the alignment of primary osteoblast cells. In fact, osteoblasts aligned along the direction of the nanogrooves. Moreover, it was observed, unexpectedly, that the construction of bone matrix (extracellular matrix, ECM) occurred in a direction perpendicular to that of the cell direction. The significance of the findings stems from the fact that the orientation of the ECM plays a key role in determining the mechanical properties of bone, and therefore the success of any implant. The underlying reason behind this unexpected alignment is still not fully understood and under investigation [75].

Table 2.2 Summary of main literature on the application of LST in orthopaedics

Reference	Implant material	Laser treatment	Effect
[70]	Pure Ti	Micro pores	166% better anchorage in rabbits' tibia when compared to implants with machined surfaces (RTQ)
[71]	Pure Ti	Micro roughening	91% better anchorage in rabbits' femur when compared to HA coating (RTQ)
[76]	Ti-6Al-4V	Micro grooves	500% more force required to pull out implants when compared with polished surfaces in rabbit tibia
[77]	Pure Ti	Micro/nano roughening	61% better anchorage in rabbits' tibia when compare with machined surfaces (RTQ)
[78]	Pure Ti	Micro/nano roughening	143-195% better anchorage in both rabbits' tibia and femur compared to machined implants (RTQ)
[79]	Pure Ti	Micro pores	48% better anchorage in rabbits' tibia when compare to turned implants (RTQ)
[80]	Pure Ti	Micro/nano roughening	153% better anchorage in rabbits' tibia compared to machined implants (RTQ)

2.4 Laser processing of complex surfaces

Laser processing complex surfaces and intricate parts differs from conventional machining in mainly 2 ways. First, being an unconventional non-contact process, the laser beam's position relative to the working surface can vary, i.e. the distance from the focal plane to the surface (FOD) and the angle of incidence relative to the surface (BIA) can both vary within, application-defined, tolerable limits to achieve the required features. Processing beyond those limits results in a deviation from the desired

features, and in the case of surface functionalization, from the desired surface functional response [13]. Second, overlapping fields of view in laser processing can be problematic, unlike in conventional machining, the beam cannot carry on processing where it last ‘left off’. Therefore, overlapping patches in laser processing results in what is known as ‘stitching errors’ characterised by small grooves/channels at the image fields’ borders [81] (Figure 2.12).

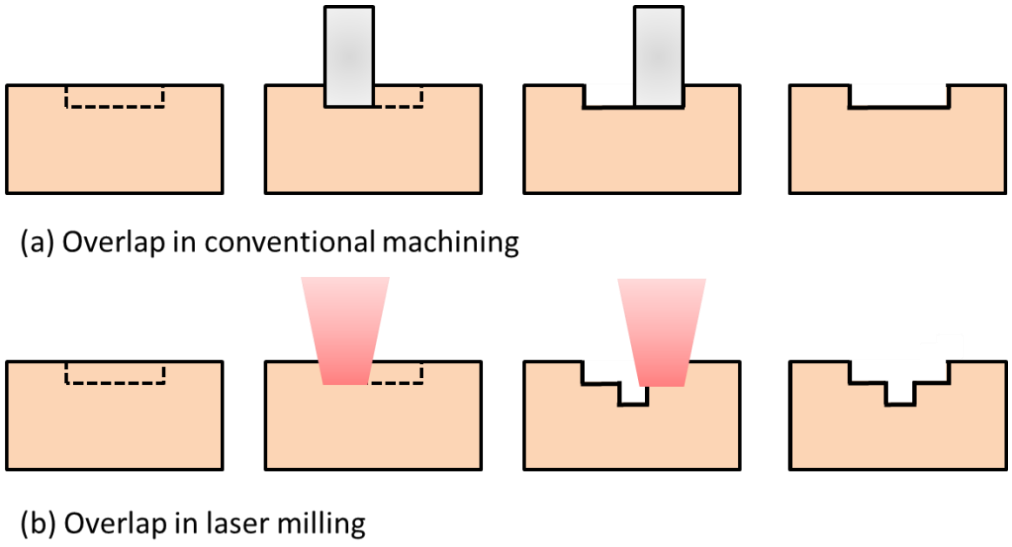

Figure 2.12 Effects of beam overlapping [81]

Partitioning parts into slices whose thicknesses are less than or equal to the depth of focus of the laser beam is a common approach to process complex surfaces. This is known as the layered method. In fact, Yung et al. employed this method to polish additively manufactured spherical components using a pulsed fibre laser, reducing the surface roughness by up to 93% [82]. Another approach for processing 3D parts is the use of common tessellation algorithm to partition the 3D part into planar scanhead fields. In their study Cuccolini et al. developed a method based on the STL file format of the part to mill features on 3D parts and join the different fields [81]. The STL method is also used for 3D structuring planar parts, such as chip breakers [83].

Figure 2.13 Example of a part processed using the CALM software developed by Cuccolini et al. based on the workpiece STL [81]

Additionally, a potential solution could be layering the scanning lens field of view onto the curved surface, a method suggested by Jiang et al [84]. Similarly, Diaci et al. proposed a rapid method to mark/engrave complex surfaces based on acquiring the surface data just before processing and adjusting the image to be engraved based on the acquired data by changing its height profiles, however without accounting for projection distortion [85]. Finally, Wang et al. suggested a more holistic approach, combining a lot of the previously mentioned concepts to pattern the surface of freeform parts. The LPAGS principle is characterised by projecting the texture within a square image field limited by the depth of focus and a critical angle [86].

Although efforts have been made towards finding a generic solution to a complex problem, still some compromises are made, for instance not factoring both the BIA and FOD when partitioning the surface, the large number of scanning fields or the constantly varying or non-optimized patch geometries.

A schematic summary of the main methods found in literature for laser processing freeform surfaces, is presented in figure 2.14.

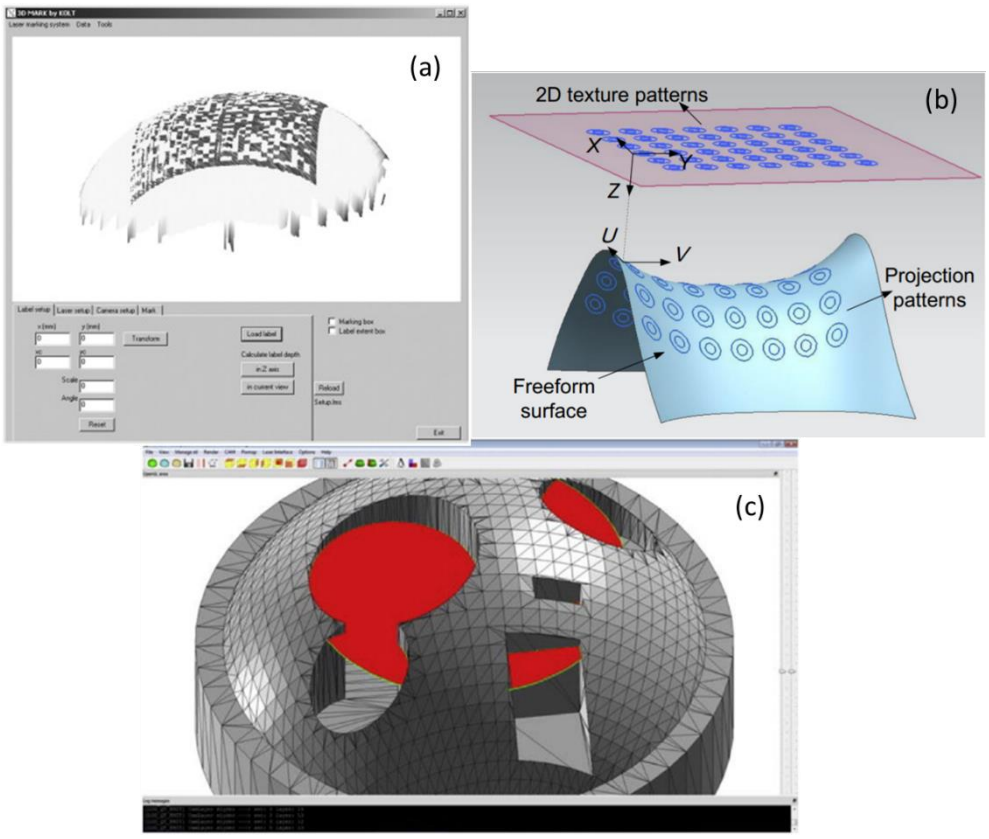

Figure 2.14 (a) Pattern projection after surface data acquisition presented in [85] (b) Field projection on known surface geometry presented in [86] (c) CL data derived from STL file presented in [81]

2.5 Summary of open research questions

The carried-out literature review highlighted the huge potential of laser technology in general, and using it as a surface modification process more specifically. In the context of biological applications/orthopaedics of laser surface modification, past literature indicates that the process may help induce bone cell proliferation, better implant anchorage and reduced bacterial adhesion, hence the significant interest from both

academics and industrialists. That being said, a number of research questions remain open, those are summarized below:

i. There is limited research on the suitability of the laser process on cobalt chrome alloys in terms of enhancing bone cell proliferation. Furthermore, the best laser strategies and feature scales are yet to be determined. And finally assessing the process performance against commercially used coatings is a must.

ii. Transferring the laser surface modification process from planar test specimens, often reported in literature, to actual 3D parts raises some concerns, namely, the effects of processing disturbances, present in 3D processing, on surface topography and thus added functionality. Those should be assessed and quantified.

iii. A better optimized method for processing 3D parts can still be developed which takes into account tolerable limits of the above-mentioned processing disturbances while optimizing the surface partitioning and joining.

References

1. Maiman, T.H., Stimulated Optical Radiation in Ruby. Nature, 1960. 187(4736): p. 493-494.
2. Bäuerle, D., Laser processing and chemistry. Fourth edition. ed. 2011, Heidelberg ; New York ;: Springer. xxii, 851 pages.
3. Fritschel, P. and L.S. Collaboration, LIGO: The Laser Interferometer Gravitational-Wave Observatory. Advanced Gravitational Wave Detectors, 2012: p. 113-132.
4. Demtröder, W., Laser spectroscopy: basic concepts and instrumentation. 2013: Springer Science & Business Media.
5. Wilson, J. and J.F.B. Hawkes, Lasers, principles and applications. Prentice Hall international series in optoelectronics. 1987, New York: Prentice Hall. xii, 308 p.
6. Bigot, S., J. Nestler, P. Dorrington, and S. Dimov, A Costing Methodology for Products Based on Emerging Micro and Nano Manufacturing Technologies. Micro and Nanosystems, 2011. 3(3): p. 254-262.
7. Dimov, S., E. Brousseau, R. Minev, and S. Bigot, Micro- and nano-manufacturing: Challenges and opportunities. Proceedings of the Institution of Mechanical Engineers, Part C: Journal of Mechanical Engineering Science, 2011. 226(1): p. 3-15.
8. Steen, W.M. and J. Mazumder, Laser Material Processing. 4th Edition. ed. 2010, London: Springer. xvii, 558 pages.
9. Cheng, J., C.-s. Liu, S. Shang, D. Liu, W. Perrie, G. Dearden, K.J.O. Watkins, and L. Technology, A review of ultrafast laser materials micromachining. 2013. 46: p. 88-102.

10. Dahotre, N.B. and S.P. Harimkar, Laser fabrication and machining of materials. 2008, New York, N.Y.: Springer. xv, 558 p.
11. Jwad, T., S.A. Deng, H. Butt, and S. DimovSchool, Laser induced single spot oxidation of titanium. Applied Surface Science, 2016. 387: p. 617-624.
12. Petkov, P.V., S.S. Dimov, R.M. Minev, and D.T. Pham, Laser milling: pulse duration effects on surface integrity. Proceedings of the Institution of Mechanical Engineers Part B-Journal of Engineering Manufacture, 2008. 222(1): p. 35-45.
13. Batal, A., A. Michalek, A. Garcia-Giron, V. Nasrollahi, P. Penchev, R. Sammons, and S. Dimov, Effects of laser processing conditions on wettability and proliferation of Saos-2 cells on CoCrMo alloy surfaces, in Advanced Optical Technologies. 2019.
14. Amer, M.S., M.A. El-Ashry, L.R. Dosser, K.E. Hix, J.F. Maguire, and B. Irwin, Femtosecond versus nanosecond laser machining: comparison of induced stresses and structural changes in silicon wafers. Applied Surface Science, 2005. 242(1): p. 162-167.
15. Mathew, M.M., R.N. Bathe, G. Padmanabham, R. Padmanaban, and S. Thirumalini, A study on the micromachining of molybdenum using nanosecond and femtosecond lasers. The International Journal of Advanced Manufacturing Technology, 2019. 104(9): p. 3239-3249.
16. Shibata, A., M. Machida, N. Kondo, and M.J.A.P.A. Terakawa, Biodegradability of poly (lactic-co-glycolic acid) and poly (l-lactic acid) after deep-ultraviolet femtosecond and nanosecond laser irradiation. 2017. 123(6): p. 438.

17. Donnet, C., J. Granier, G. Verge, Y. Bleu, S. Reynaud, and F. Vocanson, 2D reproduction of the face on the Turin Shroud by infrared femtosecond pulse laser processing. Applied Optics, 2019. 58(9): p. 2158-2165.
18. Garban-Labaune, C., E. Fabre, C. Max, R. Fabbro, F. Amiranoff, J. Virmont, M. Weinfeld, and A.J.P.R.L. Michard, Effect of laser wavelength and pulse duration on laser-light absorption and back reflection. 1982. 48(15): p. 1018.
19. Piegari, A. and F. Flory, Optical thin films and coatings: From materials to applications. 2018: Woodhead Publishing.
20. Guo, M., G. Jin, J. Cai, W. Zhang, and Z. Wei. Study and design of beam expander with wide aperture. in International Symposium on Optoelectronic Technology and Application 2014: Laser Materials Processing; and Micro/Nano Technologies. 2014. International Society for Optics and Photonics.
21. Venkatakrishnan, K., B. Tan, P. Stanley, and N.R. Sivakumar, The effect of polarization on ultrashort pulsed laser ablation of thin metal films. Journal of Applied Physics, 2002. 92(3): p. 1604-1607.
22. Sanner, N., N. Huot, E. Audouard, C. Larat, and J.P. Huignard, Direct ultrafast laser micro-structuring of materials using programmable beam shaping. Optics and Lasers in Engineering, 2007. 45(6): p. 737-741.
23. Penchev, P., S. Dimov, and D. Bhaduri, Experimental investigation of 3D scanheads for laser micro-processing. Optics and Laser Technology, 2016. 81: p. 55-59.
24. Batal, A., A. Michalek, P. Penchev, A. Kupisiewicz, S.J.I.J.o.M.T. Dimov, and Manufacture, Laser processing of freeform surfaces: A new approach based on an efficient workpiece partitioning strategy. 2020. 156: p. 103593.

25. Gu, B. The status of industrial lasers in China. 2019; Available from: https://www.industrial-lasers.com/home/article/14068621/the-status-of-industrial-lasers-in-china.

26. Wu, P.H., C.W. Cheng, C.P. Chang, T.M. Wu, and J.K. Wang, Fabrication of large-area hydrophobic surfaces with femtosecond-laser-structured molds. Journal of Micromechanics and Microengineering, 2011. 21(11).

27. Bekesi, J., J.J.J. Kaakkunen, W. Michaeli, F. Klaiber, M. Schoengart, J. Ihlemann, and P. Simon, Fast fabrication of super-hydrophobic surfaces on polypropylene by replication of short-pulse laser structured molds. Applied Physics a-Materials Science & Processing, 2010. 99(4): p. 691-695.

28. Romano, J.M., M. Gulcur, A. Garcia-Giron, E. Martinez-Solanas, B.R. Whiteside, and S.S. Dimov, Mechanical durability of hydrophobic surfaces fabricated by injection moulding of laser-induced textures. Applied Surface Science, 2019. 476: p. 850-860.

29. Nimb, L., K. Gotfredsen, and J. Steen Jensen, Mechanical failure of hydroxyapatite-coated titanium and cobalt-chromium-molybdenum alloy implants. An animal study. Acta Orthop Belg, 1993. 59(4): p. 333-8.

30. Hutchings, I. and P. Shipway, Tribology: friction and wear of engineering materials. 2017: Butterworth-Heinemann.

31. Holmberg, K. and A. Erdemir, Influence of tribology on global energy consumption, costs and emissions. Friction, 2017. 5(3): p. 263-284.

32. Ezhilmaran, V., L. Vijayaraghavan, and N.J. Vasa, Investigation of Nd3+:YAG Laser Aided Surface Texturing to Improve Tribological Characteristics of Piston Ring. Journal of Laser Micro Nanoengineering, 2017. 12(3): p. 195-202.

33. Vladescu, S.C., A.V. Olver, I.G. Pegg, and T. Reddyhoff, Combined friction and wear reduction in a reciprocating contact through laser surface texturing. Wear, 2016. 358-359: p. 51-61.
34. Lerner, E.J., Laser marking systems strive for color and speed. Laser Focus World, 1999. 35(10): p. 123-+.
35. Jwad, T., S. Deng, H. Butt, and S. Dimov, Fabrication of TiO2 Thin Film-Based Fresnel Zone Plates by Nanosecond Laser Direct Writing. Journal of Micro and Nano-Manufacturing, 2018. 6(1).
36. Hermens, U., M. Pothen, K. Winands, K. Arntz, and F. Klocke, Automated polarization control for the precise alignment of laser-induced self-organized nanostructures. Optics and Lasers in Engineering, 2018. 101: p. 44-50.
37. Young, T., III. An essay on the cohesion of fluids. Philosophical Transactions of the Royal Society of London, 1805. 95: p. 65-87.
38. Marmur, A., Wetting on Hydrophobic Rough Surfaces: To Be Heterogeneous or Not To Be? Langmuir, 2003. 19(20): p. 8343-8348.
39. Cassie, A.B.D. and S. Baxter, Wettability of porous surfaces. Transactions of the Faraday Society, 1944. 40(0): p. 546-551.
40. Blossey, R., Self-cleaning surfaces - virtual realities. Nature Materials, 2003. 2(5): p. 301-306.
41. Farhadi, S., M. Farzaneh, and S.A. Kulinich, Anti-icing performance of superhydrophobic surfaces. Applied Surface Science, 2011. 257(14): p. 6264-6269.
42. Ranella, A., M. Barberoglou, S. Bakogianni, C. Fotakis, and E. Stratakis, Tuning cell adhesion by controlling the roughness and wettability of 3D micro/nano silicon structures. Acta Biomater, 2010. 6(7): p. 2711-20.

43. Tamada, Y. and Y. Ikada, Cell adhesion to plasma-treated polymer surfaces. Polymer, 1993. 34(10): p. 2208-2212.

44. Dowling, D.P., I.S. Miller, M. Ardhaoui, and W.M. Gallagher, Effect of surface wettability and topography on the adhesion of osteosarcoma cells on plasma-modified polystyrene. J Biomater Appl, 2011. 26(3): p. 327-47.

45. Jin, M.H., X.J. Feng, J.M. Xi, J. Zhai, K.W. Cho, L. Feng, and L. Jiang, Super-hydrophobic PDMS surface with ultra-low adhesive force. Macromolecular Rapid Communications, 2005. 26(22): p. 1805-1809.

46. Trdan, U., M. Hocevar, and P. Gregorcic, Transition from superhydrophilic to superhydrophobic state of laser textured stainless steel surface and its effect on corrosion resistance. Corrosion Science, 2017. 123: p. 21-26.

47. Albrektsson, T. and C. Johansson, Osteoinduction, osteoconduction and osseointegration. European Spine Journal, 2001. 10: p. S96-S101.

48. Kawano, T., W. Prananingrum, Y. Ishida, T. Goto, Y. Naito, M. Watanabe, Y. Tomotake, and T. Ichikawa, Blue-Violet Laser Modification of Titania Treated Titanium: Antibacterial and Osteo-Inductive Effects. Plos One, 2013. 8(12).

49. Balla, V.K., S. Dey, A.A. Muthuchamy, G.D.J. Ram, M. Das, and A. Bandyopadhyay, Laser surface modification of 316L stainless steel. Journal of Biomedical Materials Research Part B-Applied Biomaterials, 2018. 106(2): p. 569-577.

50. Schneider, J., V. Djamiykov, and C.J.B.j.o.n. Greiner, Friction reduction through biologically inspired scale-like laser surface textures. 2018. 9(1): p. 2561-2572.

51. Yang, Z., X. Liu, Y.J.J.o.c. Tian, and i. science, Insights into the wettability transition of nanosecond laser ablated surface under ambient air exposure. 2019. 533: p. 268-277.
52. Yang, Z., X. Liu, Y.J.C. Tian, S.A. Physicochemical, and E. Aspects, Novel metal-organic super-hydrophobic surface fabricated by nanosecond laser irradiation in solution. 2020. 587: p. 124343.
53. Zhao, J., J. Guo, P. Shrotriya, Y. Wang, Y. Han, Y. Dong, S.J.O. Yang, and L. Technology, A rapid one-step nanosecond laser process for fabrication of super-hydrophilic aluminum surface. 2019. 117: p. 134-141.
54. Tsai, H.-Y., Y.-C. Hsieh, Y.-H. Lin, H.-C. Chang, Y.-H. Tang, and K.-C.J.M. Huang, Fabrication of Hydrophilic Surface on Rigid Gas Permeable Contact Lenses to Enhance the Wettability Using Ultraviolet Laser System. 2019. 10(6): p. 394.
55. Yang, L., X. Luo, W. Chang, Y. Tian, Z. Wang, J. Gao, Y. Cai, Y. Qin, and M.J.J.o.M.P. Duxbury, Manufacturing of anti-fogging super-hydrophilic microstructures on glass by nanosecond laser. 2020. 59: p. 557-565.
56. Babuska, V., J. Palan, J. Kolaja Dobra, V. Kulda, M. Duchek, J. Cerny, and D.J.M. Hrusak, Proliferation of osteoblasts on laser-modified nanostructured titanium surfaces. 2018. 11(10): p. 1827.
57. Yu, Z., S. Yin, W. Zhang, X. Jiang, and J.J.J.o.B.M.R.P.B.A.B. Hu, Picosecond laser texturing on titanium alloy for biomedical implants in cell proliferation and vascularization. 2020. 108(4): p. 1494-1504.
58. Gnilitskyi, I., M. Pogorielov, R. Viter, A.M. Ferraria, A.P. Carapeto, O. Oleshko, L. Orazi, O.J.N.N. Mishchenko, Biology, and Medicine, Cell and

tissue response to nanotextured Ti6Al4V and Zr implants using high-speed femtosecond laser-induced periodic surface structures. 2019. 21: p. 102036.

59. Pan, Q., Y. Cao, W. Xue, D. Zhu, and W.J.L. Liu, Picosecond laser-textured stainless steel superhydrophobic surface with an antibacterial adhesion property. 2019. 35(35): p. 11414-11421.

60. Chan, C.-W., L. Carson, G.C. Smith, A. Morelli, and S.J.A.S.S. Lee, Enhancing the antibacterial performance of orthopaedic implant materials by fibre laser surface engineering. 2017. 404: p. 67-81.

61. Jalil, S.A., M. Akram, J.A. Bhat, J.J. Hayes, S.C. Singh, M. ElKabbash, and C.J.A.S.S. Guo, Creating superhydrophobic and antibacterial surfaces on gold by femtosecond laser pulses. 2020. 506: p. 144952.

62. Lu, L.B., Z. Zhang, Y.C. Guan, and H.Y. Zheng, Comparison of the effect of typical patterns on friction and wear properties of chromium alloy prepared by laser surface texturing. Optics and Laser Technology, 2018. 106: p. 272-279.

63. Garcia-Giron, A., J.M. Romano, Y. Liang, B. Dashtbozorg, H. Dong, P. Penchev, and S.S. Dimov, Combined surface hardening and laser patterning approach for functionalising stainless steel surfaces. Applied Surface Science, 2018. 439: p. 516-524.

64. Bonse, J., J. Kruger, S. Hohm, and A. Rosenfeld, Femtosecond laser-induced periodic surface structures. Journal of Laser Applications, 2012. 24(4).

65. Graf', S. and F.A. Muller, Polarisation-dependent generation of fs-laser induced periodic surface structures. Applied Surface Science, 2015. 331: p. 150-155.

66. Epperlein, N., F. Menzel, K. Schwibbert, R. Koter, J. Bonse, J. Sameith, J. Kruger, and J. Toepel, Influence of femtosecond laser produced

nanostructures on biofilm growth on steel. Applied Surface Science, 2017. 418: p. 420-424.

67. Pazokian, H., S. Jelvani, M. Mollabashi, J. Barzin, and G.A. Farahani, ArF laser surface modification of polyethersulfone film: Effect of laser fluence in improving surface biocompatibility. Applied Surface Science, 2011. 257(14): p. 6186-6190.

68. Hill, M.R., A.T. DeWald, A.G. Demma, L.A. Hackel, H.L. Chen, C.B. Dane, R.C. Specht, and F.B. Harris, Laser peening technology. Advanced Materials & Processes, 2003. 161(8): p. 65-67.

69. Kalentics, N., E. Boillat, P. Peyre, S. Ciric-Kostic, N. Bogojevic, and R.E. Loge, Tailoring residual stress profile of Selective Laser Melted parts by Laser Shock Peening. Additive Manufacturing, 2017. 16: p. 90-97.

70. Cho, S.A. and S.K. Jung, A removal torque of the laser-treated titanium implants in rabbit tibia. Biomaterials, 2003. 24(26): p. 4859-4863.

71. Park, E.Y., H.O. Sohn, and E.K. Kim, Comparison of the removal torque and a histomorphometric evaluation of the RBM treated implants with the RBM followed by laser treated implants: an experimental study in rabbits. Yeungnam Univ J Med, 2019. 36(1): p. 43-49.

72. Schröder, M.L., N. Angrisani, E. Fadeeva, J. Hegermann, and J. Reifenrath, Laser-structured spike surface shows great bone integrative properties despite infection in vivo. Materials Science and Engineering: C, 2020. 109: p. 110573.

73. Batal, A., R. Sammons, and S. Dimov, Response of Saos-2 osteoblast-like cells to laser surface texturing, sandblasting and hydroxyapatite coating on

CoCrMo alloy surfaces. Materials Science and Engineering: C, 2019. 98: p. 1005-1013.

74. Qin, L.G., Q.F. Zeng, W.X. Wang, Y.L. Zhang, and G.N. Dong, Response of MC3T3-E1 osteoblast cells to the microenvironment produced on Co-Cr-Mo alloy using laser surface texturing. Journal of Materials Science, 2014. 49(6): p. 2662-2671.

75. Matsugaki, A., G. Aramoto, T. Ninomiya, H. Sawada, S. Hata, and T. Nakano, Abnormal arrangement of a collagen/apatite extracellular matrix orthogonal to osteoblast alignment is constructed by a nanoscale periodic surface structure. Biomaterials, 2015. 37: p. 134-143.

76. Chen, J., R. Bly, M. Saad, M. AlKhodary, R. El-Backly, D.J. Cohen, N. Kattamis, M. Fatta, W. Moore, C.B.J.M.S. Arnold, and E. C, In-vivo study of adhesion and bone growth around implanted laser groove/RGD-functionalized Ti-6Al-4V pins in rabbit femurs. 2011. 31(5): p. 826-832.

77. Faeda, R.S., H.S. Tavares, R. Sartori, A.C. Guastaldi, E.J.J.o.O. Marcantonio Jr, and M. Surgery, Biological performance of chemical hydroxyapatite coating associated with implant surface modification by laser beam: biomechanical study in rabbit tibias. 2009. 67(8): p. 1706-1715.

78. Palmquist, A., L. Emanuelsson, R. Brånemark, and P.J.J.o.B.M.R.P.B.A.B. Thomsen, Biomechanical, histological and ultrastructural analyses of laser micro-and nano-structured titanium implant after 6 months in rabbit. 2011. 97(2): p. 289-298.

79. Hallgren, C., H. Reimers, D. Chakarov, J. Gold, and A.J.B. Wennerberg, An in vivo study of bone response to implants topographically modified by laser micromachining. 2003. 24(5): p. 701-710.

80. Shah, F.A., M.L. Johansson, O. Omar, H. Simonsson, A. Palmquist, and P.J.P.o. Thomsen, Laser-modified surface enhances osseointegration and biomechanical anchorage of commercially pure titanium implants for bone-anchored hearing systems. 2016. 11(6): p. e0157504.

81. Cuccolini, G., L. Orazi, and A. Fortunato, 5 Axes computer aided laser milling. Optics and Lasers in Engineering, 2013. 51(6): p. 749-760.

82. Yung, K.C., T.Y. Xiao, H.S. Choy, W.J. Wang, and Z.X. Cai, Laser polishing of additive manufactured CoCr alloy components with complex surface geometry. Journal of Materials Processing Technology, 2018. 262: p. 53-64.

83. Pacella, M.J.T.I.J.o.A.M.T., A new low-feed chip breaking tool and its effect on chip morphology. 2019. 104(1-4): p. 1145-1157.

84. Jiang, M., X.Z. Wang, S.H. Ke, F. Zhang, and X.Y. Zeng, Large scale layering laser surface texturing system based on high speed optical scanners and gantry machine tool. Robotics and Computer-Integrated Manufacturing, 2017. 48: p. 113-120.

85. Diaci, J., D. Bracun, A. Gorkic, and J. Mozina, Rapid and flexible laser marking and engraving of tilted and curved surfaces. Optics and Lasers in Engineering, 2011. 49(2): p. 195-199.

86. Wang, X.Z., J. Duan, M. Jiang, S.H. Ke, B.Y. Wu, and X.Y. Zeng, Study of laser precision ablating texture patterns on large-scale freeform surface. International Journal of Advanced Manufacturing Technology, 2017. 92(9-12): p. 4571-4581.

CHAPTER 3: RESPONSE OF SAOS-2 OSTEOBLAST-LIKE CELLS TO LASER SURFACE TEXTURING, SANDBLASTING AND HYDROXYAPATITE COATING ON COCRMO ALLOY SURFACES

A. Batal[1], R. Sammons[2], S. Dimov[1]

[1] Department of Mechanical Engineering, University of Birmingham, Edgbaston, Birmingham, B15 2TT, UK

[2] School of Dentistry, University of Birmingham, Edgbaston, Birmingham, B5 7EG, UK

This research was published as a full-length article in *Materials Science and Engineering: C* (2019):

Batal, A., Sammons, R., & Dimov, S. (2019). Response of Saos-2 osteoblast-like cells to laser surface texturing, sandblasting and hydroxyapatite coating on CoCrMo alloy surfaces. Materials Science and Engineering: C, 98, 1005-1013.

Authors' Contributions:

A. Batal

Main author, conducted the laser experiments and functional tests.

R. Sammons

Supervision and proofreading

S. Dimov

Supervision and proofreading

Abstract

Cobalt chrome alloys are commonly used in orthopaedic implants where high stiffness and wear resistance are required. This study proposes Laser Surface Texturing (LST) as a cost-effective mean for producing bioinspired surface textures in order to improve the performance of CoCrMo orthopaedic implants. Cobalt-chrome alloy disks were modified using three different LST strategies: i) micro-scale texturing using a nanosecond laser source; (ii) micro-scale texturing with an ultrashort laser source and (iii) bioinspired sub-micron scale texturing with an ultrashort laser source. The modified disks were characterized and compared to blasted, hydroxyapatite coated and polished surface finishes. Saos-2 osteoblast-like cells were seeded on the different surfaces and their proliferation and morphology was assessed. The laser modification increases the surface energy of the CoCrMo alloy disks when compared to their untreated counterparts. The bioinspired sub-micron textured surfaces exhibited the highest cell metabolic activity on day 7 of the MTT assay.

3.1 Introduction

Cobalt-chrome alloys are widely used by the medical device industry especially as orthopaedic implant materials. They were first introduced in the 1930s owing to their remarkable corrosion resistance, biocompatibility and excellent mechanical properties [1]. Due to their high stiffness and superior wear-resistance, cobalt-chrome alloys are used instead of titanium alloys in high stress applications such as scoliosis rods and bearing surfaces [2,3]. Moreover, the most popular total knee arthroplasty (TKA) design, accounting for 36% of all the TKAs performed in 2009 in England and Wales in 2009, was redesigned in 2006 changing the implant material from titanium to cobalt-chrome based alloy [4,5]. The objective of this change was to minimize the polyethylene insert wear (backside wear), and to increase implant success and life expectancy [5]. Early clinical results showed survival rates of 96.6% with revision for any reason and 98.6% with revision for aseptic failure at 5 years postoperative [6]. These results were very encouraging when compared to the previous titanium design which recorded a 97.2% success rate for any revision at five years and a 99.5% rate for aseptic failure. Now, cobalt-chrome alloys are also commonly used in dental prosthetics, due to their fatigue resistance and retaining capabilities and they are the material of choice for many removable partial dentures [7,8]. However the alloy's remarkable hardness makes it difficult to machine using conventional processes [9].

Although cobalt chrome alloys outperform titanium in stiffness and wear resistance, concerns have been raised about cobalt toxicity. In particular, adverse effects caused by wear debris were reported in patients with CoCrMo metal-on-metal bearing systems [10]. Therefore, this is a very active research field and there are continuous developments to improve CoCr alloys' biocompatibility. For example, De Villiers et al. developed silver chromium nitride coatings for cobalt-chrome bearing surfaces and

their use led to less wear while negligible cobalt was released when compared to their uncoated counterparts [11].

Hydroxyapatite (HA) coatings are widely used in industry to improve uncemented stem survival [12,13]. Although coatings may help to improve the performance of CoCrMo orthopaedic implants, there are several limitations associated with their broad use, i.e. high manufacturing costs, potential failures at the interfaces and detrimental interactions with physiological fluids [14]. Also, it is worth mentioning that the benefits of these coatings are still questionable [15].

In recent years, bio-inspired hierarchical micro/sub-micron topographies have shown potential to improve bioactivity and biocompatibility of implant materials. Sousa et al. demonstrated that bio-inspired freestanding multilayer membranes produced via a layer-by-layer technique, enhanced the adhesive properties of natural-based polymers [16]. Wang et al. showed that self-assembled TiO_2 nanotubes on a hierarchical micro/nano titanium surface lead to superior attachment and growth of osteoblasts when compared with a smooth machined Ti surface [17]. Li et al. produced microwell arrays inspired by the surface of rose petals to enhance the contact between polyester and fibroblasts [18]. Such intricate structures are commonly fabricated via complex, difficult to control and expensive chemical processes which limit their commercial viability (such as chemical etching or lithography). Furthermore, most studies were conducted on polymers and titanium.

Laser surface texturing (LST) has attracted the interest of researchers and industry in the last fifteen years, mostly due its tribological applications. Many studies reported

the benefits of LST in friction and wear reduction that led to commercial applications of the technology for cylinder liner honing and mechanical seals [19]. The non-contact nature of laser processing makes it an attractive tool to process and modify the otherwise hard to machine cobalt-chrome alloys.

More recently, LST has attracted significant interest as a surface modification technology with potential applications in orthopaedic implants. LST-based surface modifications were reported to reduce the risk of aseptic failures of implants and also to strengthen the bond between the bone and implant by promoting bone cell proliferation and attachment [20, 21, 22, 23]. Mariscal-Muñoz et al. cultured primary osteoblast cells on laser-modified (roughening) Ti surfaces and demonstrated increased ALPase activity and mineralised nodule formation together with enhanced expression of mature bone cell phenotypical markers in comparison with polished Ti surfaces [24]. Furthermore, Shah et al. demonstrated that the Nd:YAG laser modifications (roughening) of commercially pure titanium implants increased the removal torque (RTQ) in rabbit tibiae by 153% when compared to machined implants. The higher RTQ was attributed to the strength of the bone-implant interface; laser-treated implants showed fracture lines at 30 to 50 µm from the interface when tested for failure, whereas separation occurred at the bone-implant interface for the machined surfaces [25].

Many researchers stated that implant surface energy plays a significant role in the interactions of the implant with biological fluids, cells and tissues. In particular, hydrophilic surfaces were reported to promote osseointegration and implant anchorage [26, 27, 28, 29, 30, 31]. However, such surface functionalities are

commonly achieved by means of toxic gases [32], harmful chemicals or expensive coating procedures [33, 34, 35]. At the same time the use of LST as an alternative solution for producing hydrophilic implant surfaces, which may favour biological interactions, has not been thoroughly examined; in fact, most of the studies reported an opposite (hydrophobic) effect unless the samples had been stored in controlled environments [36, 37, 38, 39, 40, 41].

There is currently limited literature on the use of LST on CoCr alloys to improve surface properties for cell interactions. Qin et al. investigated the effects of LST on CoCrMo alloy wettability and MC3T3-E1 osteoblast-like cells proliferation. However the disjoint micro-scale patterns (circular, rectangular and triangular pits) produced lead to an increase in the water contact angle when compared with untreated surfaces. Moreover, while the duration of the cell incubation was only 48h, no significant difference in the MC3T3-E1 cells proliferation was observed between the different samples [42]. Further work is hence required to study the effects of bio-inspired surface topographies, achievable via LST, on cell attachment and proliferation on cobalt-chrome alloys. This research evaluates the wettability and proliferation of Saos-2 osteoblast-like cells on 3 different types of laser modified CoCrMo alloy surfaces: nanosecond laser structuring, femtosecond laser structuring and sub-micron laser patterning. It also compares their performance with the current state of the art in the implant industry, i.e. blasted and HA coated surfaces, together with polished surfaces as references.

3.2 Material and Methods

3.2.1 CoCrMo Samples

A surgical cobalt-chromium-molybdenum casting alloy with the following Wt% composition was used in all experiments: 67.0% Co, 27.0% Cr and 5.0% Mo. Disks with a diameter of 18mm and 2mm thickness were supplied by MatOrtho Ltd. UK. The samples were sandblasted with 20 grit white fused alumina, and some were manually polished on linishing belts down to a mirror finish (Ra < 0.05 µm).

3.2.2 Laser Surface Texturing

Three different LST approaches were investigated as follows: (i) micro-scale texturing employing a nanosecond laser source (NS surfaces) ; (ii) micro-scale texturing with an ultrashort laser source (FS surfaces) and (iii) bioinspired sub-micron scale texturing with an ultrashort laser source (NT surfaces), namely to mimic the corneal surface of some insects such as moths, butterflies and drosophila, as such structures have been shown to possess good biological surface properties [43] . The ultrashort laser had the following technical specification (Satsuma from Amplitude Systemes): 5W average power, 10µJ max pulse energy, 310fs pulse duration, up to 500 KHz repetition rate, 1030 nm wavelength and a beam quality M^2 better than 1.2. The technical specification of the nanosecond laser source (redENERGY G4 from SPI Lasers) was as follows: 50W average power, 0.71 mJ max pulse energy, pulse durations in the range 15 to 220 ns, up to 1Mhz repetition rate, 1060 nm wavelength and beam quality

M^2 better than 1.3. The laser spot size was approximately 30 µm in diameter at the focal point for both laser sources.

A grid of 100 x 100 µm grooves with a spacing of 400 µm was chosen as the micro-scale pattern for both NS and FS surfaces. This particular groove size was selected to be similar to the size of Saos-2 cells that is generally just under 100 µm in any direction when adhered and fully spread on a flat surface [44]. The microscale recessions on the surface should offer a favourable environment for the cells to settle, adhere and spread [45]. To better understand the influence of pulse duration on resulting surface topographies, and consequently cell growth, the grids were produced using two different laser sources.

Laser Induced Periodic Surface Structures (LIPSS) have been shown to induce a positive response from osteoblast cells (and osteoblast-like cell lines) on various polymers and titanium alloys. However, the sub-micron ripples tend to influence the orientation and spreading of cells [46]. Thus, this bio-inspired semi-omnidirectional geometry was chosen to produce the NT surfaces in an effort to avoid any directionality.

The NS and FS surfaces were produced on the blasted disks (B). To produce NT surfaces, LST was carried out on mirror finish polished disks (P). The three LST strategies employed to produce NS, FS and NT surfaces are depicted in Figure 3.1 while the laser parameters used in the experiments are given in Table 3.1. These parameters were chosen in order to achieve the desired topographies within minimal

processing times, they were derived through trial and error. LST was performed in ambient conditions with the assistance of a fume extractor.

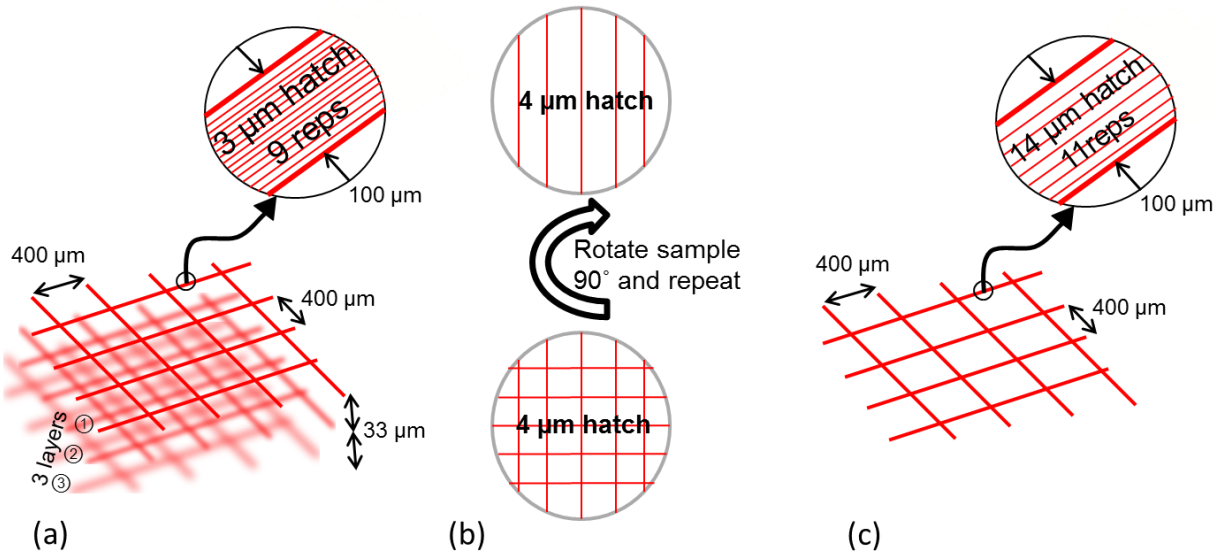

Figure 3.1 Schematic diagrams of the LST strategies used to produce (a) FS surfaces, (b) NT surfaces and (c) NS surfaces

Note: *hatch* refers to the step-over distance between two consecutive laser scans while *reps* to the number of scanning repetitions per layer.

Table 3.1 Laser parameters used for LST

Sample	Average Power (W)	Energy Density (J/cm^2)	Pulse Duration	Repetition Rate (kHz)	Scanning Speed (mm/s)
FS	4.19	1.19	310 fs	500	1000
NT	1^{st} scan: 0.57/2^{nd} scan: 0.1	0.16/0.028	310 fs	250	1000
NS	33.4	28.3	220 ns	65.5	950

3.2.3 Hydroxylapatite Coating

High-purity synthetic calcium hydroxylapatite from Plasma Biotal Ltd. UK was used to coat the blasted disks. Particles 30 μm in diameter with a highly crystalline structure (>50%) were deposited on the CoCrMo surface. The coating meets the requirements of ISO 13779:2000 which specifies hydroxyapatite powders that should be used as a raw material for producing surgical implants or their coatings.

3.2.4 Surface Topography Assessment

Focus variation microscopy, i.e. G5 InfiniteFocus system from Alicona, was used to analyse the 3D surface topographies of the B, NS, FS and HA disks, to assess their surface roughness. The surface roughness of the P and NT samples was also measured but their respective 3D representations omitted as they lacked visible topographical features.

All 6 samples were examined by scanning electron microscopy using a Zeiss EVO MA 10 microscope: WD=6.0mm and EHT=20.00kV.

Table 3.2 Summary of the tested samples

Sample	Treatment	Original Surface
B	Sand Blasting	Cast
P	Mirror Finish Polishing	Cast
NT	Sub-Micron Texturing Femtosecond Laser	Mirror Finish Polished
FS	Micro Grooves Femtosecond Laser	Blasted
NS	Micro Grooves Nanosecond Laser	Blasted
HA	Hydroxylapatite Coated	Blasted

3.2.5 Surface Wettability

Contact angle (CA) analysis was performed employing the sessile drop technique, using an Attension Theta optical tensiometer with 4μL drops of Milli-Q water. The

measurements were taken 5 and 30 days after LST to assess the impact of disk storage in ambient conditions on the evolution of contact angle and thus to judge the functional stability of created topographies. Before the first measurement the samples underwent rigorous cleaning: The samples were subjected to three 15 min ultrasonic baths, first, in 8 wt% aqueous oxalic acid, second, in pure acetone, and third, in 70 vol% ethanol aqueous solution. The samples were rinsed with distilled pure water in-between baths and finally dried with argon gas.

3.2.6 Cell Culture

All CoCrMo disks underwent the cleaning protocol described above followed by autoclaving at 120° C 1 bar pressure . Specimens were then placed in 12-well plates (Thermo Scientific™ Nunc™ Cell-Culture Treated Multidishes) and approximately $2x10^4$ Saos-2 osteoblast-like cells were seeded on each sample in McCoy's 5A medium supplemented with 10% FBS, I00U/mL of Penicillin and 100µg/mL of Streptomycin. The well plates were placed in a humidified incubator at 37˚C in an atmosphere of 5% CO_2 and the culture medium was changed every 2 days.

3.2.7 Cell Proliferation

Saos-2 cells metabolic activity was evaluated via a MTT assay [47], reflecting the cells' proliferation on the different CoCrMo specimens. MTT was prepared in phosphate buffered saline (PBS, pH 7.4) at a concentration of 5mg/mL. 100µL of the MTT solution was added to each well and the plates were incubated at 37˚C in an atmosphere of 5% CO_2 for 4 hours at the selected time intervals (2, 4 and 7 days). The medium was then removed and 1mL of DMSO was added to each well to dissolve the formazan. The well plates were placed on a shaking platform for 5 minutes and then the optical density was measured at 570 nm using a spectrophotometer, the Biotek ELx800.

3.2.8 Cell Morphology

At selected time intervals: 2, 4 and 7 days after seeding, samples were rinsed with phosphate buffered saline (PBS, pH 7.4) and then immersed in 2.5% EM grade glutaraldehyde in 0.1M sodium cacodylate buffer (pH 7.3) prepared on the day. After fixation, the different CoCrMo disks were then dehydrated by immersion in solutions of increased ethanol concentration: 20, 30, 40, 50, 60, 70, 90, 95 (twice) and 100% (twice). The ethanol was then removed and the disks' surfaces were rinsed with hexamethyldisilzane (HMDS) and left to evaporate in a fume cupboard overnight. Finally the disks were sputter coated with gold and examined under SEM to image the attached cells on the surface.

3.2.9 Statistical Analysis

All data was expressed as means with their standard deviations. Contact angle average values were calculated based on 5 measurements for each disk type (5 disks for every type of surface) while the average MTT optical density values based on 3 measurements (3 disks for every type of surface). Statistical analysis was performed using Minitab 17 Statistical Software. General Linear Model ANOVA was used to examine differences between the groups. Values of $p<0.05$ were considered significant.

3.3 Results and Discussion

3.3.1 Focus Variation Microscopy

The surface topographies of the B, FS, NS and HA specimens are depicted in Figure 3.2.

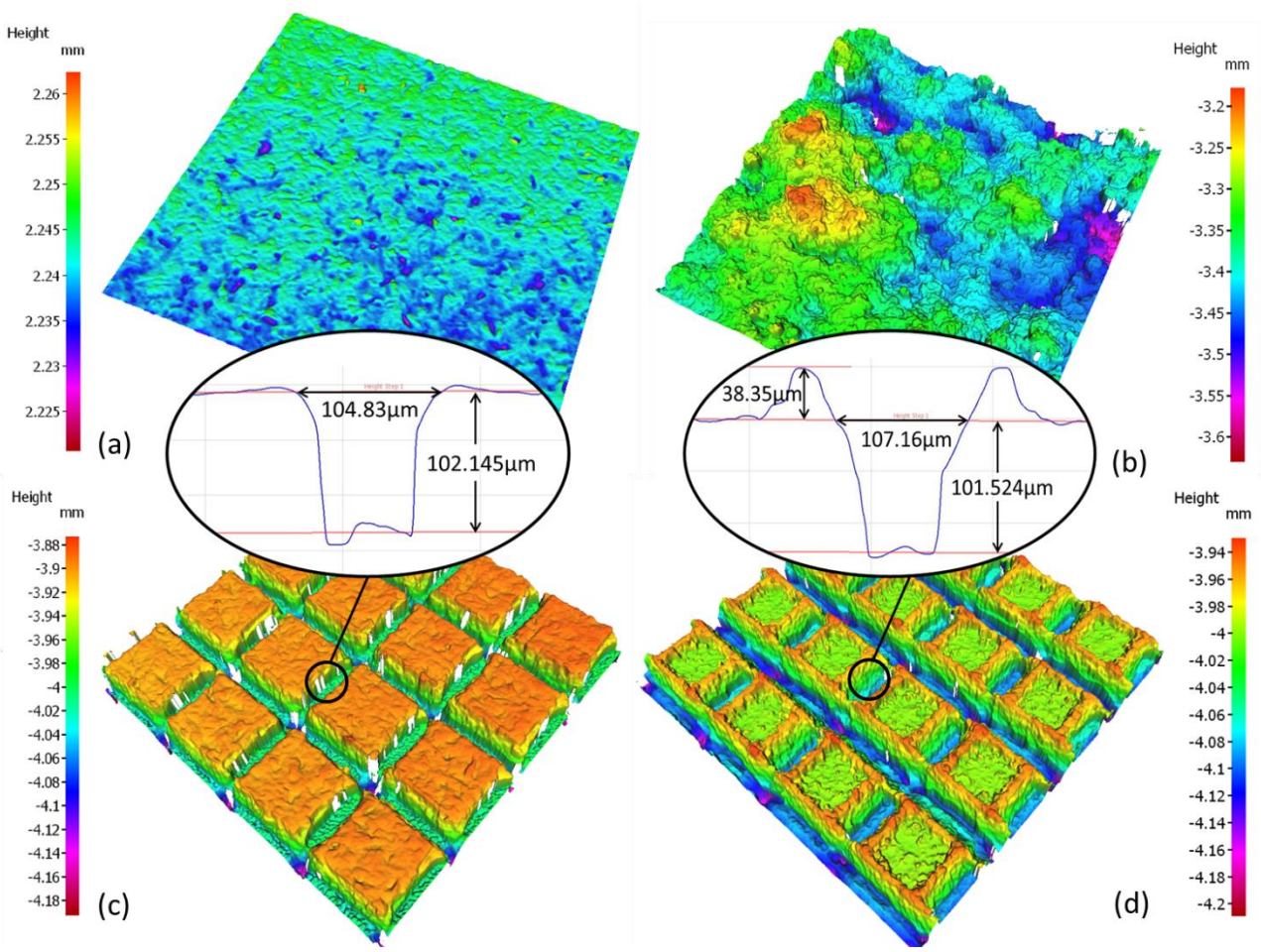

Figure 3.2 Topography measurements of (a) B surface
(b) HA surface (c) FS surface (d) NS surface

The 3D surface profiles were made with the 10x objective of the Alicona G5 microscope. Using the same magnification, the arithmetical mean height (S_a) and root mean square height (S_q) values of the blasted and HA coated specimens were calculated over a 1.62mm^2 area (10x objective's field of view). The average S_a and S_q values, taken from 5 surfaces, for the B surface were 60 µm and 60 µm, respectively, compared with 89 µm and 106 µm for the HA coated surface, making it the roughest surface by a significant margin with values higher than the 100 µm deep grooves of the NS and FS surfaces. As for the NT surface, the S_a and S_q values were measured using the 100x objective, for being orders of magnitude smoother, over a 0.0256mm^2

area (100x objective's field of view) and they were 0.05 μm and 0.07 μm respectively, a slight increase over the mirror finish.

The desired groove width and depth was produced with both FS and NS laser sources with deviations less than 10%. However, the resulting topographies differ considerably; the longer pulse duration used for the NS samples resulted in a significant recast bulges along the grid edges of the CoCrMo disks that enclosed non-processed areas in-between the grooves. Furthermore, after producing the grooves in one direction, the processing of perpendicular grooves to form the grids resulted in re-deposition of molten material where they intersected the existing ones.

In contrast, due to the nature of ultrashort pulsed laser processing that is also commonly referred to as "cold ablation", no recast budges were observed on the FS disks. The non-processed area retained its blasted finish characteristics while the grooves' intersection remained open in both directions.

Additionally, the grooves of the NS surfaces exhibited a larger draft angle when compared to the almost-vertical walls obtained along the FS grooves, which could be attributed to the higher thermal load when longer pulses were used and consequently a high amont of molted material and slashes along the groves.

3.3.2 Scanning Electron Microscopy

The SEM micrographs of all 6 investigated surfaces are presented in Figure 3.3

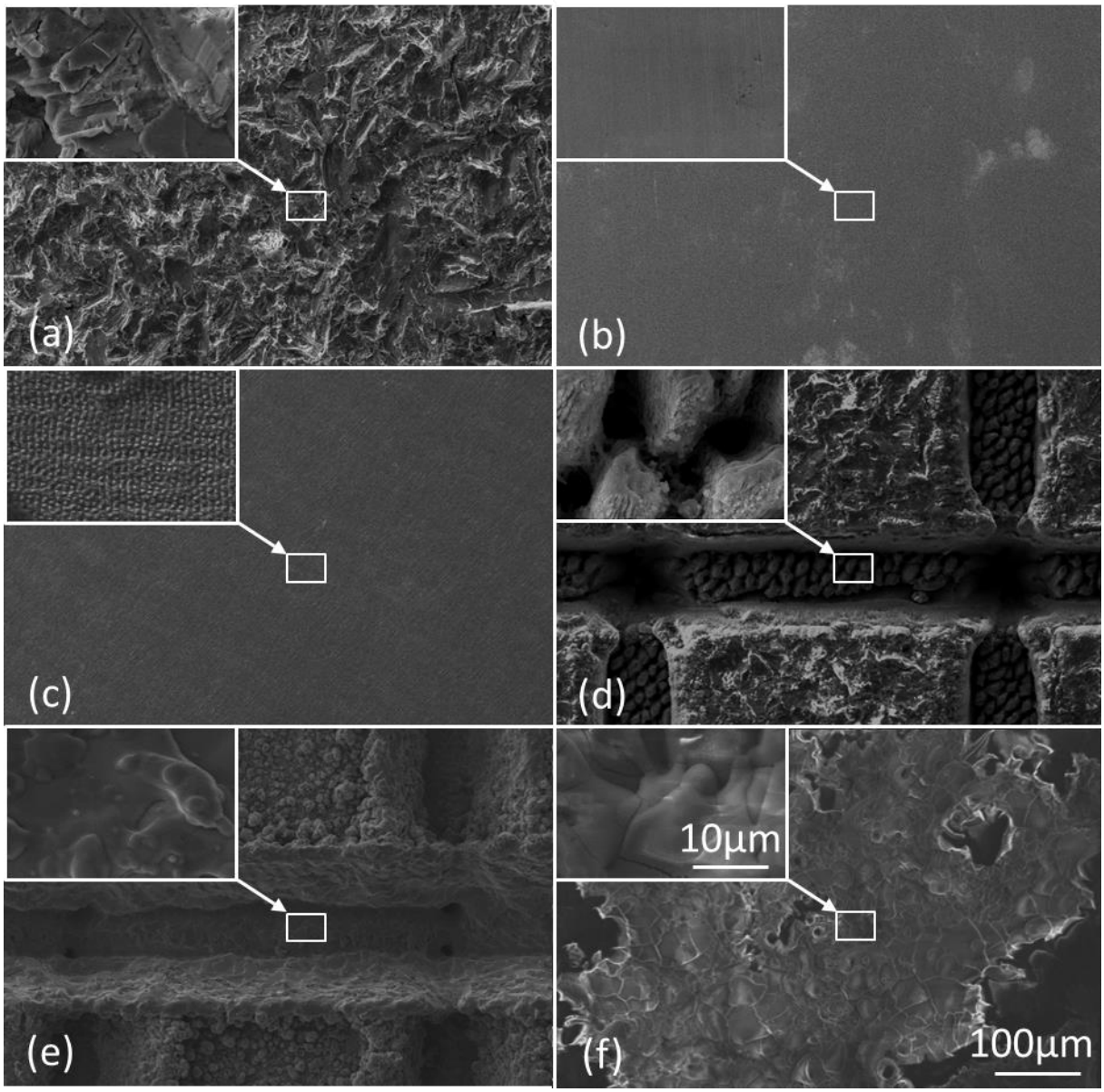

Figure 3.3 SEM micrographs of: (a) B surface; (b) P surface; (c) NT surface; (d) FS surface; (e) NS surface and (f) HA surface.

Scale bars are valid for all images.

It is evident that apart from the NT and P surfaces, the CoCrMo disks have a significant roughness. The B surface had uniform roughness whereas the FS, NS and HA surfaces were more irregular as seen from both the SEM images and focus variation microscopy, see also section 3.3.1. The difference between the NS and FS surfaces is depicted in more detail in µ. Regarding the NT surface, a hexagonal sub-micron

array resembling the corneal surface of insects was successfully formed on the initially polished surface (Figure 3.4d windowed). The distance between two consecutive sub-micron features is just under the wavelength of the ultrashort laser source used: 600-700 nm in this case. This has been thoroughly documented when producing LIPSS with an ultrashort pulsed laser [48]. Nano bumps were formed instead of linear ripples due to the 90º rotation of the samples between the first and second scans together with the use of lower power in the second scan, and as a result the ripples from the two scans intersected to form the nano-bumps. It is important to stress that the power settings in the two scans are very important to generate this particular NT surfaces. In particular, if the second scan is performed with the same laser power, the first set of ripples will be erased while no LIPSS would be generated if the power settings are too low. The energy levels should thus be just sufficent to ablate the peaks of the first set of LIPSS, giving this particular bio-inspired sub-micron topography, see table 3.1 for specific parameters on CoCrMo. This was determined experimentally, by varying the laser energy in the second scan in small increments until the desired pattern is achieved.

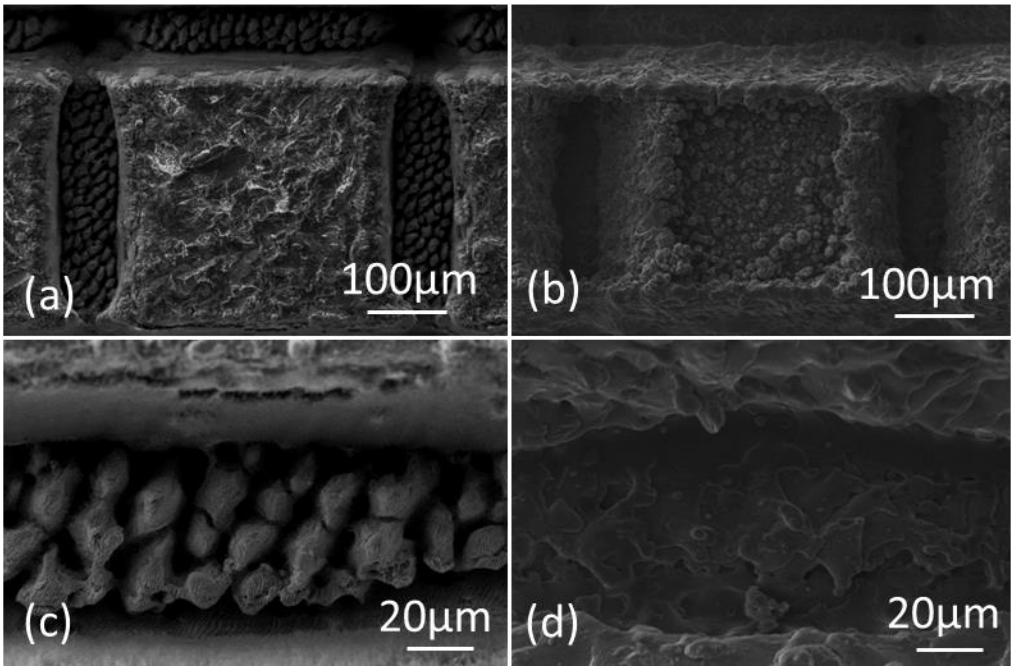

Figure 3.4 SEM micrographs of (a) FS surface (b) NS surface
(c) FS groove (d) NS groove

The differences between the FS and NS surfaces, especially the effects of the 2 different pulse durations, are depicted in more detail in Figure 3.4. In particular, the unprocessed areas between the grooves of the NS samples are covered with re-solidified molten CoCrMo while the recast bulges are very prominent at the intersections, even closing the first set of grooves, and also along the edges, as can also be seen in Figure 3.2. In contrast, the untreated areas of the FS samples retained their blasted surface characteristics, no recast formations along the grooves were observed and the first set of grooves was only narrowed at the intersections. Taking a closer look at the bottom of the grooves (Figure 3.4c & d), it can be seen that the processed surface areas with the longer 220ns pulses were re-melted and smoothened whereas a self-organised hierarchical micro/nano morphology was observed in the FS groove as a result of multiple passes, in particular the accumulated laser fluence [49]. The morphology is of similar scale to that of the rose petals

examined by Li et al. [18], nano ripples can be observed on the top of the micro features that measure between 15 and 20 µm.

3.3.3 Surface Wettability

The contact angle (CA) values are shown in Figure 3.5.

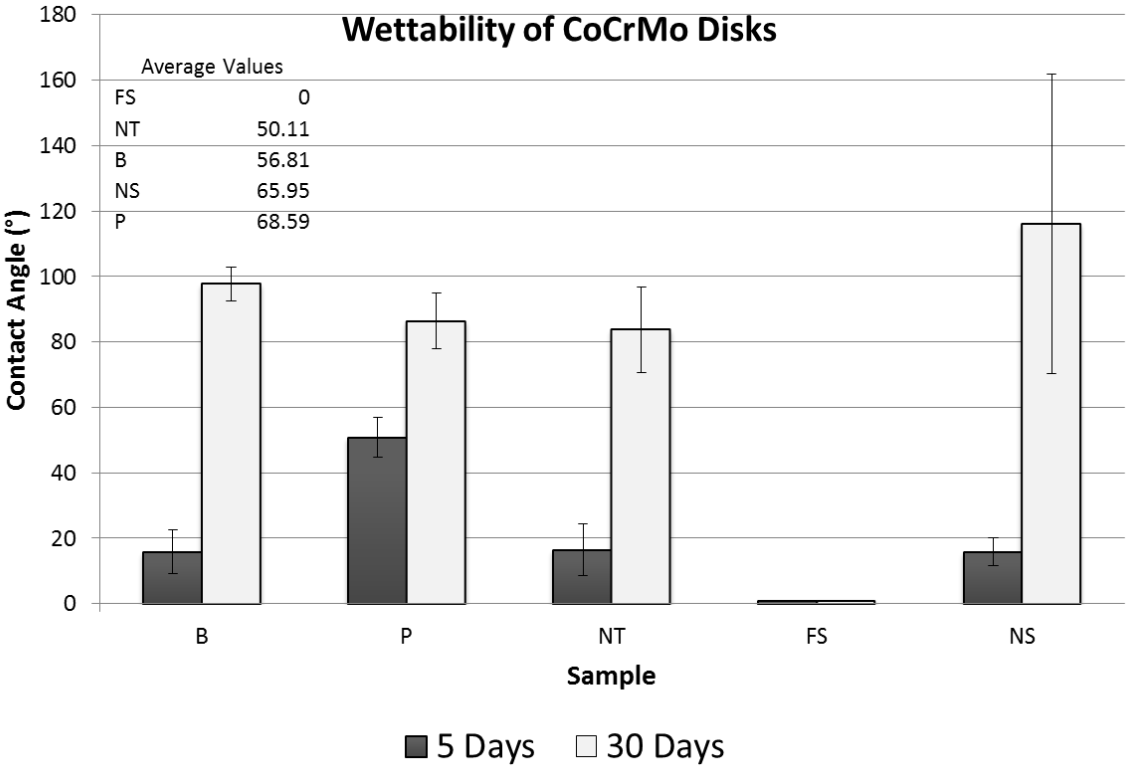

Figure 3.5 Contact angle of the different uncoated CoCrMo surfaces (n=5)

Table 3.3 Contact angle data

	5 Days	Mean (degree)	STD	30 Days	Mean (degree)	STD
Cast	16.7	15.846	6.5631	89.48	97.764	5.1951
	25.99			103		
	10.7			99.4		
	16.46			100.5		
	9.38			96.44		
Polished	48.12	50.814	6.1484	89.59	86.374	8.46
	57.76			99.38		
	56.97			84.33		
	46.96			80.31		
	44.26			78.26		
Nano-Textured	10.85	16.461	7.9812	103.5	83.774	13.041
	6.917			78.01		
	24.82			86.31		
	24.29			83.12		
	15.43			67.93		
Femtosecond	0	0	0	0	0	0
	0			0		
	0			0		
	0			0		
	0			0		
Nanosecond	12.81	15.834	2.2377	74.51	116.06	39.735
	18.9			83.17		
	14.89			134		
	16.59			172.5		
	15.98			116.12		

Looking at the average CA values 5 days after laser texturing, all samples were hydrophilic, with 0^o CA for the FS sample processed with the ultrashort laser, while the CA values for the NS, NT and B samples were similar at ~15^o, only the polished disks exhibited a higher CA at ~50^o. With time (30 days), all CA values increased except for the FS sample. This increase in CA values has been observed by many researchers and is commonly attributed to changes in surface chemistry [50, 51].

Furthermore, the large CA deviation of NS samples after 30 days is due to the directional nature of the surface. In fact, the samples exhibited semi-hydrophilic

properties in the direction of the open grooves and were hydrophobic in the direction of the closed ones while the value in Figure 3.5. is the average of both. This is due to some capillary effects that have led to droplets spreading in the direction of the open grooves. However, the droplets still did not flow inside the grooves as reflected by the lowest contact angle of 70˚. Luo et al. [52] argued that the cell-like structures (unprocessed areas enclosed by the molten material) repel the water droplets due to some entrapped air. Thus, the NS surface exhibits a mixed Cassie-Baxter (CB) - Wenzel wetting state, especially a transitional state between CB and Wenzel regimes, similar to the one seen with pigeon feathers [53].

On the other hand, the FS samples exhibited a complete Wenzel state of wetting where there was complete contact between the liquid and the solid surface, reflected by the contact angle of 0˚. This wetting state can be attributed to the lack of ‘air pockets’ due to the absence of molten material around the edges of the grooves and the morphology at the bottom of the grooves that prevented the air being compressed as it is open to the environment [54].

3.3.4 Saos-2 Cell Proliferation and Morphology

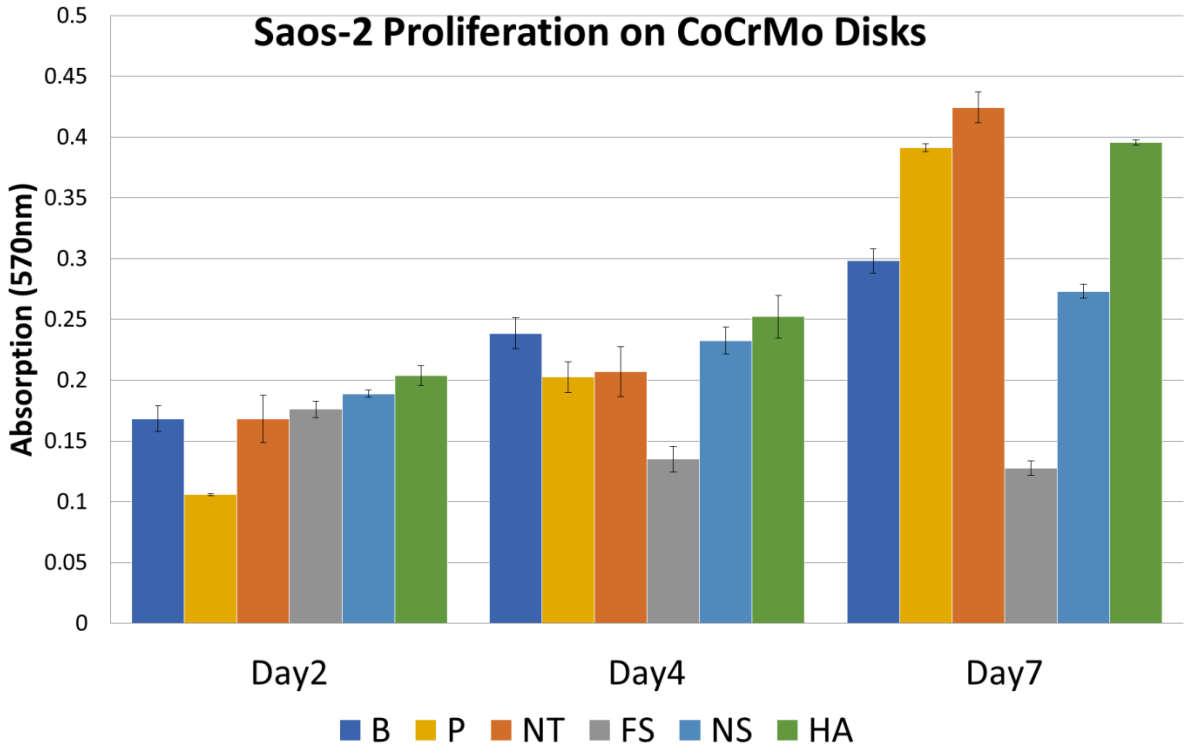

Figure 3.6 Proliferation of Saos-2 cells on the 6 different CoCrMo surfaces after 2, 4 and 7 days. (n=3, statistical significance indicated by $p<0.05$)

From the MTT assay, a number of conclusions can be drawn. Initial cell adhesion is favourable on surfaces with higher roughness (see section 3.3.1 for roughness values), this is reflected in the higher cell metabolic activity on the B, FS, NS and HA surfaces when compared to the P on Day2. However, the rate of proliferation is much in favour of surfaces with lower S_a values (see section 3.3.1 for roughness values). In fact, the P and NT samples exhibited the highest rates of proliferation at 93.21% and 105.1%, respectively, between Day4 and Day7. In contrast, cells on the hydroxyapatite coated disk increased by 56.84% in the same time period. This phenomenon was also

seen with epithelial cells on different titanium surfaces [55]. This could be attributed to the mechanical micro-anchorage of the cells onto the disks with micro-topography. The NT surface exhibited high levels of initial adhesion, comparable to those of the four rough surfaces (B, FS, NS, HA), yet it also showed the highest rate of proliferation between Day4 and Day7. This highlights the important role of sub-micron features in terms of cell adhesion.

At the end of the assay on Day7, the Sub-micron Textured CoCrMo disk showed the highest cell metabolic activity.

From the ANOVA, it can be concluded that the topography is a very significant factor with a p-value of $0.001<<<0.05$. As for the contribution percentages, they are 29.15 and 39.10% for the factors Topography and Day respectively.

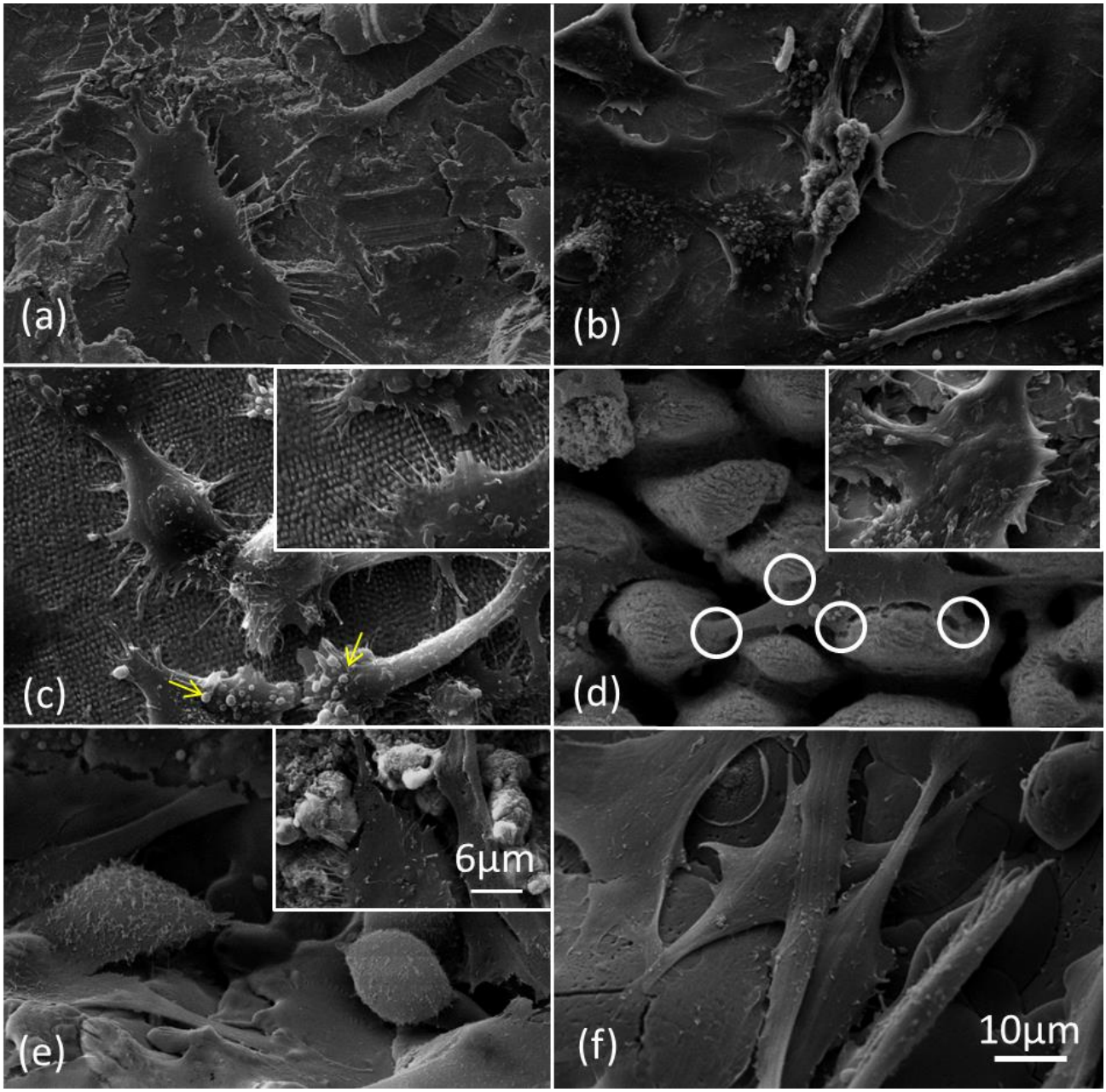

Figure 3.7 Representative SEM micrographs of Saos-2 cells at day 4 on: (a) B surface; (b) P surface; (c) NT surface; (d) FS surface; (e) NS surface and (f) HA surface.

Scale bars are valid for all images.

Cell adhesion and proliferation was monitored by SEM at day 4 (Figure 3.7). Cells were not confluent at this time on any of the surfaces except for the HA surface (Figure 3.7f). On the B surface (Figure 3.7a) the Saos-2 cells were relatively flat on the sample

but less spread than in the P samples, as was seen on Titanium surfaces by Degasne et al. [56]. In some areas of the P surface (Figure 3.7b) the cells appeared almost confluent and were completely flattened and spread out on the surface with few exceptions, as is typical of such surfaces [56]. On the NT surface (Figure 3.7c) the cells had a raised profile and several filopodia can be seen attached to the nanofeatures (Figure 3.7c windowed). Blebs (arrows) were seen in the cell membrane of many cells on this surface, which could be indicative of secretive metabolic activity. The filopodia anchoring the cells to the sub-micron topography explains the high initial adhesion on Day2 unlike the P surfaces. Moreover, the cells on this surface did not show signs of directionality, as was hypothesised, which is otherwise common with LIPSS surfaces [46]. On the FS surface (Figure 3.7d) there was no cell growth inside the grooves and only occasional cells were seen, as pictured, spanning the hierarchical features. Cells in the untextured areas had the same characteristics as on the blasted surface (Figure 3.7d windowed and Figure 3.7a). On the NS surface (Figure 3.7e) the cells were concentrated in the grooves as expected, which could be attributed to some capillary action of the cell media, but a few cells were also present on the untreated area, they had a similar morphology to those found on the B surfaces (Figure 3.7e windowed). On the HA surface (Figure 3.7f) the cells appeared elongated and there appeared to be more than one cell layer developing.

Both B and NS surfaces showed similar levels of proliferation and comparable morphologies. This suggests that the anchoring and growth mechanisms are similar on both surfaces with micro-topography.

Generally, higher growth was expected on the HA surfaces compared to uncoated metallic surfaces. Okumura et al. reported that Saos-2 cells settled and differentiated earlier on HA compared to pure titanium [57]. This was indeed the case with the

CoCrMo alloy samples as well, especially a higher growth and adhesion was seen on the HA samples on Day2 and Day4.

The differences in water contact angle and cell attachment between the FS and NS samples can therefore be attributed to the hierarchical structures at the bottom of the FS grooves and the splashes of molten material. Those differences led to changes in the wetting states, i.e. Cassie-Wenzel for the NS samples and Wenzel for the FS samples, and thus there was no correlation between CA and cell attachment in this case. However, there is some correlation between the surface response on the P and NT surfaces. Especially, the P and NT surfaces exhibited almost identical wetting behaviours owing to their comparable surface roughness values and thus high hydrophilicity let to a greater attachment and proliferation.

Osteoblast cells have been seen to grow across grooves much wider than the distance between 2 consecutive hierarchical structures seen in the FS grooves. In fact, De Luca et al. reported that primary osteoblast cells grew across 40 µm wide grooves on the surface of 316 L austenitic stainless steel [58]. This indicates that the morphology of the hierarchical structures, and not the distance in between them, caused the cell growth inhibition. Moreover, the cells' points of contact were seen almost exclusively on the side of the hierarchical structures (Figure 3.7d, circles) which could indicate that the cells could not attach to the top of the said structures.

3.4 Conclusions

Six different CoCrMo samples with different surface topography were studied for osteoblast-like Saos-2 cell morphology and proliferation. In particular, the cell responses after applying three different laser texturing procedures were compared to

those obtained on blasted and polished specimens and also samples with a commercially-used hydroxyapatite coating. The following conclusions were made based on the obtained results:

1. Saos-2 cell adhesion occurred on all the CoCr surfaces and the surface topography was an important factor governing both cell morphology and proliferation.
2. A higher roughness encourages initial cell adhesion however smoother/planner surfaces facilitate cell proliferation.
3. The highest metabolic activity occurred on Day 7 on the NT surface, as shown by the MTT assay. This can be attributed to both the anchoring effects of the sub-micron textures and also the high proliferation levels of smooth surfaces. In addition, the cells on the NT samples that had bio-inspired sub-micron topography did not show any signs of directionality.
4. Surface topography is a more significant factor than surface energy in Saos-2 cell attachment and proliferation. Controlling the micron (cell size) and sub-micron scales of implant surfaces could lead to much improved biological responses.
5. Correlation between CA and cell proliferation is only valid when both the wetting behaviours and surface roughness values are comparable.
6. Long lasting super hydrophilic, 0˚ CA, surfaces can be produced via ultrashort pulsed laser structuring, namely by producing micro grooves with hierarchical micro/nano topography at the bottom, FS samples.
7. Saos-2 cells grew in the micro-grooves produced with the longer 220ns laser pulses but not in the ones produced with the ultrashort pulses, in fact the FS grooves inhibited cell attachment and growth. This suggests that the self-

organized hierarchical micro/nano structures found in the FS grooves could be used to potentially control cell migration.

Based on the findings in this research, it can be argued that the potential ideal CoCrMo implant surface should be a combination of micro-scale structures and sub-micro features. In particular, the micro-scale structures would facilitate both the mechanical anchorage with the bone and also offer a better initial osteoblast cell adherence, while the smooth surfaces with sub-micron features would improve proliferation and growth without compromising adherence. Such surfaces can be produced simultaneously by employing femtosecond laser sources and thus to selectively modify implants both at the micro and sub-micro scales in one processing step.

Acknowledgments

The research reported in this paper was carried out in collaboration with MatOrtho Ltd. and was supported by two European Commission H2020 projects, i.e. the ITN programme “European ESRs Network on Short Pulsed Laser Micro/Nanostructuring of Surfaces for Improved Functional Applications” (Laser4Fun) and the FoF programme “High-Impact Injection Moulding Platform for mass-production of 3D and/or large micro-structured surfaces with Antimicrobial, Self-cleaning, Anti-scratch, Anti-squeak and Aesthetic functionalities” (HIMALAIA). In addition, the work was carried out within the framework of the UKIERI DST programme “Surface functionalisation for food, packaging, and healthcare applications”.

References

1. Chen, Q., & Thouas, G. A. (2015). Metallic implant biomaterials. Materials Science and Engineering: R: Reports, 87, 1-57.
2. Shinohara, K., Takigawa, T., Tanaka, M., Sugimoto, Y., Arataki, S., Yamane, K., ... & Sarai, T. (2016). Implant failure of titanium versus cobalt-chromium growing rods in early-onset scoliosis. Spine, 41(6), 502-507.
3. Serhan, H., Mhatre, D., Newton, P., Giorgio, P., & Sturm, P. (2013). Would CoCr rods provide better correctional forces than stainless steel or titanium for rigid scoliosis curves?. Clinical Spine Surgery, 26(2), E70-E74.
4. Anon., “National Joint Registry for England and Wales Summary to the 7th Annual Report,” 2009. Retrieved from http://www.njrcentre.org.uk/
5. Anon., “Johnson and Johnson. Company Literature and Marketing,” PFC Sigma Cobalt-Chrome, Leeds, 2010. Retrieved from https://www.depuysynthes.com/
6. Wood, A. M., Heil, K. M., Brenkel, I. J., & Walmsley, P. (2018). Press fit condylar cobalt chrome sigma total knee arthroplasty: No difference to original design at five year point. Journal of Arthroscopy and Joint Surgery, 5(1), 15-18.
7. Vallittu, P. K., & Kokkonen, M. (1995). Deflection fatigue of cobalt-chromium, titanium, and gold alloy cast denture clasp. The Journal of Prosthetic Dentistry, 74(4), 412-419.
8. Savitha, P. N., Lekha, K. P., & Nadiger, R. K. (2015). Fatigue resistance and flexural behavior of acetal resin and chrome cobalt removable partial denture clasp: an in vitro study. European Journal of Prosthodontics, 3(3), 71.

9. Zaman, H. A., Sharif, S., Kim, D. W., Idris, M. H., Suhaimi, M. A., & Tumurkhuyag, Z. (2017). Machinability of Cobalt-based and Cobalt Chromium Molybdenum Alloys-A Review. Procedia Manufacturing, 11, 563-570.

10. Delaunay, C., Petit, I., Learmonth, I. D., Oger, P., & Vendittoli, P. A. (2010). Metal-on-metal bearings total hip arthroplasty: the cobalt and chromium ions release concern. Orthopaedics & Traumatology: Surgery & Research, 96(8), 894-904.

11. De Villiers, D., Banfield, S., Housden, J., & Shelton, J. (2016). Silver Chromium Nitride Coatings On Cobalt Chrome Alloy To Reduce Cobalt Ion Release And Prevent Infections. Bone Joint J, 98(SUPP 7), 108-108.

12. Friedman, R. J., Bauer, T. W., Garg, K., Jiang, M., An, Y. H., & Draughn, R. A. (1995). Histological and mechanical comparison of hydroxyapatite-coated cobalt-chrome and titanium implants in the rabbit femur. Journal of Applied Biomaterials, 6(4), 231-235.

13. Lacefield, W. R. (1988). Hydroxyapatite coatings. Annals of the New York academy of sciences, 523(1), 72-80.

14. Nimb, L., Gotfredsen, K., & Steen Jensen, J. (1993). Mechanical failure of hydroxyapatite-coated titanium and cobalt-chromium-molybdenum alloy implants. An animal study. Acta orthopaedica belgica, 59, 333-333.

15. Hailer, N. P., Lazarinis, S., Mäkelä, K. T., Eskelinen, A., Fenstad, A. M., Hallan, G., ... & Kärrholm, J. (2015). Hydroxyapatite coating does not improve uncemented stem survival after total hip arthroplasty! An analysis of 116,069 THAs in the Nordic Arthroplasty Register Association (NARA) database. Acta orthopaedica, 86(1), 18-25.

16. Sousa, M. P., & Mano, J. F. (2017). Cell-adhesive bioinspired and catechol-based multilayer freestanding membranes for bone tissue engineering. Biomimetics, 2(4), 19.

17. Wang, F., Shi, L., He, W. X., Han, D., Yan, Y., Niu, Z. Y., & Shi, S. G. (2013). Bioinspired micro/nano fabrication on dental implant–bone interface. Applied Surface Science, 265, 480-488.

18. Li, P., Dou, X., Feng, C., & Schönherr, H. (2018). Enhanced cell adhesion on a bio-inspired hierarchically structured polyester modified with gelatin-methacrylate. Biomaterials science, 6(4), 785-792.

19. Etsion, I. (2005). State of the art in laser surface texturing. Transactions of the ASME-F-Journal of Tribology, 127(1), 248.

20. Liu, X., Chu, P. K., & Ding, C. (2004). Surface modification of titanium, titanium alloys, and related materials for biomedical applications. Materials Science and Engineering: R: Reports, 47(3), 49-121.

21. Mendonça, G., Mendonça, D. B., Aragao, F. J., & Cooper, L. F. (2008). Advancing dental implant surface technology–from micron-to nanotopography. Biomaterials, 29(28), 3822-3835.

22. Klokkevold, P. R., Nishimura, R. D., Adachi, M., & Caputo, A. (1997). Osseointegration enhanced by chemical etching of the titanium surface. A torque removal study in the rabbit. Clinical oral implants research, 8(6), 442-447.

23. Cho, S. A., & Jung, S. K. (2003). A removal torque of the laser-treated titanium implants in rabbit tibia. Biomaterials, 24(26), 4859-4863.

24. Mariscal-Muñoz, E., Costa, C. A., Tavares, H. S., Bianchi, J., Hebling, J., Machado, J. P., ... & Souza, P. P. (2016). Osteoblast differentiation is enhanced by a nano-to-micro hybrid titanium surface created by Yb: YAG laser irradiation. Clinical oral investigations, 20(3), 503-511.

25. Shah, F. A., Johansson, M. L., Omar, O., Simonsson, H., Palmquist, A., & Thomsen, P. (2016). Laser-modified surface enhances osseointegration and biomechanical anchorage of commercially pure titanium implants for bone-anchored hearing systems. PloS one, 11(6), e0157504.

26. Buser, D., Broggini, N., Wieland, M., Schenk, R. K., Denzer, A. J., Cochran, D. L., ... & Steinemann, S. G. (2004). Enhanced bone apposition to a chemically modified SLA titanium surface. Journal of dental research, 83(7), 529-533.

27. Zhao, G., Schwartz, Z., Wieland, M., Rupp, F., Geis-Gerstorfer, J., Cochran, D. L., & Boyan, B. D. (2005). High surface energy enhances cell response to titanium substrate microstructure. Journal of biomedical materials research Part A, 74(1), 49-58.

28. Schwarz, F., Ferrari, D., Herten, M., Mihatovic, I., Wieland, M., Sager, M., & Becker, J. (2007). Effects of surface hydrophilicity and microtopography on early stages of soft and hard tissue integration at non-submerged titanium implants: an immunohistochemical study in dogs. Journal of periodontology, 78(11), 2171-2184.

29. Vlacic-Zischke, J., Hamlet, S. M., Friis, T., Tonetti, M. S., & Ivanovski, S. (2011). The influence of surface microroughness and hydrophilicity of titanium on the up-regulation of TGFβ/BMP signalling in osteoblasts. Biomaterials, 32(3), 665-671.

30. Le Guéhennec, L., Soueidan, A., Layrolle, P., & Amouriq, Y. (2007). Surface treatments of titanium dental implants for rapid osseointegration. Dental materials, 23(7), 844-854.

31. Wennerberg, A., Jimbo, R., Stübinger, S., Obrecht, M., Dard, M., & Berner, S. (2014). Nanostructures and hydrophilicity influence osseointegration: a biomechanical study in the rabbit tibia. Clinical oral implants research, 25(9), 1041-1050.

32. Niino, H., & Yabe, A. (1993). Surface modification and metallization of fluorocarbon polymers by excimer laser processing. Applied Physics Letters, 63(25), 3527-3529.

33. Okabe, Y., Kurihara, S., Yajima, T., Seki, Y., Nakamura, I., & Takano, I. (2005). Formation of super-hydrophilic surface of hydroxyapatite by ion implantation and plasma treatment. Surface and Coatings Technology, 196(1), 303-306.

34. Zhong, H., Hu, Y., Wang, Y., & Yang, H. (2017). TiO2/silane coupling agent composed of two layers structure: A super-hydrophilic self-cleaning coating applied in PV panels. Applied energy, 204, 932-938.

35. Rupp, F., Scheideler, L., Olshanska, N., De Wild, M., Wieland, M., & Geis-Gerstorfer, J. (2006). Enhancing surface free energy and hydrophilicity through chemical modification of microstructured titanium implant surfaces. Journal of Biomedical Materials Research Part A, 76(2), 323-334.

36. Kenar, H., Akman, E., Kacar, E., Demir, A., Park, H., Abdul-Khaliq, H., ... & Karaoz, E. (2013). Femtosecond laser treatment of 316L improves its surface nanoroughness and carbon content and promotes osseointegration: An in vitro evaluation. Colloids and Surfaces B: Biointerfaces, 108, 305-312.

37. Raimbault, O., Benayoun, S., Anselme, K., Mauclair, C., Bourgade, T., Kietzig, A. M., ... & Donnet, C. (2016). The effects of femtosecond laser-textured Ti-6Al-4V on wettability and cell response. Materials Science and Engineering: C, 69, 311-320.

38. Fadeeva, E., Truong, V. K., Stiesch, M., Chichkov, B. N., Crawford, R. J., Wang, J., & Ivanova, E. P. (2011). Bacterial retention on superhydrophobic titanium surfaces fabricated by femtosecond laser ablation. Langmuir, 27(6), 3012-3019.

39. Bizi-Bandoki, P., Benayoun, S., Valette, S., Beaugiraud, B., & Audouard, E. (2011). Modifications of roughness and wettability properties of metals induced by femtosecond laser treatment. Applied Surface Science, 257(12), 5213-5218.

40. Kietzig, A. M., Hatzikiriakos, S. G., & Englezos, P. (2009). Patterned superhydrophobic metallic surfaces. Langmuir, 25(8), 4821-4827.

41. Mirhosseini, N., Crouse, P. L., Schmidth, M. J. J., Li, L., & Garrod, D. (2007). Laser surface micro-texturing of Ti–6Al–4V substrates for improved cell integration. Applied surface science, 253(19), 7738-7743.

42. Qin, L., Zeng, Q., Wang, W., Zhang, Y., & Dong, G. (2014). Response of MC3T3-E1 osteoblast cells to the microenvironment produced on Co–Cr–Mo alloy using laser surface texturing. Journal of materials science, 49(6), 2662-2671.

43. Blagodatski, A., Sergeev, A., Kryuchkov, M., Lopatina, Y., & Katanaev, V. L. (2015). Diverse set of Turing nanopatterns coat corneae across insect lineages. Proceedings of the National Academy of Sciences, 112(34), 10750-10755.

44. Pautke, C., Schieker, M., Tischer, T., Kolk, A., Neth, P., Mutschler, W., & Milz, S. (2004). Characterization of osteosarcoma cell lines MG-63, Saos-2 and U-2

OS in comparison to human osteoblasts. Anticancer research, 24(6), 3743-3748.

45. Lee, M. H., Oh, N., Lee, S. W., Leesungbok, R., Kim, S. E., Yun, Y. P., & Kang, J. H. (2010). Factors influencing osteoblast maturation on microgrooved titanium substrata. Biomaterials, 31(14), 3804-3815.

46. Rebollar, E., Frischauf, I., Olbrich, M., Peterbauer, T., Hering, S., Preiner, J., ... & Heitz, J. (2008). Proliferation of aligned mammalian cells on laser-nanostructured polystyrene. Biomaterials, 29(12), 1796-1806.

47. Mosmann, T. (1983). Rapid colorimetric assay for cellular growth and survival: application to proliferation and cytotoxicity assays. Journal of immunological methods, 65(1-2), 55-63.

48. Bonse, J., Krüger, J., Höhm, S., & Rosenfeld, A. (2012). Femtosecond laser-induced periodic surface structures. Journal of Laser Applications, 24(4), 042006.

49. Nayak, B. K., & Gupta, M. C. (2010). Self-organized micro/nano structures in metal surfaces by ultrafast laser irradiation. Optics and Lasers in Engineering, 48(10), 940-949.

50. Garcia-Giron, A., Romano, J. M., Liang, Y., Dashtbozorg, B., Dong, H., Penchev, P., & Dimov, S. S. (2018). Combined surface hardening and laser patterning approach for functionalising stainless steel surfaces. Applied Surface Science, 439, 516-524.

51. Bizi-Bandoki, P., Valette, S., Audouard, E., & Benayoun, S. (2013). Time dependency of the hydrophilicity and hydrophobicity of metallic alloys subjected to femtosecond laser irradiations. Applied Surface Science, 273, 399-407.

52. Luo, B. H., Shum, P. W., Zhou, Z. F., & Li, K. Y. (2010). Surface geometrical model modification and contact angle prediction for the laser patterned steel surface. Surface and Coatings Technology, 205(7), 2597-2604.

53. Bormashenko, E., Bormashenko, Y., Stein, T., Whyman, G., & Bormashenko, E. (2007). Why do pigeon feathers repel water? Hydrophobicity of pennae, Cassie–Baxter wetting hypothesis and Cassie–Wenzel capillarity-induced wetting transition. Journal of colloid and interface science, 311(1), 212-216.

54. Ran, C., Ding, G., Liu, W., Deng, Y., & Hou, W. (2008). Wetting on nanoporous alumina surface: transition between Wenzel and Cassie states controlled by surface structure. Langmuir, 24(18), 9952-9955.

55. Cochran, D. L., Simpson, J., Weber, H. P., & Buser, D. (1994). Attachment and growth of periodontal cells on smooth and rough titanium. International Journal of Oral & Maxillofacial Implants, 9(3).

56. Degasne, I., Basle, M. F., Demais, V., Hure, G., Lesourd, M., Grolleau, B., ... & Chappard, D. (1999). Effects of roughness, fibronectin and vitronectin on attachment, spreading, and proliferation of human osteoblast-like cells (Saos-2) on titanium surfaces. Calcified tissue international, 64(6), 499-507.

57. Okumura, A., Goto, M., Goto, T., Yoshinari, M., Masuko, S., Katsuki, T., & Tanaka, T. (2001). Substrate affects the initial attachment and subsequent behavior of human osteoblastic cells (Saos-2). Biomaterials, 22(16), 2263-2271.

58. De Luca, A. C., Zink, M., Weidt, A., Mayr, S. G., & Markaki, A. E. (2015). Effect of microgrooved surface topography on osteoblast maturation and protein

adsorption. Journal of Biomedical Materials Research Part A, 103(8), 2689-2700.

CHAPTER 4: EFFECTS OF LASER PROCESSING CONDITIONS ON WETTABILITY AND PROLIFERATION OF SAOS-2 CELLS ON COCRMO ALLOY SURFACES

A. Batal[1]✉, A. Michalek[1], A. Garcia-Giron[1], V. Nasrollahi[1], P. Penchev[1], R. Sammons[2], S. Dimov[1]

[1] Department of Mechanical Engineering, University of Birmingham, Edgbaston, Birmingham, B15 2TT, UK

[2] School of Dentistry, University of Birmingham, Edgbaston, Birmingham, B5 7EG, UK

This research was published as a full-length article in *Advanced Optical Technologies* (2019):

Batal, A., Michalek, A., Garcia-Giron, A., Nasrollahi, V., Penchev, P., Sammons, R., & Dimov, S. (2019). Effects of laser processing conditions on wettability and proliferation of Saos-2 cells on CoCrMo alloy surfaces. Advanced Optical Technologies.

Keywords: Laser Surface Texturing; Surface Functionalization; Laser Induced Periodic Surface Structures; Cobalt Chrome Molybdenum; Osseointegration

Authors' Contributions:

A. Batal

Main author, conducted the laser experiments and functional tests.

A. Michalek

Assisted with LIPSS optimization and characterization

A. Garcia-Giron

Assisted with sample preparation and wettability analysis

V. Nasrollahi

Assisted with SEM imaging

P. Penchev

Assisted with laser machining setup and supervision

R. Sammons

Supervision and proofreading

S. Dimov

Supervision and proofreading

Abstract

Any processing disturbances in laser surface texturing (LST) could compromise the resulting surface topography and thus their desired functional response. Disturbances such as focal plane offsets and beam incident angle variations are always present in LST processing of 3D parts and can affect the surface morphology. In this research the effects of these laser processing disturbances in producing laser induced surface structures (LIPSS) on CoCrMo alloy substrates were investigated. In particular, these two disturbances were considered as laser processing variables to determine their effects on functional responses of LIPSS treated surfaces, i.e. surface wettability and the proliferation of Saos-2 osteoblast-like cells were evaluated. It was found that the changes of laser processing conditions led to a decrease in surface wettability and Saos-2 cells proliferation. In addition, a correlation between surface wettability and cell proliferation on LIPSS treated surface was identified and conclusions made about the effects of investigated process disturbances on the functional response of LIPSS treated CoCrMo substrates.

4.1 Introduction

The functionalization of surfaces has become an integral part in the design of innovative products with high commercial potential and advanced functionalities. In particular, it allows the embedment of new properties foreign to the underlying substrate material, for instance turning a hydrophilic surface into a super hydrophobic one [1], or the enhancement of existing properties such as improving the biological response of Titanium alloys [2].

There are various approaches for functionalizing surfaces such as changing the surface chemistry [3], the material's microstructure on the surface [4] or the surface topography [5] and also some combinations of them. Moreover, there is a diverse range of processes available to achieve such surface functionalities. For example, Gholami et al. investigated the effect of annealing temperature on the pitting corrosion resistance of 2205 duplex stainless steel [6], Zhenyu et al. produced hydrophobic surfaces on PMMA and Ti-6 Al-4V alloy substrates via micro-milling [7], Kumar et al. improved the cutting performance of Al_2O_3/TiCN composite ceramic tools by producing micro-grooves on their rake surface via WEDM [8], Arisoy et al. produced antibacterial and antifouling surfaces via nanoimprint lithography [9], finally Bang et al. enhanced the biological response of pure titanium via sandblasting and acid etching [10]. Another process that has been attracting a lot of interest recently from both industry and research is Laser Surface Texturing (LST). LST offers a number of advantages over competing technologies. In particular, LST can be deployed to process freeform surfaces of most engineering materials selectively, with a relatively higher processing speed and higher accuracy, repeatability and reproducibility [11]. In addition, LST does

not involve the use of harmful chemicals and also can represent a relatively low cost option when compared with other unconventional machining processes.

LST was successfully employed by the automotive industry to treat cylinder liners of internal combustion engines and thus to improve fuel consumption and reduce engine wear [12]. It was also employed as a mean of reducing friction and wear between other types sliding surfaces such as PTFE/Kevlar fabric composites [13], polymers [14], and more [15]. More recently LST found applications in medical industry, specifically to modify surfaces of orthopedic implants. Shah et al. studied the effect of Nd: YAG laser modification of pure titanium implants on osseointegration and biomechanical anchorage. The modified implants exhibited 153% higher removal torque values in rabbit tibiae when compared to their untreated counterparts. Furthermore, when their fracture toughness was analyzed, fracture lines appeared within the bone for the laser modified implants whereas for the untreated titanium screws the implants failed at the bone/implant interface [16]. In another study, Briski et al. found that laser modified PEEK implants enhanced fusion in a sheep model and more abundant mineralized matrix and bony attachments were found on the treated implants than in the control group [17].

Laser Induced Periodic Surface Structures (LIPSS) are grating-like patterns that can be generated on almost any material when the laser power level is at or near the damage threshold of the workpiece. LIPSS generation is generally attributed to some form of interference between the incident laser beam and the surface-scattered electromagnetic waves [18]. Low spatial frequency (LSFL) LIPSS form on processed surfaces with a spatial period close to the laser wavelength and it is commonly under 1 μm for near infrared sources. This length scale is particularly interesting when dealing

with small living organisms, such as bone cells, and therefore LIPSS have a strong potential in the field of biomaterials modification. For example, LIPSS enhanced matrix mineralization and bone-like nodule formation as compared with polished Ti-6 Al-4V surfaces and thus they could potentially improve human mesenchymal stem cells differentiation into osteoblastic lineage [19]. Furthermore, it was shown that LIPSS with different periodicities greatly improved the proliferation of HEK-293 cell line on polystyrene surfaces; the improvement was more pronounced in the later stages of incubation [20]. In a previous study it was shown that a crossed LIPSS patterns enhanced Saos-2 osteoblast-like cell growth on polished cobalt-chromium-molybdenum (CoCrMo) alloy surfaces without compromising on initial cell adhesion, a characteristic of rougher surfaces [21].

It is evident from the result of many empirical studies that LST, LIPSS in particular, has a real potential as a technology for modifying implant surfaces and therefore it is essential to investigate and determine the process limitations. This is especially necessary when applying LST on freeform surfaces that are common in most implant designs. In particular, when the LST technology is deployed on complex 3D surfaces, there are substantial changes in the laser processing conditions when compared with the processing of planar surfaces. Therefore, the factors impacting the process performance on 3D surfaces should be considered as disturbances affecting the functional response of treated surfaces. Hence, the effects of such disturbances on added functionalities established in numerous empirical studies on planar surfaces should be investigated in order to establish the limitations of the LST technology when applied on 3D surfaces.

This paper reports investigation into the disturbances present in LST of 3D CoCrMo alloy surfaces and their effects on the functional response of such treated surfaces. In particular, the effects of the focal offset distance (FOD), beam incident angle (BIA) and the initial surface quality on the static water contact angle and Saos-2 osteoblast-like cells proliferation have been studied.

4.2 Material and methods

4.2.1 Material and surface analysis methods

CoCrMo disks, 13mm in diameter, were used in this research. The Wt% composition of the surgical grade CoCrMo casting alloy used in the experiments was as follows: 67.0% Co, 27.0% Cr and 5.0% Mo. The surface roughness of as-received disks was measured and the arithmetical mean height, S_a, and root mean square height, S_q, values were both around 45 µm. Some disks were polished down to a surface roughness of S_a 40 nm and S_q 60 nm. (measured using an Alicona focus variation microscope)

All disks were examined for periodicity data using a scanning electron microscopy, Zeiss EVO MA 10, with the following settings: WD=8.0mm and EHT=10.00kV. In addition, the topography of the laser processed samples was examined employing an atomic force microscopy (AFM), Dimension 3100 system with Bruker NP-10 non-conductive silicon nitride tips.

Considering the feature size of LIPSS, the Alicona's 10 nm vertical resolution would not be enough for accurate profile measurements.

4.2.2 Laser surface texturing

The CoCrMo disks were laser processed using an ultrashort near-infrared fiber laser with the following technical specification: 5W average power, 10µJ maximum pulse energy, 310fs pulse duration, 500 KHz maximum repetition rate, 1030 nm center wavelength and beam quality M^2 better than 1.2. The beam spot size at the focal plane was 40 µm.

Initially, the LIPSS pattern used in this study was optimized by varying the laser parameters on polished CoCrMo disks, employing the method proposed by Gnilitskyi et al. [22]. In particular, the LIPSS optimization process involved an analysis of SEM images and their regularity. Using the open-source software ImageJ with the OrientationJ plug-in and its Orientation Distribution module with Riesz Filters, the distribution angle values were calculated for the different SEM micrographs. All images used in the analysis had the same magnification (6,000x) in order to analyze sufficiently large areas. In addition, the spectrum was normalized with the highest value of the distribution shifted to the orientation value of 0°. Then, the value of half width at half maximum was obtained, defined as, the dispersion value of the LIPSS orientation angles (DLOA). The samples with lowest DLOA (2δθ) were highly-regular and therefore were selected to investigate how process disturbances could affect surface topographies and their respective functionalities in this research. The errors associated with this method were estimated by Gnilitskyi et al. at ~±1° and are due to the accuracy of the distribution and the residual fluctuations in the stabilized area. The considered laser parameters tested in a full factorial design and the optimized textured surface are shown in Figure 4.1. The pulse overlap was fixed in both x and y directions of scanning.

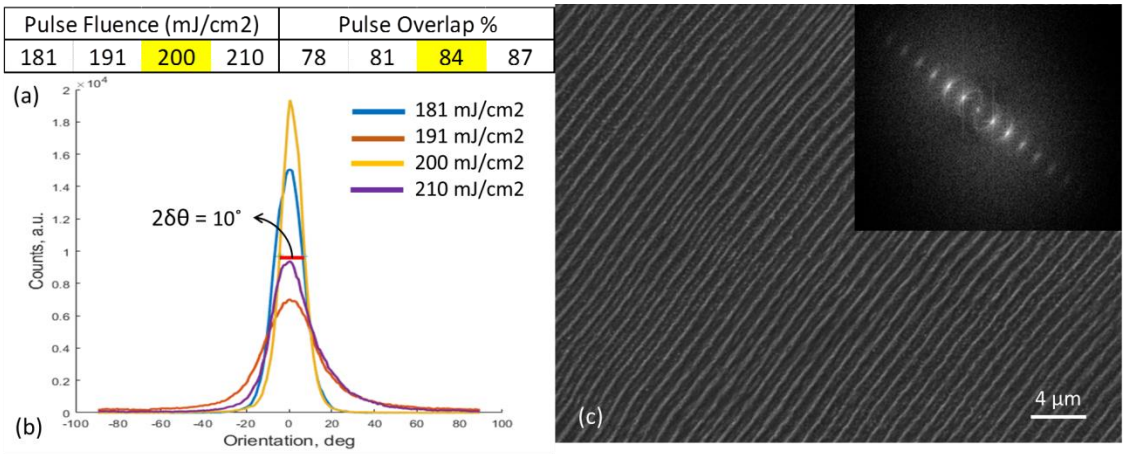

Figure 4.1 An overview of the conducted process optimisation: (a) the processing window considered in a full factorial design of experiments (b) distribution of orientation θ obtained from *ImageJ* for a fixed overlap of 84% (c) SEM micrograph, and corresponding Fourier transform of a CoCrMo surface processed with the optimized parameters

Note: Optimized parameters are highlighted in yellow

Then, the optimized laser parameters (Figure 4.1a) were used on all CoCrMo samples while process disturbances, i.e. FOD, BIA and material disturbance: initial surface quality, were introduced to investigate their effects on topography and functional response of LST surfaces. In particular, a set of experiments were conducted with the same laser processing settings while different levels of these three disturbances were applied as shown in Table 4.1.

Table 4.1 The parameters' domain used for LIPSS

Sample	Process-Material Disturbances		
	Surface Quality	**FOD (mm)**	**BIA (deg.)**
1	As-received	0	0
2	As-received	0.2	0
3	As-received	0.4	0
4	As-received	0.6	0
5	As-received	0.8	0
6	As-received	0	10
7	As-received	0	20
8	As-received	0	30
9	Polished	0	0
10	Polished	0.2	0
11	Polished	0.4	0
12	Polished	0.6	0
13	Polished	0.8	0
14	Polished	0	10
15	Polished	0	20
16	Polished	0	30

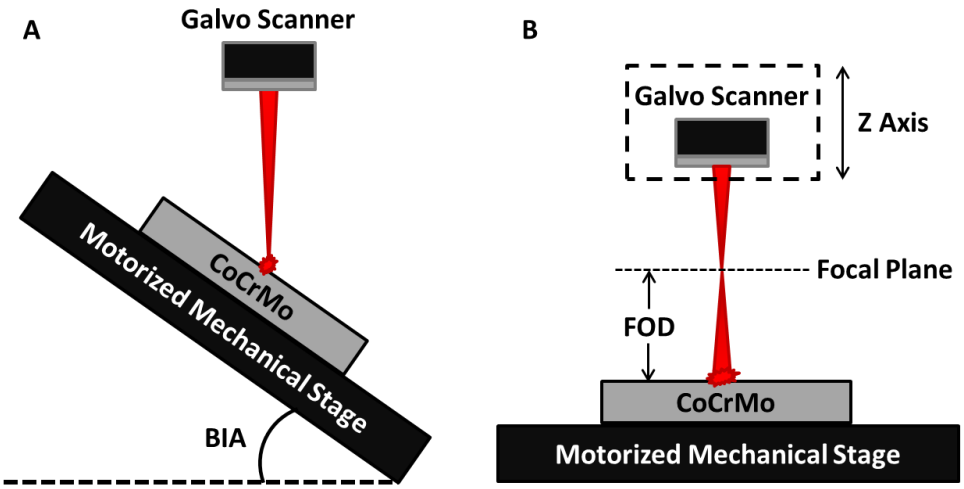

Figure 4.2 Schematic diagrams of laser processing at different A) BIA and B) FOD

4.2.3 Functional analysis of LST surfaces

Prior to functional testing, the samples were rigorously cleaned as follows: two 15 min ultrasonic baths, first, in pure acetone, and then, in 70 vol% ethanol aqueous solution. The disks were rinsed with distilled pure water in-between baths and finally dried with argon gas and stored in sterile petri dishes.

The wetting properties of the LST surfaces were analyzed directly after cleaning. Especially, static contact angle (CA) measurement was performed employing the sessile drop technique. An Attension Theta optical tensiometer with 6µL drops of purified Milli-Q water was used to conduct these measurements. The drop volume was selected in such way that the gravity forces to be not higher than the capillary one, hence to minimize any additional kinetic energy. In this way the values represent the true solid/liquid interactions.

Saos-2 osteoblast-like cells proliferation on LST CoCrMo disks was analyzed, too. In particular, the specimens were then placed in 24-well plates (Thermo Scientific™ Nunc™ Cell-Culture Treated Multidishes) and approximately $1x10^4$ Saos-2 osteoblast-like cells were seeded on each sample in McCoy's 5A medium supplemented with 10% fetal bovine serum (FBS), 100U/mL of Penicillin and 100μg/mL of Streptomycin. The well plates were placed in a humidified incubator at 37˚C in an atmosphere of 5% CO_2 and the culture medium was changed every 2 days.

Saos-2 cells metabolic activity was evaluated via a MTT assay [23], reflecting the cells' proliferation on the different CoCrMo specimens. MTT was prepared in phosphate buffered saline (PBS, pH 7.4) with a concentration of 5mg/mL. 60μL of the MTT solution was added to each well and the plates were incubated at 37˚C in an atmosphere of 5% CO_2 for 4 hours at the selected time interval, 4 days after seeding. The medium was then removed and 0.6mL of DMSO was added to each well to dissolve the formazan. The well plates were placed on a shaking platform for 5 minutes and then the optical density was measured at 570 nm using a spectrophotometer.

All functional data was expressed as mean and standard deviation, n=4 for CA and MTT measurements. Statistical analysis was performed using Minitab 17 Statistical Software. A Pearson correlation valuation was conducted to examine the relationship between wettability and cell proliferation on the laser treated disks.

4.3 Results

4.3.1 Effects on surface topography

LST was performed on the CoCrMo disks employing the process settings and disturbances provided in Table 4.1. First, the effects of initial surface roughness on

resulting surface topography were analyzed. In particular, LST produced different results on the as-received and polished surfaces as depicted in Figure 4.3. The surface defects on as-received disks (see Figure 4.3c) led to interruptions in the LIPSS patterns and changes in the ripples' orientation. Moreover, small areas were left untextured, too. At the same time, on polished disks (see Figure 4.3d), the LIPSS were highly regular, parallel and uniform while their orientation was perpendicular to the laser polarization vector and covered the surface of the disk completely.

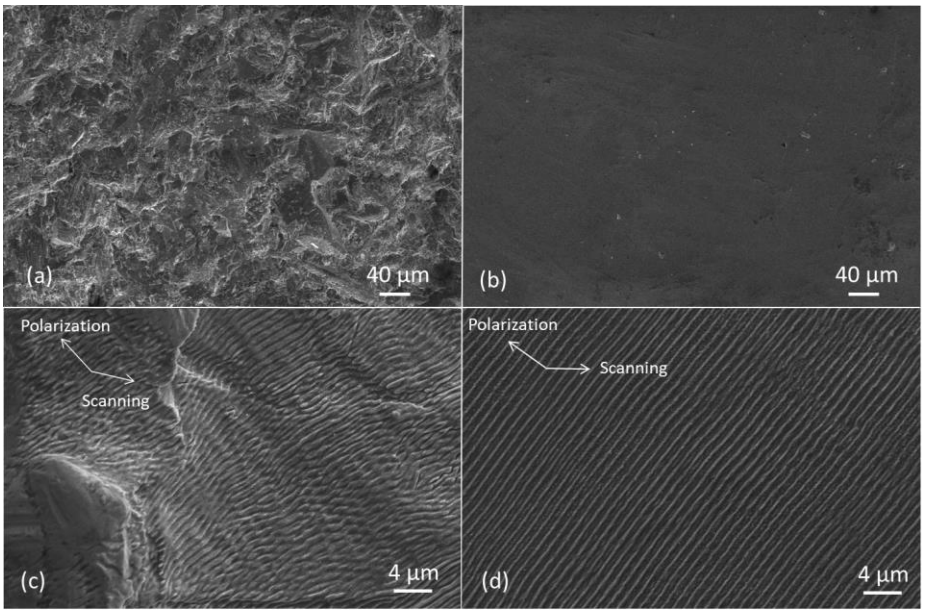

Figure 4.3 Representative SEM micrographs of (a) as-received and (b) polished (c) laser processed as-received (d) laser processed polished CoCrMo surfaces

Note: LST was conducted in-control using optimized parameters and without any process disturbances

Second, the effects of the beam incident angle on periodicity of produced LIPSS on polished CoCrMo disks were investigated experimentally. In particular, the periodicity of produced LIPSS was assessed by using the Fourier transforms of the SEM images as shown in Figure 4.4. The periodicity increased with the increase of the BIA and was roughly 980, 1140, 1400 and 1770 nm, respectively for incidence angles of 0, 10, 20 and 30˚. Furthermore, additional intermediary ripples were formed at 30˚ their periodicity was 650 nm. No such ripples were observed at processing angles less than 30˚.

The theoretical LIPSS periodicity was calculated, too. It depends on beam incidence angle and can be expressed as:

$$\Lambda = \lambda/\sqrt{(k_0/k)^2 \pm sin^2\theta} \qquad \text{(Equation 1)}$$

where: λ is the laser wavelength; k_0 - the surface electromagnetic wave propagation constant (function of the material dielectric constants); $k = 2\pi/\lambda$; and θ - the laser beam incidence angle [24]. The p- and p+ variants in Figure 4.4 are a result of the +/- sign in Equation 1. The theoretical periodicity was calculated based on Equation 1 and then normalized to the measured periodicity at 0˚ as the values were slightly higher. The empirical and analytical results are compared in Figure 4.4. The deviation between the theoretical and experimental values was small then 5% and this could be attributed to some processing effects together with some measurement uncertainty (SEM accuracy and image resolution) and the alloy's real dielectric constants. Overall, there was a strong agreement between the theoretical and experimental trends as depicted in Figure 4.4. The amplitude of the ripples (the depth of valleys) stayed unchanged when

BIA was set at 10 and 20˚, however at a 30˚, the intermediary ripples had an amplitude of roughly 50 nm.

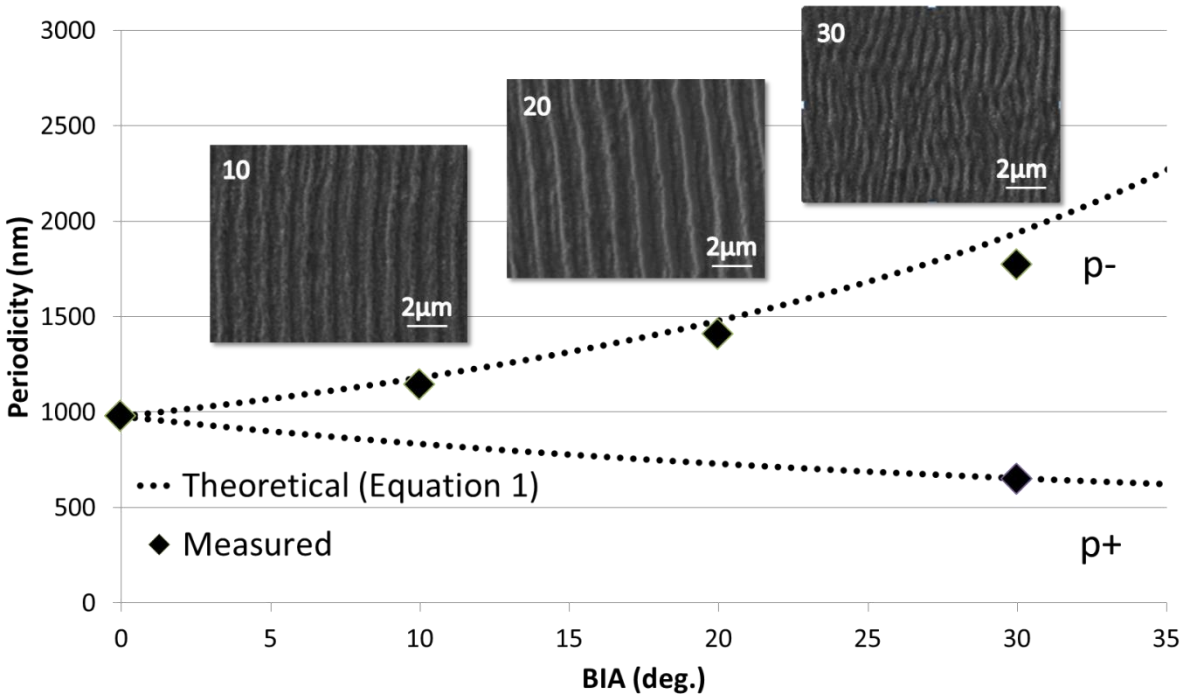

Figure 4.4 Empirical and analytical LIPSS periodicity at different BIA values on CoCrMo
Note: the dash line represents the theoretical values while the diamonds the empirical values obtained from the Fourier transforms of the SEM images (n=4).

Last, the effects of the FOD on resulting LIPSS were analyzed. The profiles of the LIPSS were analyzed via AFM and the data is summarized in Figure 4.5 and Table 4.2. The average LIPSS amplitude decreased from 115 nm when in focus down to 35 nm at a defocusing distance of 0.8mm (see Figure 4.5). The periodicity of the produced ripples stayed unchanged when FOD was varied.

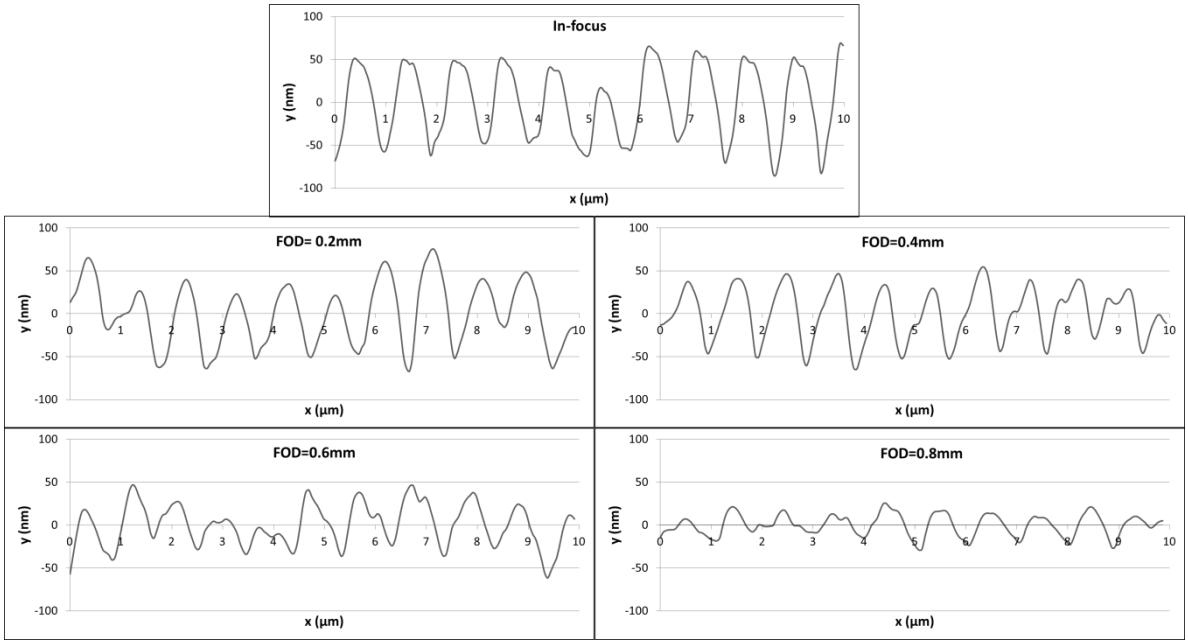

Figure 4.5 Profile of polished surfaces with LIPSS at different FOD

Table 4.2 Summary of the effects of process disturbances on resulting topography (n=4)

	Sample	Average Depth (±10nm)	Average periodicity (±15nm)	Representative Surface Profile
FOD	9	115	980	
	10	105	980	
	11	90	980	
	12	60	980	
	13	35	980	
BIA	14	115	1140	
	15	115	1400	
	16	110 & 50	1770 & 650	

4.3.2 Effects on surface functionality

4.3.2.1 Surface wettability

The LIPSS treatment decreased the wettability both on as-received and polished CoCrMo disks. In particular, the LST process increased the CA values from 57.9˚ to 63.6˚ (9.8%) and from 46.0˚ to 54.7˚ (19%) on as-received and polished surfaces, respectively, when there was no any other processing disturbances present.

The CA values increased further with the increase of the BIA as shown in Figure 4.6. The trend appears to be valid for both As-Received and polished surfaces. The CA increased from 63.6˚ to 76.1˚ (20%) and from 54.7˚ to 68.5˚ (25%) with the increase of the angle of incidence to 30˚ on as-received and polished disks, respectively.

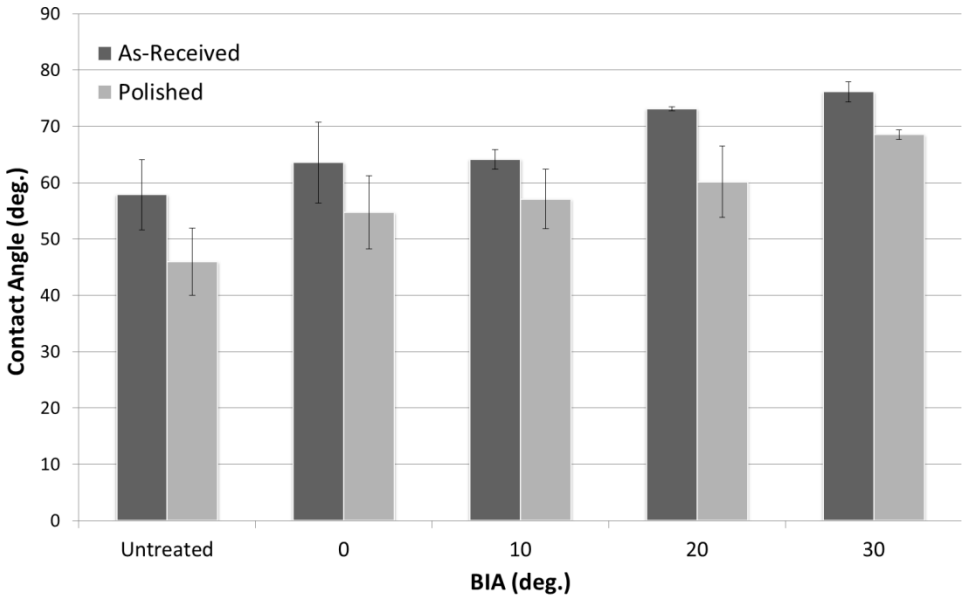

Figure 4.6 The beam incident angle effects (deg.) on CoCrMo disks' wettability (n=4)

Finally, the FOD effects on surface wettability were analyzed. The CA values increased initially with the increase of the beam offset to reach a plateau at 0.4mm offset and then gradually decreased as shown in Figure 4.7. This tendency was observed both on as-received and polished disks. In particular, 17% and 6% CA increase were observed initially on both disks respectively, and then the CA values dropped significantly on as-received disks, i.e. from 74.2˚ to 55.6˚, and only marginally from 58.1˚ to 55.3˚ on polished samples when FOD reached 0.8mm.

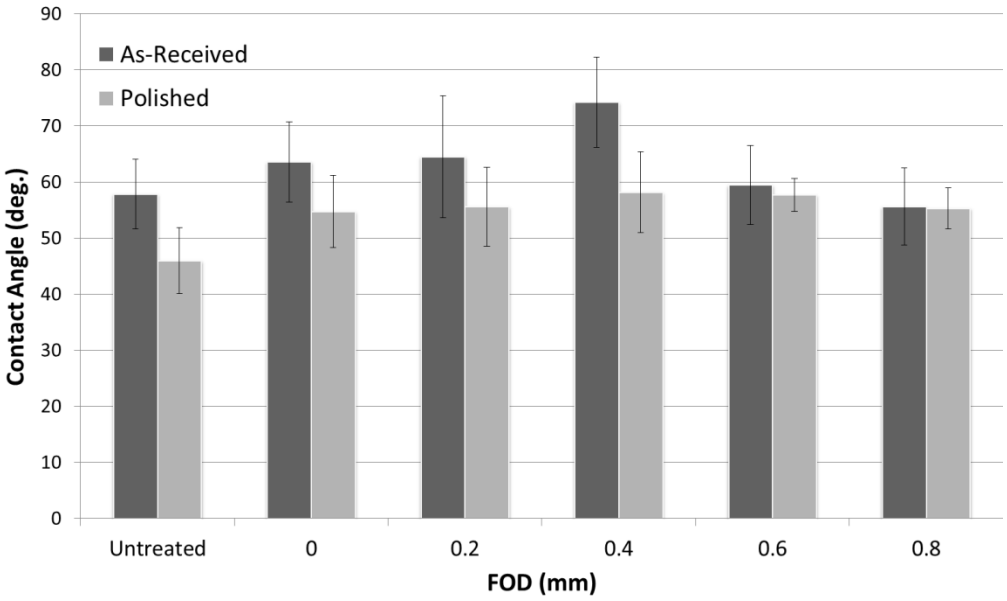

Figure 4.7 The beam defocusing distance (mm) effects on CoCrMo disks' wettability (n=4)

4.3.2.2 Saos-2 cell proliferation

Overall, LIPSS enhanced the proliferation of the Saos-2 osteoblast-like cells on CoCrMo alloy disks, regardless of their initial surface condition. The highest improvement in cell viability observed was 18.2% and 27.7% for the As-Received and polished surfaces respectively, 4 days after seeding the cells compared with the untreated surfaces.

Generally, higher cell viability was observed on rougher As-Received surfaces 4 days after seeding regardless of the laser treatment.

The Saos-2 cell viability decreased with the increase of the laser incidence angle (Figure 4.8). This is the case for both As-Received and polished surfaces. The optical density decreased from 0.155 to 0.111 (27.7%) and from 0.149 to 0.109 (26.8%) for the As-Received and polished surfaces with the increase of the incidence angle to 30˚, respectively.

A loss of the added cell proliferation improvement via LST is apparent when the BIA is increased past 25˚, indeed, higher optical density values were obtained on untreated surfaces compared to those that were processed with 30˚ BIA.

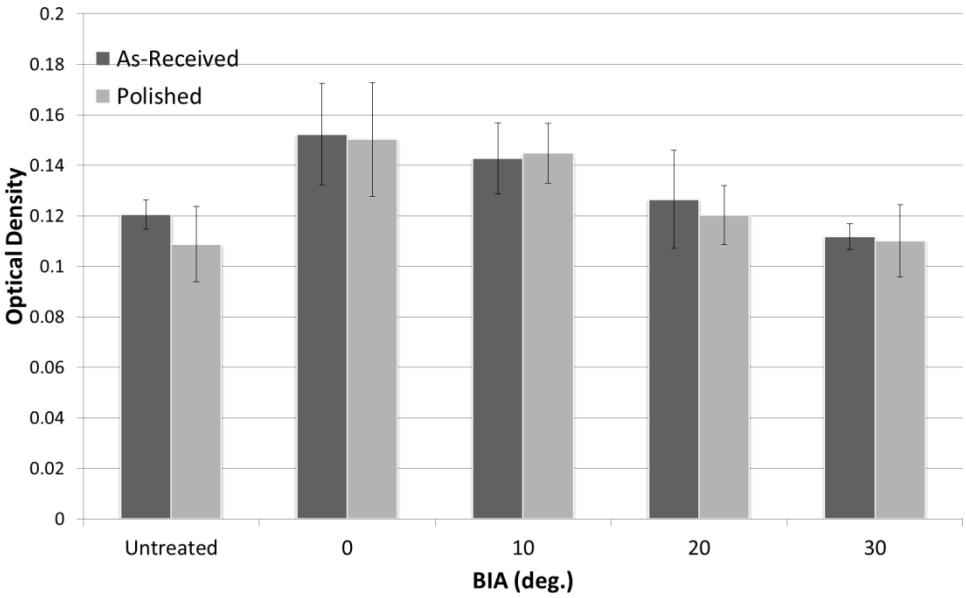

Figure 4.8 The beam incident angle (deg.) influence on proliferation of Saos-2 cells on textured CoCrMo disks 4 days after seeding (n=4)

A similar trend in regards to the cell viability was observed initially with the FOD increase and the lowest values were obtained at FOD of 0.4mm. Then, there was a gradual increase with any further focus offset as shown in Figure 4.9 and this trend was observed on both As-Received and polished surfaces. In particular, the optical density decreased initially from 0.155 to 0.126 (18.5%) and 0.149 to 0.123 (17%) when FOD reached 0.4 mm before it started to increase to 0.141 and 0.137 at 0.8 mm defocusing distance on As-Received and polished surfaces, respectively. The experiments were repeated 4 times and the trends were consistent across the repetitions with some differences in the underlying values.

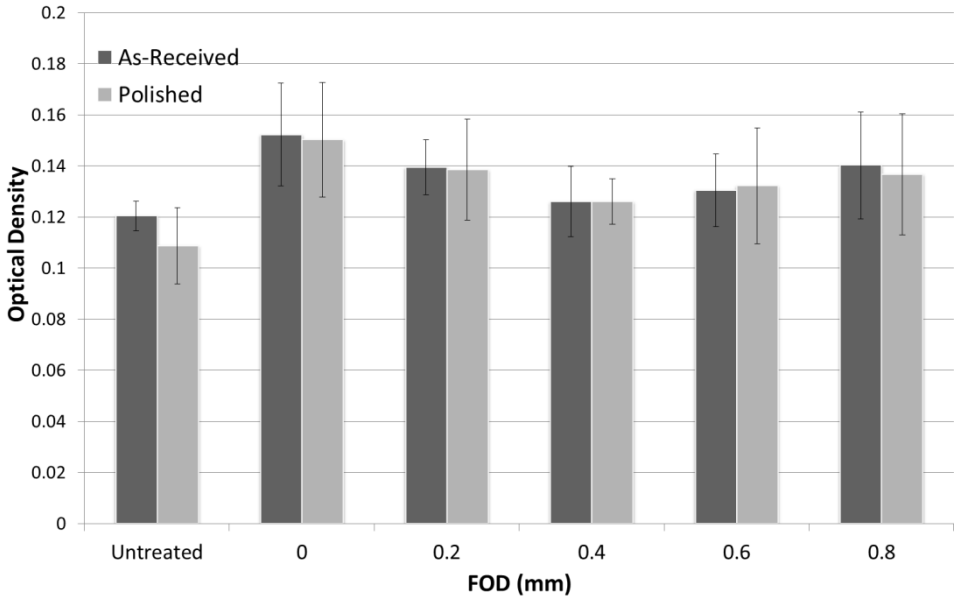

Figure 4.9 The beam defocusing distance (mm) influence on proliferation of Saos-2 cells on textured CoCrMo disks 4 days after seeding (n=4)

Therefore, looking at the CA and proliferation data, there is an inverse correlation between CA and the proliferation of Saos-2 cells on the laser-treated CoCrMo alloy disks, regardless of their initial surface quality. The same trend was observed when cell viability measurements were taken 2 days after seeding (data not shown), however the biological improvement was more pronounced after 4 days. The Pearson correlation results for the laser processed samples are shown in Table 4.3. It is worth noting that the effects of BIA on the functional response of the surface are more pronounced than those of FOD; the statistical significance of the results is greater when the BIA is changed and less so when the FOD is changed.

Table 4.3 Pearson Correlation

Laser Processing Condition	Pearson Correlation Coefficient	P-Value
As-Received/Incident Angle	-0.974	0.026
As-Received/Off-Focus	-0.411	0.492
Polished/Incident Angle	-0.973	0.027
Polished/Off-Focus	-0.896	0.04

4.4 Discussion

The conducted empirical study has shown clearly that changes in the LST conditions, i.e. the presence of disturbances common in laser processing of 3D surfaces, alter the functionality of laser-processed surfaces. Therefore, the effects of such process disturbances, i.e. initial surface roughness, FOD and BIA, should be considered carefully when LST ‘recipes’ developed and tested on planar substrates are applied on

freeform surfaces, e.g. when processing implants. The ranges within which the desired surface functional response is still within some pre-defined limits in the presence of these process disturbances should be determined. In this way, it will be possible to define/design LST strategies that allow the surface functionality to be maintained within acceptable limits dictated by any specific application.

When the process is in control (no presence of LST disturbances), LST leads to a decrease of the CoCrMo disks' wettability. This indicates that despite the samples remaining relatively hydrophilic (CA<90˚), they exhibited a Cassie-Baxter (CB) state of wetting, i.e. where air entrapped in the surface roughness contributed to the wettability decrease. According to Giacomello et al., the CB state at the nanoscale can be stable in the case of moderate hydrophilic surfaces [25]. The experimental results in this research are in line with Giacomello's analysis, as the introduction of sub-micron surface topography did not increase the wettability of the initially hydrophilic surface. Furthermore the introduction of LIPSS was shown to increase the CA on AISI 316L and Ti–6Al–V surfaces further reaffirming the CB theory [26].

The laser processing treatment improved the biological response of the CoCrMo alloy disks, regardless of their initial surface quality, as was expected based on literature and previous work [19-21].

The effects of each of the three LST disturbances, i.e. the initial surface quality, BIA and FOD on the static water contact angle and Saos-2 osteoblast-like cells proliferation are discussed separately in the follow up sub-sections.

4.4.1 Effects of initial surface quality on functional response

The irregularity of the rough surface influenced the formation, morphology and orientation of the LIPSS on the as-received CoCrMo alloy disks. In particular, defects such as small holes, grains and scratches disrupted the regular orientation of ripples that are normally perpendicular to the polarization vector. Such defects may result in surface strain which overpowers the laser electric field governing the formation direction of the LST generated sub-micron structures. Similar findings were observed on calcium fluoride and poly-carbonate films [27, 28]. Moreover, morphological differences related to process disturbances such as off-focus processing and BIA variations were observed also on in-control processed as-received samples due to topography variations that led to the different orientations of normal vectors at each processed spot on the surface.

The rougher CoCrMo surfaces exhibited higher CA that was in line with the CB state analysis as they contained more air pockets compared to the polished disks.

The higher Saos-2 cells viability observed on the as-received disks was in agreement in previous studies; rougher surfaces offered better initial mechanical anchorage [21].

4.4.2 Effects of beam incident angle on functional response

When BIA deviations were introduced, the CA values increased with the BIA increase. This was attributed to the resulting increase of LIPSS periodicity as no other significant morphological differences were observed between samples processed with and without any BIA changes. Such a dependence was not reported by other researchers when investigated the BIA effects on polymer substrates, in particular after LIPSS processing of polystyrene or polyethyleneterephthalate samples [20, 29]. The

wettability decrease of LST surfaces can be explained with the CB state. In particular, the higher periodicity led to relatively wider air pockets between the ripples and thus to the bigger air entrapment that led to a higher CA.

At the same time, a decrease in Saos-2 cell proliferation was observed on samples processed with higher BIA. This could be attributed again to the bigger ripples' periodicity. Knowing that cells anchor to the top of the sub-micron features [21, 30, 31], the longer periodicity implies that the seeded cells have to span larger distances in order to find anchoring points, thus this leads to less focal adhesion overall [31]. Other researchers observed the same interdependence between the cell proliferation and periodicity [20].

4.4.3 Effects of focal offset distance on functional response

When off-focus processing is performed or FOD is introduced in general, the effective spot size increases and hence laser fluence is reduced. Thus, any FOD variations shift the processing conditions away from the optimum fluence levels for LIPSS treatments of CoCrMo substrates and as a result the LIPSS depth gradually decreases until eventually no ripples are generated anymore. The diameter of a Gaussian beam at a distance z from the beam waist is given by [32]:

$$D(z) = D_0\sqrt{1 + (\frac{z}{z_R})^2} \qquad \text{(Equation 2)}$$

Where: D_0 is the beam diameter at the waist and z_R is the Rayleigh length. Thus for FOD of 0.2, 0.4, 0.6 and 0.8mm, the respective beam diameters are 40.53, 42.09, 44.58 and 47.83 μm while the corresponding laser pulse fluence values are: 195.3, 181.1, 161.4 and 140.3mJ/cm^2. Thus, the relationship between the laser fluence and

the depth of the sub-micron ripples appears to be linear on the polished CoCrMo disks within the investigated parameters' range (Table 4.2).

As a result of the FOD increase in this research, the corresponding fluence and LIPSS depth decreased and this had a detrimental effect on functional response of textured surfaces. In particular, the wettability of the CoCrMo surfaces decreased with the FOD increase. The FOD variations led to a CA increase initially (see Figure 4.7) when compared with the samples processed in-focus. Similar results were reported by Kietzig et al. when processing pure Cobalt, i.e. the highest CA value was achieved at a fluence level lower than the highest one tested [33]. In addition, an off focus processing of copper and nickel surfaces to produce LIPSS was reported, too, and again this led to higher CA values and a trend similar to that depicted in Figure 4.6 was discussed [34]. This suggests the existence of a specific sub-micron ripple depth, around 89 nm in this case, where the apparent CA is highest. The CA values eventually decreased with the gradual loss of pattern due to the lower laser pulse fluence levels. The processing with a varying FOD had a detrimental effect on proliferation of Saos-2 cells, too. Especially, the proliferation decreased and reached the lowest values at FOD of 0.4mm and then slightly increased while remaining under the levels achieved without the focal offset. The FOD effects of the laser focal plane position were less pronounced than those of BIA on the proliferation of Saos-2 cells. Lamers et al. postulated the existence of a threshold LIPSS depth under which rat bone marrow cells were unable to respond to surface patterns on polystyrene [31]. This seems to be the case with samples processed with varying FOD; the gradual LIPSS depth decrease and ultimately the LST loss led to a gradual loss of the added surface functionalities, i.e. both surface wetting and Saos-2 proliferation.

4.4.4 Interdependences between wettability and Saos-2 cells proliferation

Looking at the impact of the two LST disturbances investigated in this research, i.e. the BIA and FOD deviations, on the wettability and Saos-2 cell proliferation data, it is clear that there is a correlation between them. In particular, a decrease of surface wettability, i.e. a CA increase, leads to a decrease of the Saos-2 cell proliferation. This is also confirmed by the Pearson correlation results reported in Table 4.3 where the average Pearson coefficient was close to -1. The correlation results did not show a strong agreement in the case of the As-received/Off-focus LST condition and this could be due to the high variations in height observed on the As-received samples, therefore the position of the focal plane relative to the surface is not always constant. To better visualize these trends, the surface functional responses were plotted against the different process disturbances in Figure 4.10. Therefore, any wettability changes can be used to explain and also to indicate for potential changes in the Saos-2 cell proliferation due to the effects on cells number/proliferation/metabolic activity on LST surfaces only and cannot be compared with non-structured surfaces (Figures 4.6 to 4.10). The mechanisms governing cell attachment and growth are different for structured surfaces. It is worth noting that any LST treatments with ultrashort lasers, e.g. a femtosecond laser source in this research, are carried out with a very low fluence (200 mJ/cm^2). In addition, the laser-material interaction time is extremely small (310fs pulse duration) and therefore the temperature gradient can be considered negligible in the processed area. Thus, the surface chemistry is usually not affected and can be considered unchanged after laser processing [19]. Therefore, any changes in wettability and cell proliferation can only be attributed to changes in the regular sub-micron topography. For example, the surface wettability could be used to explain the

dip in Saos-2 cell proliferation at a beam defocusing distance of 0.4mm and the subsequent increase at 0.8mm. However, it should be stressed that the correlation between surface wettability and cell proliferation stands only when the LST surfaces are chemically and topographically comparable. A separate chemical analysis is not presented as it is not in the scope of this research, however it can be assumed that no chemical differences exist between the LIPSS treated surfaces [19]. This correlation could be used to judge the biological performance of LIPSS covered surfaces and determine the limits when transferring the added functionalities onto freeform implant surfaces and thus develop an adequate laser patching strategy.

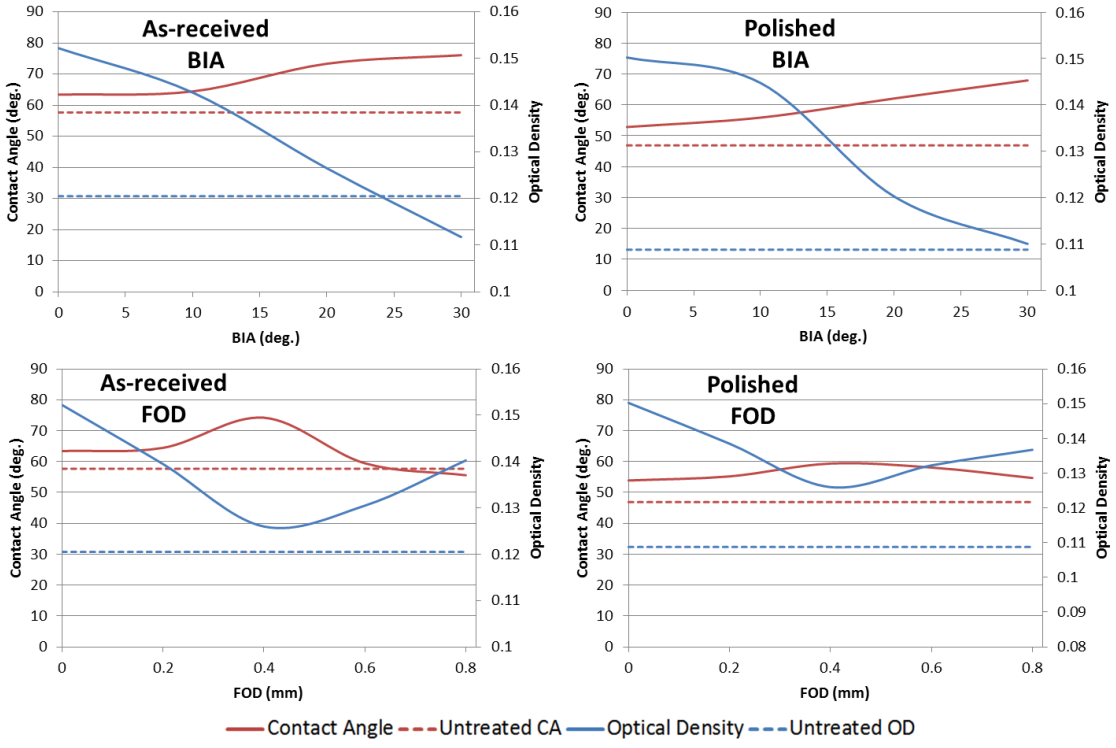

Figure 4.10 Interdependences between wettability and Saos-2 cells proliferation on laser treated CoCrMo disks

4.5 Conclusion

The effects of LST disturbances on functional response of LIPSS treated CoCrMo disks with a NIR fs laser were investigated in this research. In particular, the FOD and BIA were varied to simulate the processing of a 3D part. The effects of these process disturbances on wettability and Saos-2 cell proliferation were analyzed. The following conclusions can be made based on the obtained results:

1. In general, the LIPSS treatments enhanced the Saos-2 cells proliferation on the CoCrMo disks while their wettability decreased.
2. Irrespective of initial surface roughness there were substantial improvements in Saos-2 cells proliferation.
3. The biological response of laser-processed biomaterials is more sensitive to BIA changes compared with the effects of FOD variations, i.e. Saos-2 cells were more affected by changes in the periodicity of the sub-micron ripples rather than their depth
4. The biological performance of biomaterials can be correlated to their wettability when the surfaces are chemically and topographically comparable.

Acknowledgments

The research was supported by two European Commission H2020 projects, i.e. the ITN programme “European ESRs Network on Short Pulsed Laser Micro/Nanostructuring of Surfaces for Improved Functional Applications” (Laser4Fun) and the FoF programme “High-Impact Injection Moulding Platform for mass-production of 3D and/or large micro-structured surfaces with Antimicrobial, Self-cleaning, Anti-

scratch, Anti-squeak and Aesthetic functionalities” (HIMALAIA). In addition, the work was carried out within the framework of the UKIERI DST programme “Surface functionalisation for food, packaging, and healthcare applications”.

References

1. Liu, T.Y. and C.J. Kim, Turning a surface superrepellent even to completely wetting liquids. Science, 2014. 346(6213): p. 1096-1100.
2. Ma, Q.L., L.Z. Zhao, R.R. Liu, B.Q. Jin, W. Song, Y. Wang, Y.S. Zhang, L.H. Chen, and Y.M. Zhang, Improved implant osseointegration of a nanostructured titanium surface via mediation of macrophage polarization. Biomaterials, 2014. 35(37): p. 9853-9867.
3. Jwad, T., S.A. Deng, H. Butt, and S. DimovSchool, Laser induced single spot oxidation of titanium. Applied Surface Science, 2016. 387: p. 617-624.
4. Cheng, L., W. Chen, M. Kunz, K. Persson, N. Tamura, G. Chen, and M. Doeff, Effect of surface microstructure on electrochemical performance of garnet solid electrolytes. ACS Appl Mater Interfaces, 2015. 7(3): p. 2073-81.
5. Garcia-Giron, A., J.M. Romano, Y. Liang, B. Dashtbozorg, H. Dong, P. Penchev, and S.S. Dimov, Combined surface hardening and laser patterning approach for functionalising stainless steel surfaces. Applied Surface Science, 2018. 439: p. 516-524.
6. Gholami, M., M. Hoseinpoor, and M.H. Moayed, A statistical study on the effect of annealing temperature on pitting corrosion resistance of 2205 duplex stainless steel. Corrosion Science, 2015. 94: p. 156-164.
7. Shi, Z.Y., Z.Q. Liu, H. Song, and X.Z. Zhang, Prediction of contact angle for hydrophobic surface fabricated with micro-machining based on minimum Gibbs free energy. Applied Surface Science, 2016. 364: p. 597-603.

8. Kumar, C.S. and S.K. Patel, Effect of WEDM surface texturing on Al2O3/TiCN composite ceramic tools in dry cutting of hardened steel. Ceramics International, 2018. 44(2): p. 2510-2523.
9. Arisoy, F.D., K.W. Kolewe, B. Homyak, I.S. Kurtz, J.D. Schiffman, and J.J. Watkins, Bioinspired Photocatalytic Shark-Skin Surfaces with Antibacterial and Antifouling Activity via Nanoimprint Lithography. Acs Applied Materials & Interfaces, 2018. 10(23): p. 20055-20063.
10. Bang, S.M., H.J. Moon, Y.D. Kwon, J.Y. Yoo, A. Pae, and I.K. Kwon, Osteoblastic and osteoclastic differentiation on SLA and hydrophilic modified SLA titanium surfaces. Clinical Oral Implants Research, 2014. 25(7): p. 831-837.
11. Bhaduri, D., P. Penchev, S. Dimov, and S.L. Soo, An investigation of accuracy, repeatability and reproducibility of laser micromachining systems. Measurement, 2016. 88: p. 248-261.
12. Etsion, I., State of the art in laser surface texturing. Journal of tribology, 2005. 127(1): p. 248-253.
13. Qi, X.W., H. Wang, Y. Dong, B.L. Fan, W.L. Zhang, Y. Zhang, J. Ma, and Y.F. Zhou, Experimental analysis of the effects of laser surface texturing on tribological properties of PTFE/Kevlar fabric composite weave structures. Tribology International, 2019. 135: p. 104-111.
14. Dufils, J., F. Faverjon, C. Heau, C. Donnet, S. Benayoun, and S. Valette, Combination of laser surface texturing and DLC coating on PEEK for enhanced tribological properties. Surface & Coatings Technology, 2017. 329: p. 29-41.

15. Bonse, J., S.V. Kirner, M. Griepentrog, D. Spaltmann, and J. Kruger, Femtosecond Laser Texturing of Surfaces for Tribological Applications. Materials, 2018. 11(5).
16. Shah, F.A., M.L. Johansson, O. Omar, H. Simonsson, A. Palmquist, and P. Thomsen, Laser-Modified Surface Enhances Osseointegration and Biomechanical Anchorage of Commercially Pure Titanium Implants for Bone-Anchored Hearing Systems. Plos One, 2016. 11(6).
17. Briski, D.C., B.W. Cook, J.M. Zavatsky, and T. Ganey, Laser Modified PEEK Implants as an Adjunct to Interbody Fusion: A Sheep Model. The Spine Journal, 2015. 15(10): p. S187.
18. Sipe, J.E., J.F. Young, J.S. Preston, and H.M. Vandriel, Laser-Induced Periodic Surface-Structure .1. Theory. Physical Review B, 1983. 27(2): p. 1141-1154.
19. Cunha, A., O.F. Zouani, L. Plawinski, A.M.B. do Rego, A. Almeida, R. Vilar, and M.C. Durrieu, Human mesenchymal stem cell behavior on femtosecond laser-textured Ti-6Al-4V surfaces. Nanomedicine, 2015. 10(5): p. 725-739.
20. Rebollar, E., I. Frischauf, M. Olbrich, T. Peterbauer, S. Hering, J. Preiner, P. Hinterdorfer, C. Romanin, and J. Heitz, Proliferation of aligned mammalian cells on laser-nanostructured polystyrene. Biomaterials, 2008. 29(12): p. 1796-1806.
21. Batal, A., R. Sammons, and S. Dimov, Response of Saos-2 osteoblast-like cells to laser surface texturing, sandblasting and hydroxyapatite coating on CoCrMo alloy surfaces. Materials Science and Engineering: C, 2019. 98: p. 1005-1013.
22. Gnilitskyi, I., T.J.Y. Derrien, Y. Levy, N.M. Bulgakova, T. Mocek, and L. Orazi, High-speed manufacturing of highly regular femtosecond laser-induced periodic surface structures: physical origin of regularity. Scientific Reports, 2017. 7.

23. Mosmann, T., Rapid Colorimetric Assay for Cellular Growth and Survival - Application to Proliferation and Cyto-Toxicity Assays. Journal of Immunological Methods, 1983. 65(1-2): p. 55-63.

24. Prokhorov, A.M., A.S. Svakhin, V.A. Sychugov, A.V. Tishchenko, and A.A. Khakimov, Excitation and Resonant Transformation of a Surface Electromagnetic Wave during Irradiation of a Solid by High-Power Laser Radiation. Kvantovaya Elektronika, 1983. 10(5): p. 906-912.

25. Giacomello, A., S. Meloni, M. Chinappi, and C.M. Casciola, Cassie-Baxter and Wenzel States on a Nanostructured Surface: Phase Diagram, Metastabilities, and Transition Mechanism by Atomistic Free Energy Calculations. Langmuir, 2012. 28(29): p. 10764-10772.

26. Bizi-Bandoki, P., S. Benayoun, S. Valette, B. Beaugiraud, and E. Audouard, Modifications of roughness and wettability properties of metals induced by femtosecond laser treatment. Applied Surface Science, 2011. 257(12): p. 5213-5218.

27. Csete, M., O. Marti, and Z. Bor, Laser-induced periodic surface structures on different poly-carbonate films. Applied Physics a-Materials Science & Processing, 2001. 73(4): p. 521-526.

28. Reif, J., O. Varlamova, and F. Costache, Femtosecond laser induced nanostructure formation: self-organization control parameters. Applied Physics a-Materials Science & Processing, 2008. 92(4): p. 1019-1024.

29. Krajcar, R., J. Siegel, P. Slepicka, P. Fitl, and V. Svorcik, Silver nanowires prepared on PET structured by laser irradiation. Materials Letters, 2014. 117: p. 184-187.

30. Matsugaki, A., G. Aramoto, T. Ninomiya, H. Sawada, S. Hata, and T. Nakano, Abnormal arrangement of a collagen/apatite extracellular matrix orthogonal to osteoblast alignment is constructed by a nanoscale periodic surface structure. Biomaterials, 2015. 37: p. 134-143.

31. Lamers, E., R. van Horssen, J. te Riet, F.C.M.J.M. van Delft, R. Luttge, X.F. Walboomers, and J.A. Jansen, The Influence of Nanoscale Topographical Cues on Initial Osteoblast Morphology and Migration. European Cells & Materials, 2010. 20: p. 329-343.

32. Meschede, D., Optics, Light, and Lasers: The Practical Approach to Modern Aspects of Photonics and Laser Physics. Optics, Light, and Lasers: The Practical Approach to Modern Aspects of Photonics and Laser Physics, 2017: p. 1-528.

33. Kietzig, A.M., M.N. Mirvakili, S. Kamal, P. Englezos, and S.G. Hatzikiriakos, Laser-Patterned Super-Hydrophobic Pure Metallic Substrates: Cassie to Wenzel Wetting Transitions. Journal of Adhesion Science and Technology, 2011. 25(20): p. 2789-2809.

34. Zhang, Y.C., G.S. Zou, L. Liu, Y. Zhao, Q. Liang, A.P. Wu, and Y.N. Zhou, Time-dependent wettability of nano-patterned surfaces fabricated by femtosecond laser with high efficiency. Applied Surface Science, 2016. 389: p. 554-559.

CHAPTER 5: LASER PROCESSING OF FREEFORM SURFACES: A NEW APPROACH BASED ON AN EFFICIENT WORKPIECE PARTITIONING STRATEGY

A. Batal[1✉], A. Michalek[1], P. Penchev[1], A. Kupisiewicz[2], S. Dimov[1]

[1] Department of Mechanical Engineering, University of Birmingham, Edgbaston, Birmingham, B15 2TT, UK

[2]Lasea SA, Liege Science Park, 4031 ANGLEUR, Belgium

This research was published as a full-length article in the *International Journal of Machine Tools and Manufacture* (2020):

Batal, A., Michalek, A., Penchev, P., Kupisiewicz, A., & Dimov, S. (2020). Laser processing of freeform surfaces: A new approach based on an efficient workpiece partitioning strategy. International Journal of Machine Tools and Manufacture, 156, 103593.

Keywords: 3D laser processing; freeform surface; surface partitioning; laser polishing; laser texturing; additive manufacturing

Authors' Contributions:

A. Batal

Main author, conducted the laser experiments characterisation and analysis.

A. Michalek

Assisted with MATLAB coding

P. Penchev

Assisted with laser machining setup and supervision

A. Kupisiewicz

Supervision and proofreading

S. Dimov

Supervision and proofreading

Abstract

A novel method for laser processing freeform surfaces is proposed and demonstrated in this article. The method employs empirical data on the 3D limitations of a given laser process, namely the negative effects of focal offset and angle of incidence on the process performance, to partition a freeform surface into triangular laser processing fields. In this way, processing efficiency can be maximized by minimizing part repositioning while fully utilizing the capabilities of high dynamics galvo scanners. In this proof of concept, the surface of 3D printed Ti-6Al-4V spherical shells was improved by more than 90% (S_a) and subsequently textured, using the proposed method. Conclusions were made about the advantages of this new approach for processing freeform surfaces consistently and efficiently.

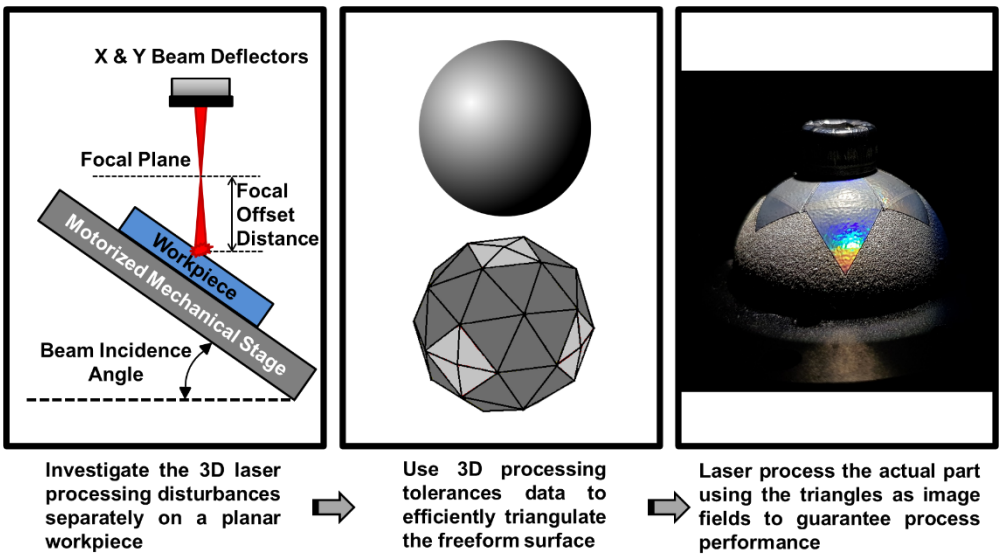

Figure 5.1 Chapter 5 graphical abstract

Keywords: 3D laser processing; freeform surface; surface partitioning; laser polishing; laser texturing; additive manufacturing

5.1. Introduction

Laser-based Powder Bed Fusion (LPBF) is a widely used additive manufacturing (AM) technology, commonly referred to as 3D printing, for producing near net shape engineering components. In the last decade LPBF has become a viable technology for a range of biomedical applications, more specifically in orthopedics, where it allows patient-specific and intricate designs with different mechanical and biological properties to be manufactured [1, 2]. One of the major shortcomings of LPBF technology is the surface integrity of the produced components, namely the resulting residual stresses and surface roughness, that have to be improved through post processing operations [3].

Titanium alloys are commonly used to produce biomedical implants and their mechanical polishing is undesirable due to their low thermal conductivity, high chemical reactiveness, high hardness and shear strength that lead to high tool wear and low processing rates [4-6]. Furthermore, custom tools and fixtures would be required to polish uniformly all functional surfaces of complex components. A promising alternative for finishing 3D printed components is laser polishing (LP) technology. In particular, the technology is a non-contact method, capable of processing freeform surfaces while retaining the geometrical accuracy obtained with the AM process. Furthermore, it is more environmentally friendly technology than commonly used chemical polishing processes.

Laser surface texturing (LST) as a technology for functionalizing surfaces was extensively investigated by researchers [7]. In the context of orthopedic applications, LST was shown to improve the performance of implants, namely by enhancing their

biocompatibility and also by strengthening their mechanical bond with bones [8, 9]. Laser induced periodic surface structures (LIPSS) in particular offer some appealing opportunities for enhancing the performance of biomaterials. They are a regular ripple pattern that can be generated on almost any material when the laser intensity is at or near the damage threshold of the target material. Their periodicity is usually just under the wavelength of the laser source. LIPSS generation is generally attributed to some sort of interference between the incident laser beam and the surface-scattered electromagnetic waves [10, 11]. Their sub-micron length scale offers advantageous interactions with bone cells [12, 13].

Most laser surface processing research was conducted on planar substrates, however, processing disturbances are present when processing complex shapes, such as the acetabular shells found in total hip replacements [14]. This spherical component can be produced to near net shape by LPBF. The shells feature an outer surface that can benefit from some advantageous functional enhancements, such as anti-bacterial or osteoconductive properties, potentially offered by LIPSS, while their inner surface must be polished in order to minimize the wear of polyethylene liners. Thus, it would be beneficial, from a productivity standpoint, for both surfaces to be processed in one setup, particularly by employing LP on the inner surface and LP followed up by LST on the outer surface of the spherical shells. In this way, coatings and mechanical machining operations could potentially be avoided, they are currently required for their manufacture.

Both LP and LST were investigated extensively and proven on planar surfaces [5, 9, 15-17]. However, when laser processing 3D or freeform surfaces, they first have to be partitioned into fields while taking into account factors that affect the process uniformity

and efficiency. In particular, variations in the beam incidence angle (BIA) and focal offset distance (FOD) when processing 3D surfaces directly affect the process performance. Therefore, these two factors should be taken into account when deciding how to partition such surfaces for laser processing [14].

The most common approach to laser process complex geometries is to apply the so-called layered method. For instance, Yung et al. used a pulsed fiber laser to polish additively manufactured spherical CoCr alloy components by splitting them into layers, i.e. splitting the sphere in segments along its axis, and thus reducing surface roughness by up to 93% [18]. Other approaches for laser processing 3D parts include: the use of surface tessellation/triangulation algorithms for partitioning surfaces into planar fields and then using different scan-head positions for processing each of them [19]; layering the scanning fields of the focusing lens onto the freeform surfaces [20]; projecting 2D images onto 3D surfaces [21]; and also some combination of the aforementioned approaches [22]. Although, there were significant efforts dedicated to finding a generic solution to this complex problem, all available approaches still require some compromises to be made, for instance, not factoring the effects of both BIA and FOD when partitioning 3D surfaces, using a large number of scanning fields or a large number of different fields' geometries. Therefore, further efforts are required to address these open issues, especially to consider simultaneously the effects of both BIA and FOD and minimize part repositioning by setting 3D laser processing tolerances to obtain the overall desired process performance and productivity, using the smallest number of processing fields possible.

In this paper a method for laser processing complex 3D components is proposed that allows a higher processing efficiency to be achieved by maximizing the use of high

dynamics galvo scanners and minimizing the number of processing fields all the while ensuring process performance. A pilot application of the proposed method is reported that demonstrates how different laser processing operations can be performed on 3D components, specifically, laser polishing and texturing was carried out on the surfaces of additively manufactured Ti-6Al-4V spherical shells.

5.2. Methodology for partitioning freeform surfaces

Contrary to conventional machining, such as milling, the laser beam does not need to be ‘in-contact’ with the workpiece. As such, laser processing setups and operations can tolerate some deviations in BIA from normal and also of some FOD before the process performance deteriorates. These intrinsic characteristics can be used advantageously through off-focus processing with varying BIA, and thus fully utilizing the high dynamics of beam deflectors while avoiding the need for constant refocusing. In addition, the use of relatively slow mechanical stages for part repositioning can be minimized by using as big as possible processing fields, and thus to increase the processing efficiency even further. However, the position of the scan-head relative to the working surface has an impact on process performance. Therefore, the effects of processing disturbances, i.e. deviations of the BIA from normal and off-focus processing, should be taken into account when processing strategies are designed, especially when partitioning 3D surfaces into laser processing fields [14]. A novel partitioning method is proposed in this research that employs an efficient strategy for tessellating 3D surfaces. The method is driven by predetermined 3D laser processing tolerances, i.e. max BIA and max FOD, to keep the process in control. In particular,

the geometrical parameters that are commonly used to control the tessellation in most CAD packages are set based on these 3D laser processing tolerances, in the proposed method.

5.2.1 Laser processing tolerances

The method requires the laser processing tolerances, i.e. the processing constraints associated with BIA and FOD, to be determined by conducting preliminary laser processing trials. Therefore, first, a laser processing operation, e.g. polishing, texturing or engraving, should be optimized on a planar substrate in 'ideal' conditions, i.e. in-focus (FOD = 0) and BIA normal to the surface, these processing parameters are then used as reference. Secondly, the effects of BIA and FOD on process performance should be investigated independently and quantified. Finally, cut-off values for BIA and FOD should be defined beyond which the process performance is no longer deemed satisfactory: they are referred to as processing tolerances in this research. The set of optimized processing parameters and processing tolerances, i.e. max BIA and max FOD, are specific for a given laser processing operation and substrate material. An example, how they can be obtained for a given laser processing setup, operation and material is provided in Section 5.3.

5.2.2 Surface tessellation

The surface tessellation process in the proposed method employs common algorithms available in most CAD packages and their respective set of geometrical parameters, i.e. the max edge length of a triangular field, the max chord height, and the tessellation angular tolerance. They are used to drive the partitioning process and, in the proposed method, are determined based on the 3D laser processing tolerances, i.e. the identified

BIA and FOD constraints for a given laser processing setup, operation and material. They define the 3D laser processing strategy, especially by partitioning 3D surfaces into triangular fields that are then used to determine scan-head positions and fields for subsequent processing. In particular, the following three constraints should be considered when executing the surface tessellation process.

i. The field of view (FoV) of the used focusing lens introduces a constraint with regards to the size of the triangular fields. In particular, the longest side of any triangular field (max edge length) is determined by the focusing lens's FoV as follows:

$$max\ edge\ length \leq \sqrt{2}\ s \qquad (1)$$

where: s is the length of the FoV side as shown in Figure 5.2.

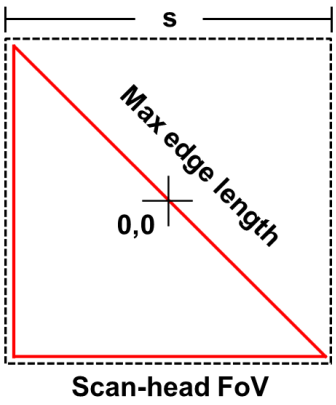

Figure 5.2 Triangle max edge length

Also, it should be noted that to make the best use of the available FoV for any given laser processing setup, the tessellation process should aim to generate triangular fields that are as close as possible to right-angle isosceles triangles, with a max edge length equal to the FoV diagonal as shown in Figure 5.2. Finally, the scan-head's (0,0) position should coincide with the triangle's circumcenter to meet the following processing tolerances.

ii. The processing tolerance defined by the FOD limit introduces a constraint on the maximum chord height in the tessellation process [23]. Especially, to keep the process in control the maximum chord height should not exceed twice the FOD limit, in particular:

$$max\ chord\ height\ \leq 2\ FOD\ limit \qquad (2)$$

In this way, the focal plane can be positioned halfway between the triangular field and the plane parallel to it that is also tangential to the 3D surface as shown in Figure 5.3. Thus, the depth of focus associated with any given laser processing setup will be fully utilized.

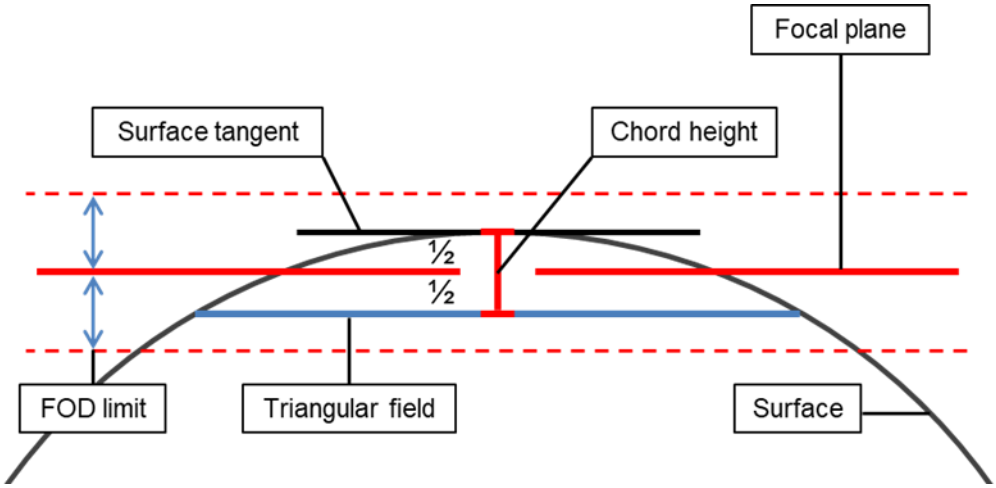

Figure 5.3 Tessellation max chord height

iii. The tessellation angular tolerance defined as the angle between the normal vectors of two adjacent triangles [24] should be constrained by the BIA limit. Particularly, the angle between surface tangents and the triangular fields, θ, does not exceed a given angular tolerance, α, when using STL tessellation algorithms [23]. Therefore, α can be used to control the BIA on the 3D part. If a telecentric focusing lens is used, α would be constrained by the BIA limit at the vertices of the triangular fields as shown in Figure 5.4a. However, when using the full FoV of F-Theta lenses, the lens's max deflection angle, β, should be also considered (Figure 5.4b) when defining a constraint for α. Especially, the relationships between θ, α and BIA limit in the case of telecentric lenses can be expressed as follows:

$$\theta \leq BIA\ limit \text{ and thus } \alpha \leq BIA\ limit \qquad (3)$$

While in the case of F-Theta focusing lenses, the relationship will be:

$$\theta \leq BIA\ limit - \beta = BIA\ limit - \tan^{-1}\left(\frac{\sqrt{2}/2.s}{f}\right) \text{ and thus } \alpha \leq BIA\ limit - \beta \qquad (4)$$

where: s is the lens FoV size and f its focal length.

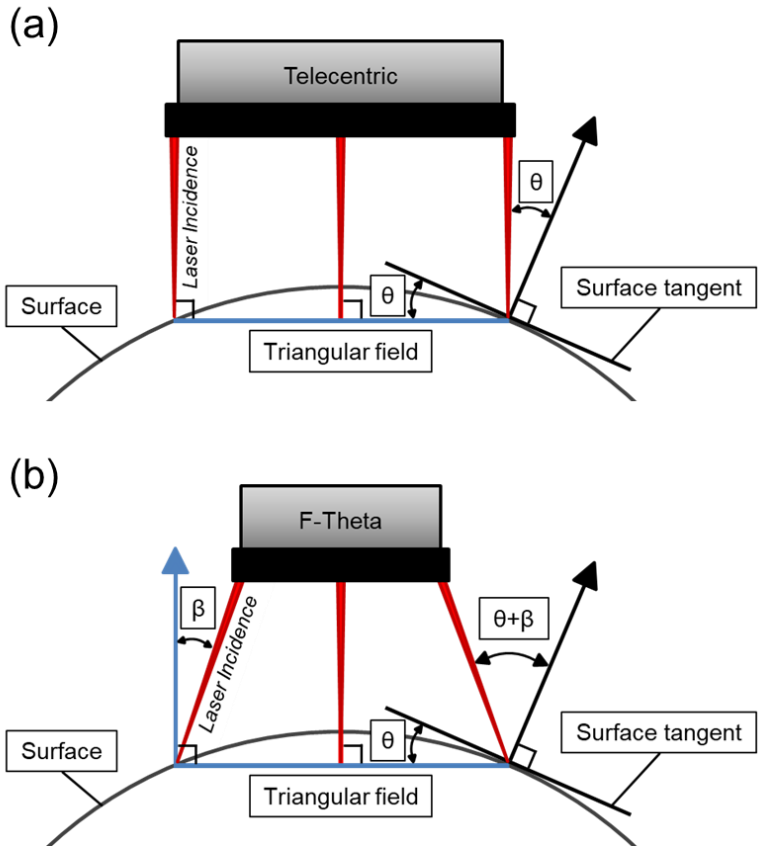

Figure 5.4 A schematic representation of BIA relative to the normal vectors and triangular fields in the case of (a) telecentric lenses and (b) F-Theta lenses.

5.2.3 Fields' distortion

Prior to laser processing the generated triangular fields onto the freeform surface, they must be, along with any feature they enclose, adjusted for any projection distortion. Essentially, the borders and any pattern or geometry inside the triangular fields must be projected onto the freeform surface (the triangles' vertices lie on the surface and therefore they would remain unchanged). This is necessary to make sure that the different fields stitch as required on the 3D surface and that patterns or structures are undistorted on the final part. The adjusted fields' borders or stitching areas would remain within the laser processing tolerances, because:

1) They lie between the between the triangular field and the plane parallel to it that is also tangential to the freeform surface. The fields' borders would essentially stay within the process's depth of focus.

2) The angle between the normal to the surface and the laser beam is smaller at the triangular fields' borders than at their vertices where it is highest.

The adjusted fields are effectively the inverse of the projections of the undistorted triangles onto the freeform surface as shown in Figure 5.5. As an example, the barrel and pincushion distorted triangular fields on the concave and convex surfaces are essentially the projections of an undistorted triangle from the projection plane (see Figure 5.5a), whereas the pincushion and barrel distorted triangles in the projection plane would be converted into undistorted triangular fields on the freeform surface (see Figure 5.5b).

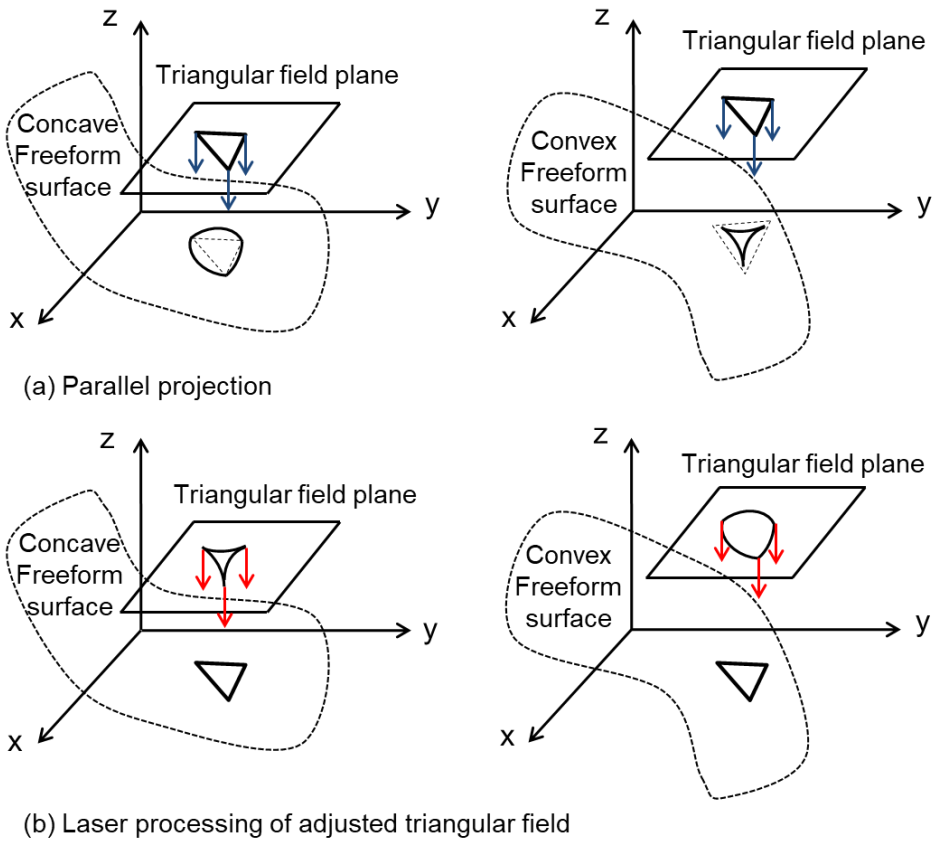

Figure 5.5 Schematic representations of projection distortions

5.2.4 Fields' overlapping

Finally, the projection-adjusted triangular fields may need to overlap when executing some laser processing operations, e.g. laser polishing, as it would be discussed in Section 5.4.2. If a given laser processing operations does not require any overlapping, regardless a small one should be introduced to compensate for any workpiece repositioning errors, e.g. because of some repeatability errors associated with the mechanical stages and/or beam deflectors. It is worth noting that the overlaps are introduced geometrically by proportionally extending the boundaries of the adjusted triangular fields along vectors originating at their centroids to maintain the overall field geometry as depicted in Figure 5.6. It should also be noted that the overlapping region

does not necessarily satisfy the laser processing tolerances associated with FOD and BIA, as they are just extensions beyond the original bounds of the triangular fields. Therefore, a certain ‘safety factor’ should be used when setting the 3D processing tolerances to account for potential overlapping requirements, e.g. dictated by a specific laser processing operation or setup.

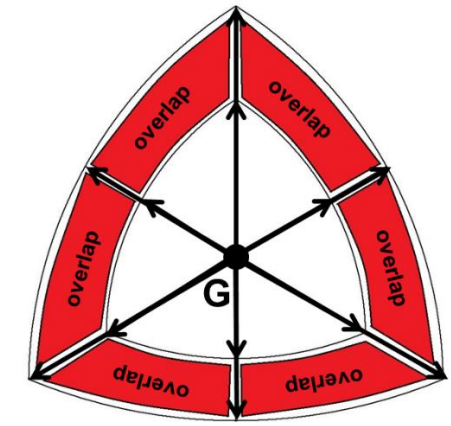

Figure 5.6 An example of boundaries’ extension of a distortion-adjusted triangular field

5.3 Pilot implementation

A pilot implementation of the proposed methodology is presented in this section. Especially, as it was already mentioned in the introduction, it would be advantageous to perform multiple laser processing operations on acetabular shells found in total hip replacements. Therefore, a spherical component that resembles the functional surfaces of such shells was selected to demonstrate the capabilities of the proposed method. In particular, spherical shells produced to near net shape by LPBF were laser polished and textured by applying the proposed method, i.e. to partition their spherical

surfaces for follow up laser processing. The conducted experimental study demonstrating the proposed surface partitioning/tessellation method is presented in this section.

5.3.1 Spherical shells produced by laser powder bed fusion

The spherical shells were built using a LPBF system, i.e. the RenAM 500M machine from Renishaw. The build parameters used to produce the shells were as follows: 200 W average laser power, 90 μm point distance (distance between 2 laser irradiation positions), 60 μs exposure time, 90 μm hatch spacing and 30 μm layer thickness. The material used to build the shells was grade 23 Ti-6Al-4V, low interstitial.

The spherical shells were 30 mm in diameter with a thickness of 1 mm. An initial optimization of LP and LST processes, required for the implementation of the proposed methodology (see Section 5.2.1), was conducted on planar substrates. They were produced with the shells in the same build. The build direction for the planar samples was normal to the substrates and their surface roughness, i.e. initial arithmetical mean height (Sa) and root mean square height (Sq), were approximately 5.0 μm and 7.0 μm, respectively.

5.3.2 Laser polishing

The LP operation was optimized by conducting experimental trials using a MOPA-based Yb-doped fiber nanosecond laser source (SPI G4 50W HS-S) with the following technical characteristics: 50W average power, 0.71mJ maximum pulse energy, pulse duration from 15 to 220 ns, 1MHz maximum repetition rate, 1064 nm center wavelength and beam quality M^2 better than 1.3. The beam was focused using a telecentric lens with a 100mm focal length down to a spot size at the focal plane of approximately 40

μm. Furthermore, the LP trials were carried out in a controlled Argon environment, flowing at 12L/min to maintain a positive pressure inside the chamber, in order to prevent surface oxidation and cracking [5, 25].

The LP parameters optimized by Ma et al. [5] on planar 3D printed Ti-6Al-4V substrates are provided in Table 5.1. They were used as a reference to study the effects of 3D laser processing disturbances on the LP performance. In particular, samples were processed in an inert gas-controlled environment using the LP settings in Table 5.1. The scan paths used were bidirectional with perpendicular and parallel tracks having the same stepover distance. The BIA and FOD values were varied independently and thus to investigate their effects on the surface roughness of LPBF Ti-6Al-4V substrates.

Table 5.1. Laser polishing parameters

Pulse Energy (μJ)	Pulse Duration (ns)	Pulse Repetition Rate (Hz)	Scanning Speed (mm/s)	Stepover Distance (μm)
80	220	500,000	200	16

5.3.3 Laser surface texturing

Laser sub-micron texturing was conducted using a femtosecond (fs) fiber laser (Satsuma from Amplitude Systemes) with the following technical characteristics: 5W average power, 10μJ maximum pulse energy, 310 fs pulse duration, 500 KHz maximum repetition rate, 1030 nm center wavelength and beam quality M^2 better than 1.2. The beam was focused using the same telecentric lens down to a spot size at the focal plane of 40 μm. The two laser sources used for the LP and LST operations were

integrated into a Lasea LS5 system and the laser processing setup is illustrated in Figure 5.7.

LIPSS were used to texture the surfaces of laser polished Ti-6Al-4V substrates produced by LPBF. The parameters' domain for producing LIPSS is relatively big and therefore the LST parameter settings used in this research were selected based on a previously reported optimization study [14]. They are provided in Table 5.2. Again, as it was the case with the LP operation, planar Ti-6Al-4V substrates produced by LPBF and then laser polished with the reference parameters in Table 5.1 were textured using the optimized LST parameters. These experimental trials were used to investigate the effects of FOD and BIA on the resulting sub-micron texture.

Table 5.2. Laser surface texturing parameters

Pulse Energy (µJ)	Pulse Duration (fs)	Pulse Repetition Rate (Hz)	Scanning Speed (mm/s)	Stepover Distance (µm)
2.8	310	250,000	1500	6

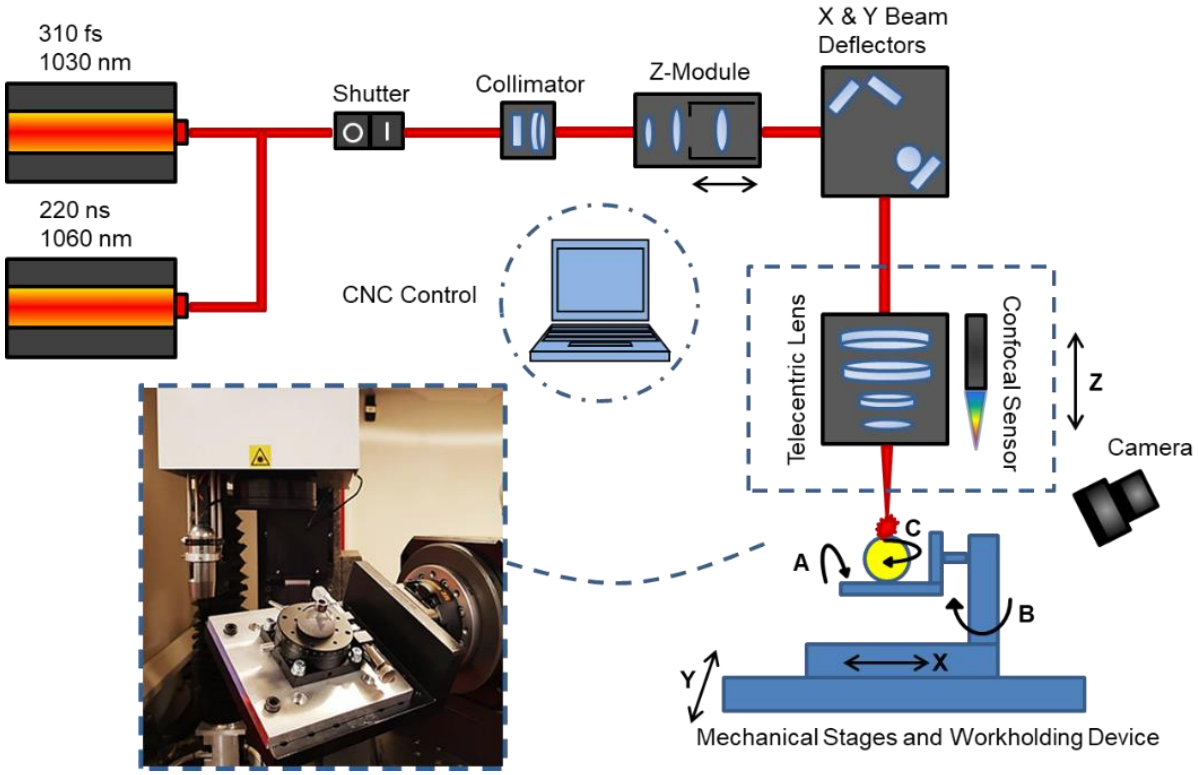

Figure 5.7 The used multi-axes laser processing setup

5.3.4 Partitioning of spherical surfaces for laser polishing and texturing

A triangulation algorithm based on the geometrical arrangements of geodesic polyhedra was used to tessellate the spherical surfaces, namely tetrahedra, octahedra and icosahedra arrangements were considered [26]. This algorithm is very efficient when applied on spheres as it generates the smallest number of triangular fields, for a given set of constraints, and the tessellation processes is very uniform. In particular, a very small number of different triangles are generated when tessellating a sphere, only 2 in this research as 2 subdivisions (3 frequencies) were examined for each of the 3 geometrical arrangements.

A MATLAB program was created for tessellating spherical surfaces that uses as inputs laser processing tolerances and the sphere diameter. The program tessellates spheres with the biggest possible triangles, hence generates as small as possible number of fields, with respect to a set of processing tolerances, i.e. max edge length, max chord height and the set angular tolerance. Furthermore, the program applies the necessary corrections to account for any projection distortion and can add an optional overlapping between the fields to compensate for any workpiece repositioning errors as discussed in sections 5.2.3 and 5.2.4. It can serve as one-step solution for partitioning and fully pre-processing the CAD data necessary for laser processing spherical surfaces, and therefore avoiding the use of expensive CAD/CAM packages. The algorithm implemented into the MATLAB program is outlined in Figure 5.8.

The advantages of this partitioning method are highlighted in Figure 5.9. In particular, if a sphere with a 30 mm diameter is to be tessellated by using max chord height of 1.14 mm as a geometrical constraint, a common STL tessellation generated in PowerShape yielded 120 triangles with varying geometries while only 72 triangles of 2 different isosceles types would be generated using octahedron partitioning. Therefore, geodesic polyhedra arrangements are more effective in pre-processing spherical surfaces for laser processing.

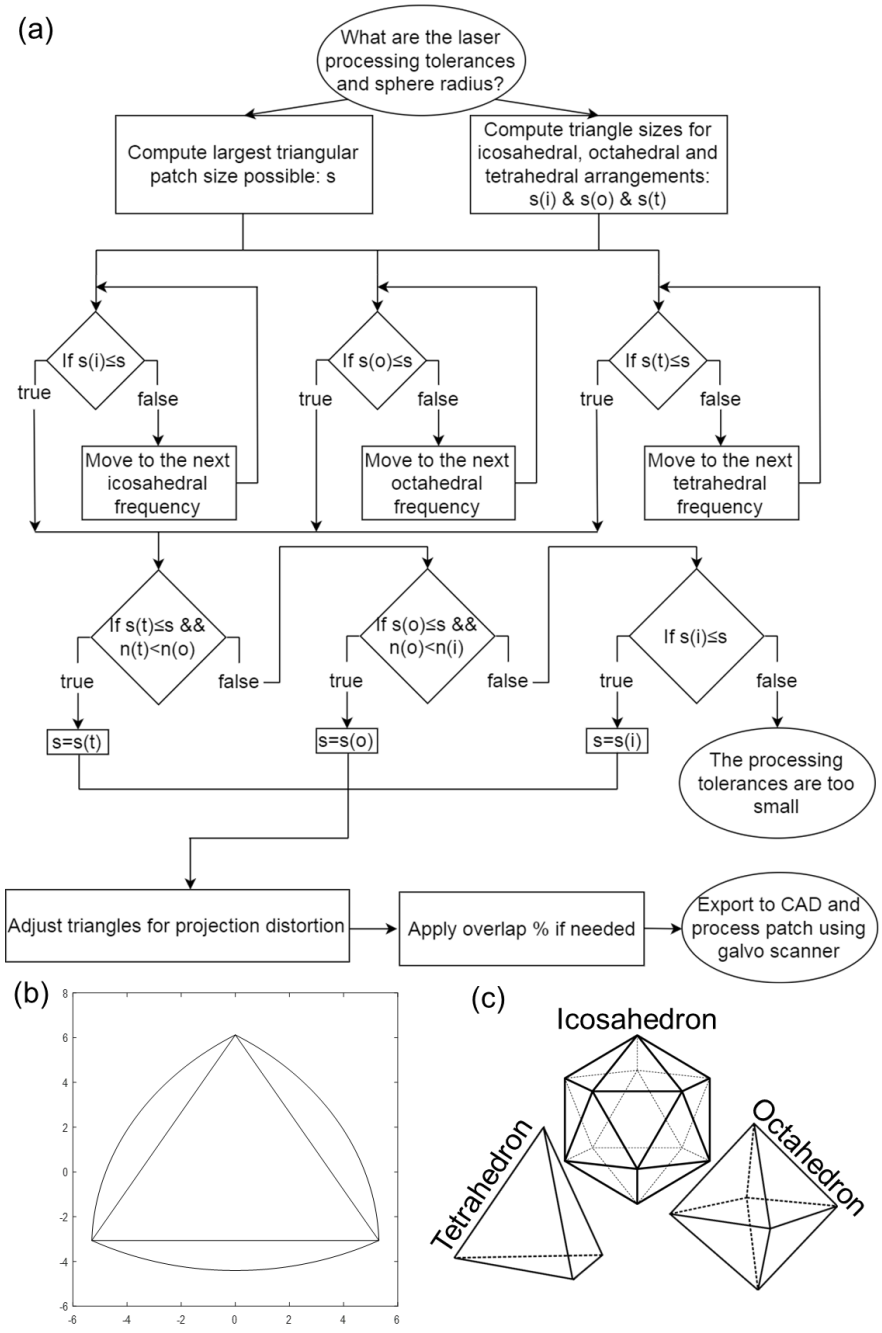

Figure 5.8 An overview of the tessellation method: a) the flowchart of the algorithm implemented in the MATLAB program b) an example of an output field with the projection distortions c) the examined types of geodesic polyhedra

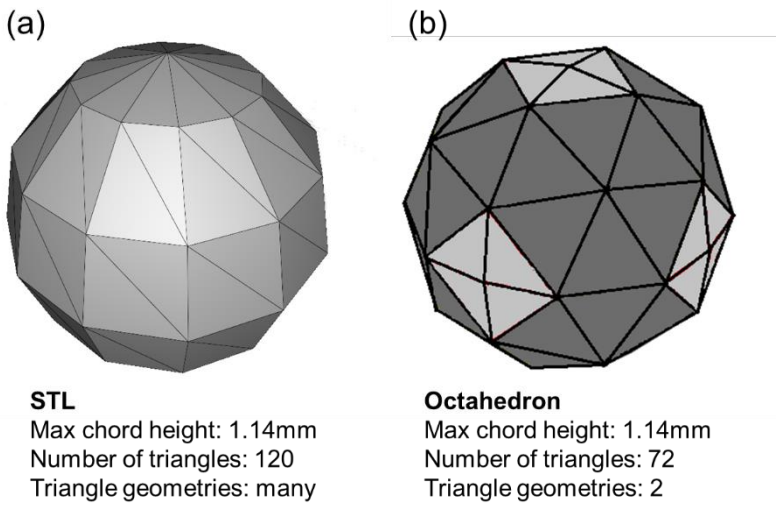

Figure 5.9 Comparison between STL and geodesic tessellations

5.3.5 Surface characterization

Topographies and surface roughness of planar and spherical surfaces were assessed using focus variation (FV) microscopy, specifically with Alicona G5 InfiniteFocus system. The surface roughness parameters were measured over a 812.173x812.173 µm area using the 20x objective with polarization and a vertical resolution of 50 nm (0.075 µm smallest measurable S_a). The exposure used was 38.72 ms and the cut-off wavelength λ_c was 162.346 µm. The surface morphology was also assessed via scanning electron microscopy, specifically the Jeol JCM-6000 with EHT of 15.00kV.

5.4 Results and discussion

The results of the pilot implementation of the proposed methodology are presented and discussed in this section. In particular, it includes the carried-out experiments to determine the 3D tolerances of the LP and LST operations. Also, the application of the

MATLAB program to generate the necessary CAD models for executing these two operations on the spherical surfaces.

5.4.1. Laser polishing process

The first step in applying the proposed methodology is to identify a set of optimized LP parameters for processing planar Ti-6Al-4V samples produced by LPBF. Then, they are used to study the effects of laser processing disturbances, i.e. variations of FOD and BIA, on the LP performance.

The reference LP parameters provided in Section 5.3.2 were used in the pilot implementation to investigate the effects of the two processing disturbances**.** First, a planar Ti-6Al-4V sample produced by LPBF was LP'd with the optimized offset and with BIA normal to the substrate surface. The roughness of the sample, i.e. S_a and S_q, was reduced from around 5.0 µm and 7.0 µm down to under 0.2 µm and 0.2 µm, respectively, resulting in a maximum improvement of 96% as shown in Figure 5.10.

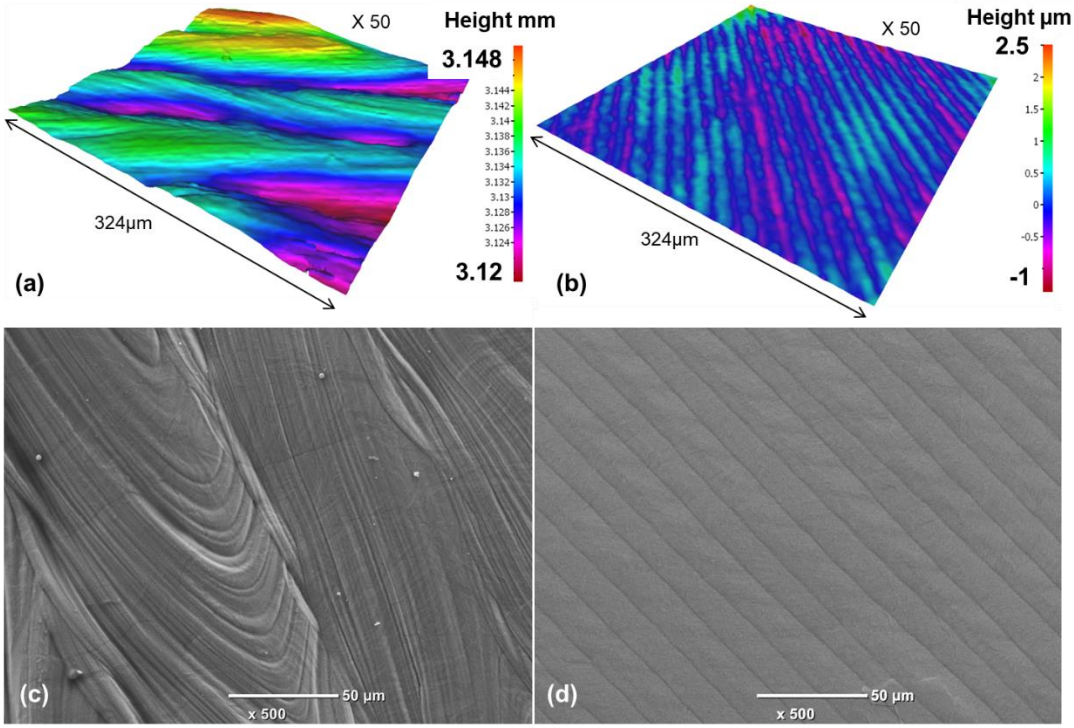

Figure 5.10 Laser polishing performance on a planar 3D printed Ti-6Al-4V sample a) 3D topological view of as-printed surface b) 3D topological view of polished surface (c) SEM micrograph of as-printed surface d) SEM micrograph of polished surface.

The next step was to investigate the effects of FOD and BIA separately on planar Ti-6Al-4V surfaces by using as reference the optimum LP results obtained prior.

The FOD value was varied in increments of 0.5 mm above and below the substrate surface of the planar samples and the FOD effects on the surface roughness were assessed. The measurement results obtained with FOD above and below the surface were similar and therefore only those obtained above the focal plane are discussed further. The LP results were considered acceptable when S_a was less than 0.5 µm. When the FOD was in the range from 2.5 to 3.5mm the polishing performance was

tolerable, and the lowest roughness value of 0.18 µm was obtained with a FOD of 3 mm as shown in Figure 5.11. At a FOD of 2mm, some signs of laser ablation were observed on the surface of the Ti-6Al-4V sample, whereas at 4mm FOD, the waviness of the printed substrates was not reduced. Therefore, FOD of 3 mm with a tolerance of 0.5 mm was selected to partition and polish the fields of the printed spherical shells.

Assuming a perfect Gaussian distribution of the beam intensity, its diameter at an offset z from the focal plane can be calculated as follows [27]:

$$D(z) = D_0\sqrt{1 + (\frac{z}{z_R})^2} \qquad (4)$$

where: D_0 is the beam diameter at the focal plane and z_R the Rayleigh length. Thus, the beam spot size increases from around 80 to 140 µm when FOD is raised from 2 to 4mm, resulting in a decrease of power density, a key laser polishing parameter, that is inversely proportional to the beam spot size by nearly a factor of 2.

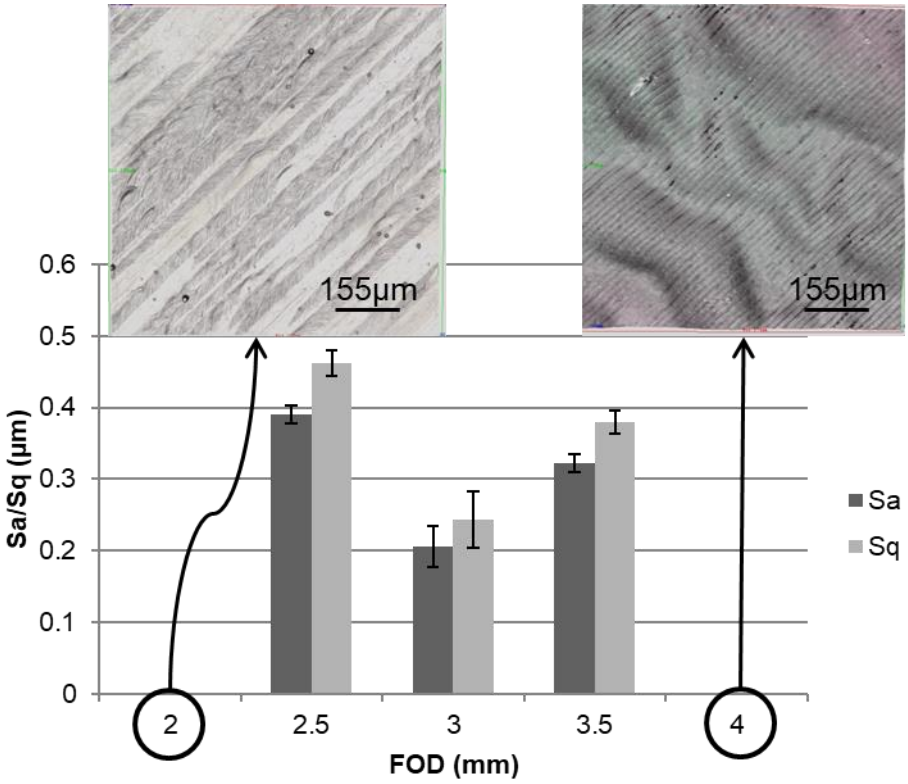

Figure 5.11 Effects of FOD on polishing performance

(n=3, error bars represent the standard deviation)

Next, the BIA was varied in increments of 10˚. A steady increase in surface roughness was observed with the increase of BIA as depicted in Figure 5.12. The polishing process was still acceptable at BIA of 40˚, however at 50˚ a sharp deterioration in the LP performance occurred, surface cracks and increased waviness were observed on the surface. At higher BIAs the Gaussian energy distribution of the beam is distorted and the pulse power density is compromised [22]. Furthermore, the material's reflectivity increases at high BIAs and thus the laser absorption is reduced [28].

Therefore, the max BIA when polishing LPBF Ti-6Al-4V should be limited to 40˚ in this setup.

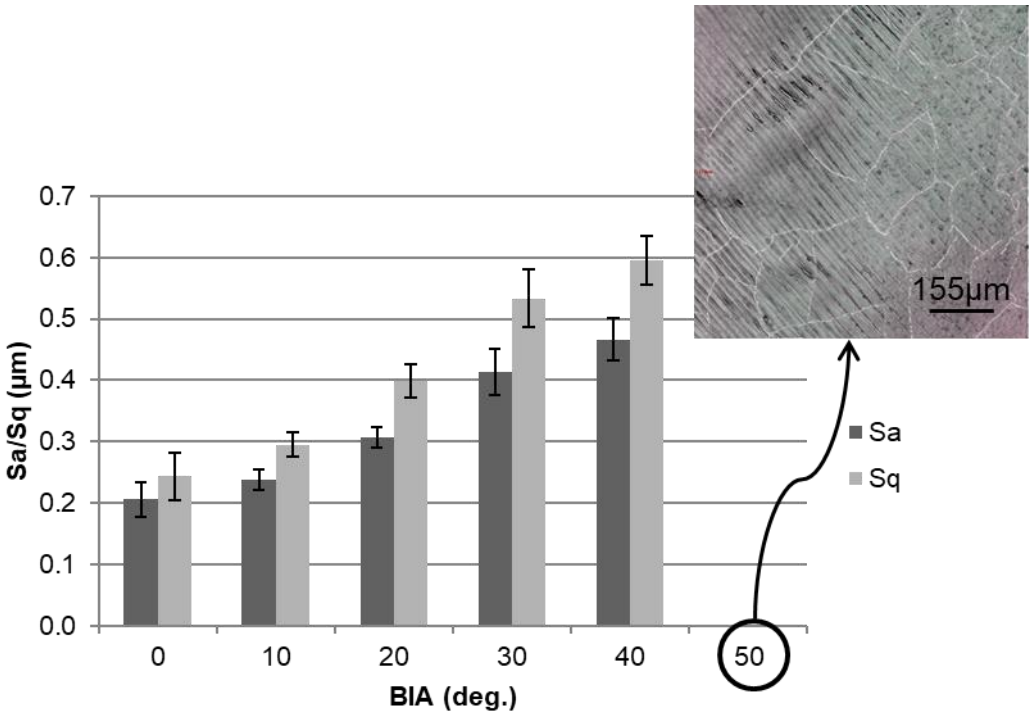

Figure 5.12 Effects of BIA on polishing performance

(n=3, error bars represent the standard deviation)

5.4.2. Laser polishing fields' stitching

The stitching areas between LP fields should be analyzed too, as they can affect the performance of the follow up LST operation and the overall part aesthetic. The surface defects in these areas can be minimized by counteracting the negative dynamics effects of the beam deflectors. In this research, the negative dynamic effects were minimized by employing a built-in software tool in the used laser processing setup [29]. However, the conducted planar LP trials revealed that there were some surface defects

in spite the use of this tool at the borders between the LP fields and the un-processed surface. In particular, there were surface cracks and some material build-up near the fields' borders followed by a groove before transitioning back to the original, unprocessed surface, as depicted in Figure 5.13. Those are predominantly due to the flow of the molten material on the surface [15] , see Figure 5.16.

A representative SEM image of surface defects at the border between two adjacent LP fields without any overlapping is provided in Figure 5.14a. The formation of peaks and valleys between the fields was aggravated by stitching them as precisely as possible. Therefore, the use of some overlapping to minimize these defects was investigated as a potential solution.

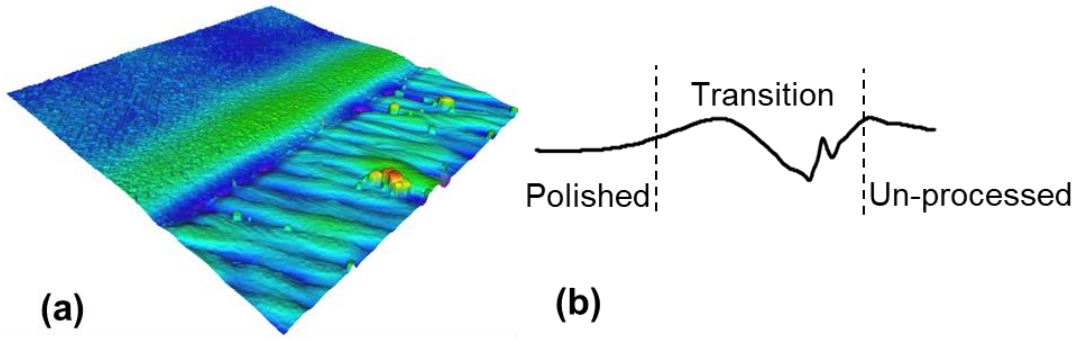

Figure 5.13 An analysis of the transition zone between a laser polished field and un-processed surface: a) 3D representation of the transition zone b) a representative surface profile of the transition zone obtained via FV microscopy

The level of overlapping between the LP fields was varied to investigate its impact on resulting surface morphology. LP trials of fields with varying overlapping areas were conducted while the same LP strategy, processing parameters (as given in Section 5.3.2) and waiting time between any two adjacent fields were used. The level of overlapping was selected to cover the material build-up at the border regions between

adjacent LP fields when no overlap is applied, the width of these regions was measured to be less than 200 μm. The overlapping distance was controlled using Aerotech's PRO165LM series mechanical stages with a stated accuracy of ±1 μm.

The increase of the overlapping distance from 0 to 160 μm reduced surface cracks and the depth of the resulting 'valleys' between the LP fields and thus a smoother transition between them was achieved. In particular, the depth of the 'valleys' on the LP surfaces was measured using the FV microscope and it decreased steadily from approximately 35 μm to just under 7 μm when the overlap distance was increased from 0 to 160 μm as shown in Figure 5.14. Therefore, when surfaces are partitioned for LP, a controlled overlapping between the fields should be introduced to minimize any side effects, and thus achieving the smoothest possible transition between them. In this way, the uniformity of LP surfaces can be improved substantially and parts' aesthetics can be enhanced.

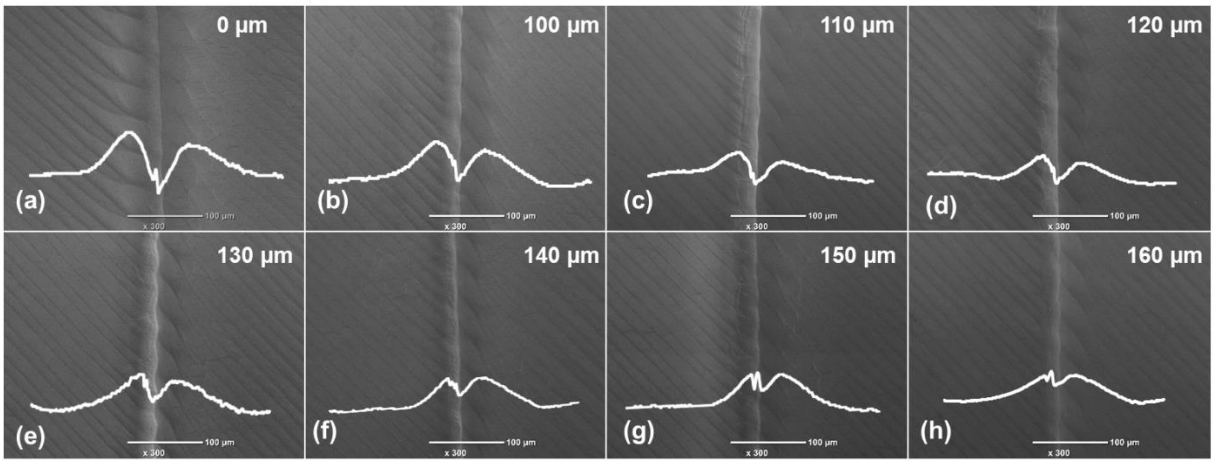

Figure 5.14 SEM micrographs and representative profiles of laser polished fields' borders when the overlapping distance was increased from 0 to 160 μm

Increasing the overlap distance further up to 200 μm, showed no sign of improvement to the joining process; the border area seemed more or less identical and therefore a 160 μm overlap was used in the LP operation.

5.4.3. Laser surface texturing of laser polished surfaces

The next step in applying the proposed methodology is to identify a set of optimized LST parameters for processing laser polished planar Ti-6Al-4V samples produced by LPBF. Again, as it was the case with the LP operation, they are used to study the effects of laser processing disturbances, i.e. variations of FOD and BIA, on the LST performance.

The reference LST parameters provided in Section 5.3.3 were used in this pilot implementation to investigate the effects of processing disturbances**.** In particular, the printed Ti-6Al-4V planar substrates polished using the laser parameter settings in Table 5.1, were successfully textured using the LST parameters provided in Table 5.2 when no processing disturbances are present. The substrates were fully covered with LIPSS and the preceding LP operation did not seem to affect in the LIPSS formation in any way. As expected, the resulting sub-micron ripples were perpendicular to the laser polarization vector and their periodicity was 860 ± 10 nm. The ripples formed over the visible LP track lines with no apparent alterations to their morphology as can be seen in Figure 5.15a.

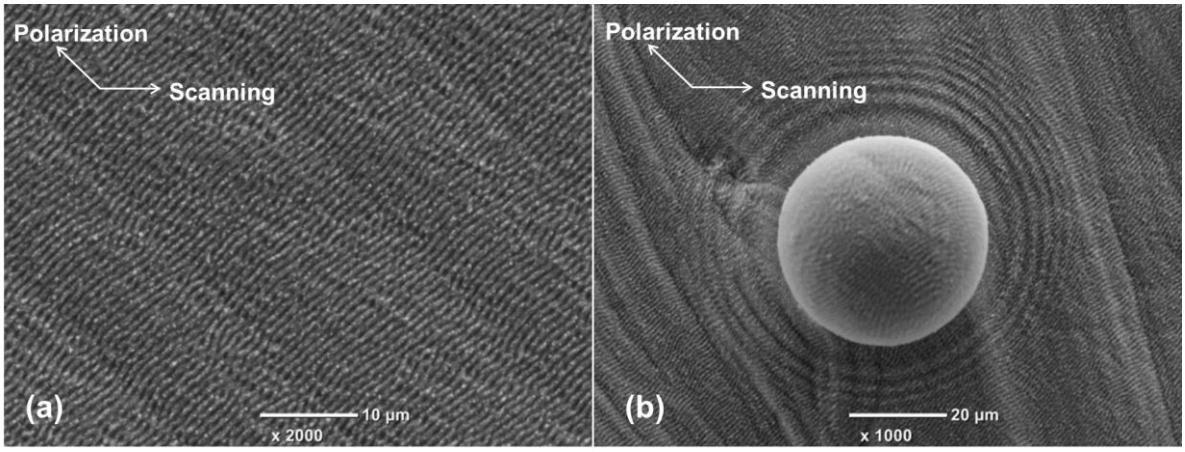

Figure 5.15 (a) Laser surface texturing on laser polished surface (b) Laser surface texturing on as-printed surface

The LP operation prior to LST was essential for the formation of regular and homogenous LIPSS. Any surface defects, such as sharp height variations, scratches and un-melted powder particles, as depicted in Figure 5.15b, can disturb the LIPSS formation and their morphology, and can thus affect their functional performance [14, 30].

The next step was to investigate the effects of the FOD and BIA separately on planar LP Ti-6Al-4V surfaces by using as a reference LST results obtained without any processing disturbances.

With the increase of FOD, the laser spot size would increase too, and thus the pulse fluence would effectively be reduced. The formation of LIPSS on surfaces requires a certain threshold fluence under which no texturing would occur. Therefore, the max acceptable FOD was determined experimentally by increasing FOD until this threshold fluence was reached on the laser polished Ti-6Al-4V substrates. In particular, the FOD was deemed acceptable if the substrate surface was entirely covered in LIPSS. Based

on the conducted LST trials on laser polished Ti-6Al-4V samples, the FOD limit was found to be 0.8 mm.

Regarding the BIA, its increase leads to an increase in the ripples' periodicity, as was already reported by other researchers [31]. For the considered texture in our experimental study, LIPSS periodicity variations were acceptable and therefore, the BIA was deemed not important. Consequently, the FOD was considered as the only limiting factor and thus used as the sole 3D processing tolerance for the LST operation on 3D surfaces.

Finally, the level of overlapping of LST fields was also investigated similarly to the LP process. However, it became immediately evident that varying the overlapping between the LST fields did not influence LIPSS formation as no discernible differences could be seen in SEM micrographs when the overlapping levels were varied. Therefore, it was concluded that overlapping between LIPSS fields was not necessary. Furthermore, the morphology of LIPSS was examined at the border area between two LP fields with a 160 μm overlap. Again, there were no alterations to their periodicity, orientation or regularity as depicted in Figure 5.16.

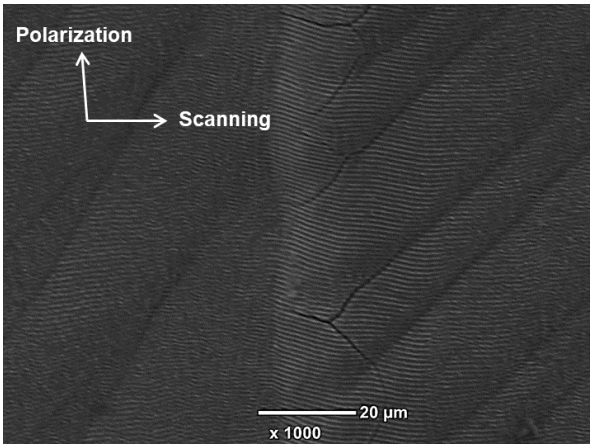

Figure 5.16 LIPSS over a representative border between two laser polished fields with a 160 µm overlap

5.4.4. Laser polishing and surface texturing of Ti-6Al-4V spherical shells

Prior to processing the spherical shells, the positional accuracy and repeatability of the manual C rotary axis to be used in the experiments, were determined by conducting some trials. In particular, equidistant crosses on the mirror finish surface of ball bearings were produced using the fs laser while repositioning them with the manual C rotary axis. The obtained actual distances between the crosses were compared with the nominal one to judge about the positioning accuracy. In addition, a second set of crosses was produced, and the displacements between the first and second set were used to assess the process repeatability. The standard deviations of those measurements were used to quantify the processing uncertainties associated with the used experimental setup. In particular, the trials were repeated 6 times and the distances between crosses were measured using the 20x objective of the FV microscope. The standard deviation of these measurements was 33 µm, both for positional accuracy and repeatability, and therefore this was considered to be the uncertainty associated with the used laser processing setup.

The MATLAB program described in Section 5.3.4 was used to partition and fully pre-process the CAD model of the spherical shell by using as inputs the shell diameter and the laser processing tolerances associated with LP and LST operations (see Sections 5.4.1 and 5.4.3). In particular, the spherical surface was partitioned into 80 triangular fields with an Icosahedral arrangement by inputting the LP processing tolerances of 0.5 mm and 40˚ for FOD and BIA respectively. By increasing the FOD tolerance to 0.57 mm it was possible to reduce the number of triangular fields down to 72. This was achieved at the expense of a 35 μm increase in FOD on either side of the focal plane only, which was considered an acceptable compromise to the LP process considering the significant reduction in processing time. The resulting partitioning of the spherical shell for the LP operation was comprised of only two sizes of triangular fields that formed the second sub-division (third frequency) of the octahedron with the geodesic notation $\{3,4+\}_{0,3}$.

As for the LST operation, the input for the MATLAB program was a processing tolerance of 0.8 mm for FOD and no constraints with regard to BIA, it generated the same triangular arrangement as for the LP process. Thus, both operations utilized the same geodesic arrangement while satisfying their respective processing tolerances.

Furthermore, the program applied the necessary corrections for projection distortion and added the necessary overlapping between the fields for the LP operation. In particular, considering the minimum overlapping distance of 160 μm required for the LP operation (see Section 5.4.2) it was necessary to adjust the triangular fields, accordingly, using the MATLAB program as described in Section 5.2.4. The smallest distance from the centroid to the border of the triangular patch in the generated CAD model was identified to be 1.6805 mm, and therefore the respective overlapping

percentage to ensure a minimum overlap distance of 160 μm was calculated as follows:

$$\frac{0.5 \times overlap\ distance}{\min distance\ from\ centroid} \times 100 = \frac{0.5 \times 0.16}{1.6805} \times 100 = 4.76\% \quad (6)$$

Thus, taking into account the relatively small compensation required for the processing uncertainty associated with the used machine setup, in addition to the necessary overlapping of 4.76%, the adjustment applied to the fields was increased to 5% for both operations for simplicity, since overlapping did not have an effect on the LST process.

The LPBF Ti-6Al-4V spherical shells were then polished and subsequently textured using the laser processing setup shown in Figure 5.7, while the CAD data for the LP and LST operations was generated by applying the geodesic triangulation algorithm with the identified processing tolerances in Sections 5.4.1 and 5.4.3. To assess the LP performance, the surface roughness was measured 3 times in 3 different areas within a triangular field as shown in Figure 5.17b and their borders were examined (Figures 5.17c and d).

The proposed tessellation method in Section 5.2.2 takes into account the FOD and BIA constraints associated with the LP and LST operations, and therefore should lead to a process performance within the pre-defined limits. It is expected for the two processes to be near their limits at the vertices of the triangular fields. The obtained average S_a values on the spherical surface were 0.38, 0.42 and 0.51 μm in the areas 1, 2 & 3, respectively (Figure 5.17b). As expected, area 3, the closest to one of the triangle's vertices exhibited the highest S_a, just marginally higher than acceptable value of 0.5 μm. Furthermore, the roughness in area 2 was slightly higher compared to that

obtained in area 1. This could be explained with the FOD effects on the LP performance, particularly, the FOD was higher in area 2 compared with that in area 1. Overall, the LP performance on the spherical shells was slightly behind when compared to the results obtained on planar substrates, but this was expected. The higher roughness observed on the laser polished 3D surfaces could be attributed to the presence of a combined effect from both processing disturbances, i.e. FOD and BIA, while they were investigated separately in section 5.4.1. Another possible explanation that could have impacted the polishing results on the sphere is the laser fields' geometry. Due to the thermal nature of the ns laser polishing process, the size of the processed area directly correlates with the applied thermal load onto the surface, an important factor that impacts this polishing process based on surface re-melting [32]. In fact, smaller laser fields reduce heat dissipation from the processing area whereas larger ones stretch the temporal distances between consecutive scan lines and subsequent passes and thus allow for some cooling to occur. In the given pilot implementation, the triangular fields were comparable in size to the 3x3 mm square fields used to optimize the LP process prior in sections 5.4.1 and 5.4.2. However, if this is not the case, then some compensation should be introduced in the LP parameters to account for the discrepancy in thermal load associated with the size difference. Regardless, the LP process still performed within the set tolerable limits, especially, average S_a was below the acceptable chosen threshold value of 0.5 µm.

The borders between the LP fields were then examined by taking surface profiles. The maximum depth of the resulting 'valleys' at the borders was 8 µm and thus slightly higher compared to on the planar samples where it was less than 7 µm (Figure 5.17d).

This can again be attributed to the presence of a combined effect and/or the different patch geometry. Still, the difference is negligible.

Finally, regarding the LST process, the triangular fields were fully covered with LIPSS and their light diffraction characteristic can be clearly seen in Figure 5.17a.

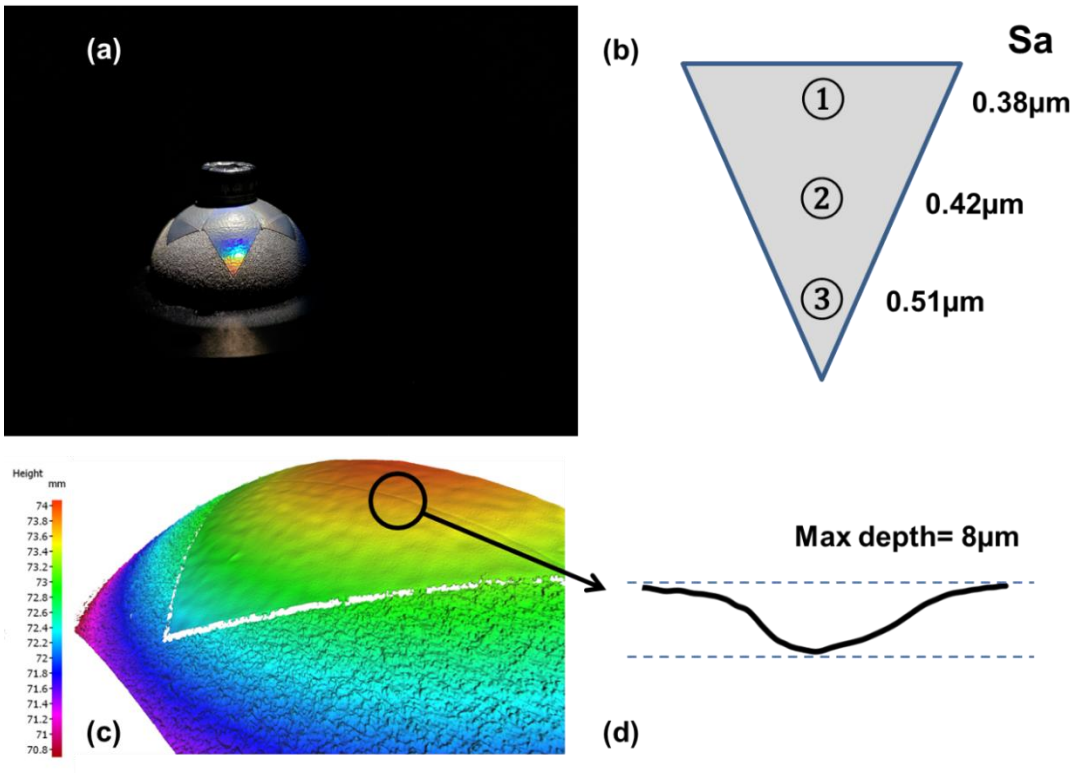

Figure 5.17 The results obtained on additively manufactured Ti-6Al-4V spherical shells: (a) a laser polished and textured spherical shell (b) three areas where surface roughness measurements were taken over the laser polished fields (c) 3D topological view of laser processed area (d) a representative profile scan of a border between two laser polished fields with the applied overlap

5.5. Conclusion

The paper demonstrates a significant development in 3D laser processing technology. Following a set of preliminary experiments, the empirical 3D limitations of a given laser process are used as input arguments to efficiently tessellate freeform surfaces. The resulting triangular partitions then serve as laser processing fields. By employing this method, processing efficiency is maximized by minimizing part repositioning, maximizing the use of fast galvo scanners, and ensuring process performance within the laser fields. In the pilot implementation, the new approach was used to successfully laser polish and texture the surface of 3D printed Ti-6Al-4V spherical shells. The presented method can be applied to any 3D part, granted the laser operation has some flexibility in terms of focal offset and beam incidence and the beam line of sight is uninterrupted. Considerations regarding patch joining and the combined effect of the beam angle of incidence and focal offset on the laser process performance should be made when using this method.

In future work, other approaches for improving the stitching quality between the triangular fields can be investigated, for example, randomizing the overlap between scanning vectors and their position in the joining area, in order to mask their presence. While the combined effect present in 3D laser processing could be measured empirically for a given laser task, greatly increasing the number of initial experiments, alternatively, modelling the beam energy distribution over the 3D part could potentially help better understand and quantify its effects.

Acknowledgment

The research reported in this paper was supported by a H2020 Factory of the Future projects, “High-Impact Injection Moulding Platform for mass-production of 3D and/or large micro-structured surfaces with Antimicrobial, Self-cleaning, Anti-scratch, Anti-squeak and Aesthetic functionalities” (HIMALAIA) and the UKIERI DST programme “Surface functionalisation for food, packaging, and healthcare applications”. The authors would like to acknowledge also the collaboration with LASEA SA, Belgium within the framework of the ESIF project “Smart Factory Hub” (SmartFub).

References

1. Javaid, M. and A. Haleem, Additive manufacturing applications in orthopaedics: A review. J Clin Orthop Trauma, 2018. 9(3): p. 202-206.

2. Sing, S.L., et al., Laser and electron-beam powder-bed additive manufacturing of metallic implants: A review on processes, materials and designs. J Orthop Res, 2016. 34(3): p. 369-85.

3. Szost, B.A., et al., A comparative study of additive manufacturing techniques: Residual stress and microstructural analysis of CLAD and WAAM printed Ti-6Al-4V components. Materials & Design, 2016. 89: p. 559-567.

4. Lyczkowska, E., et al., Chemical polishing of scaffolds made of Ti-6Al-7Nb alloy by additive manufacturing. Archives of Civil and Mechanical Engineering, 2014. 14(4): p. 586-594.

5. Ma, C.P., Y.C. Guan, and W. Zhou, Laser polishing of additive manufactured Ti alloys. Optics and Lasers in Engineering, 2017. 93: p. 171-177.

6. Ezugwu, E.O. and Z.M. Wang, Titanium alloys and their machinability—a review. Journal of Materials Processing Technology, 1997. 68(3): p. 262-274.

7. Wahab, J.A., et al., Enhancing material performance through laser surface texturing: a review. Transactions of the Institute of Metal Finishing, 2016. 94(4): p. 193-198.

8. Shah, F.A., et al., Laser-Modified Surface Enhances Osseointegration and Biomechanical Anchorage of Commercially Pure Titanium Implants for Bone-Anchored Hearing Systems. Plos One, 2016. 11(6).

9. Mariscal-Munoz, E., et al., Osteoblast differentiation is enhanced by a nano-to-micro hybrid titanium surface created by Yb:YAG laser irradiation. Clinical Oral Investigations, 2016. 20(3): p. 503-511.

10. Sipe, J.E., et al., Laser-Induced Periodic Surface-Structure .1. Theory. Physical Review B, 1983. 27(2): p. 1141-1154.

11. Villerius, V., et al., Ultrashort pulsed laser ablation of stainless steels. International Journal of Machine Tools and Manufacture, 2019. 138: p. 27-35.

12. Lee, B.E.J., et al., Characterization and evaluation of femtosecond laser-induced sub-micron periodic structures generated on titanium to improve osseointegration of implants. Applied Surface Science, 2018. 441: p. 1034-1042.

13. Cunha, A., et al., Human mesenchymal stem cell behavior on femtosecond laser-textured Ti-6Al-4V surfaces. Nanomedicine, 2015. 10(5): p. 725-739.

14. Batal, A., et al., Effects of laser processing conditions on wettability and proliferation of Saos-2 cells on CoCrMo alloy surfaces, in Advanced Optical Technologies. 2019.

15. Bhaduri, D., et al., Laser polishing of 3D printed mesoscale components. Applied Surface Science, 2017. 405: p. 29-46.

16. Marimuthu, S., et al., Laser polishing of selective laser melted components. International Journal of Machine Tools & Manufacture, 2015. 95: p. 97-104.

17. Karoussis, I.K., et al., Nd:YAG laser radiation (1.064 nm) accelerates differentiation of osteoblasts to osteocytes on smooth and rough titanium surfaces in vitro. Clin Oral Implants Res, 2017. 28(7): p. 785-790.

18. Yung, K.C., et al., Laser polishing of additive manufactured CoCr alloy components with complex surface geometry. Journal of Materials Processing Technology, 2018. 262: p. 53-64.

19. Cuccolini, G., L. Orazi, and A. Fortunato, 5 Axes computer aided laser milling. Optics and Lasers in Engineering, 2013. 51(6): p. 749-760.

20. Jiang, M., et al., Large scale layering laser surface texturing system based on high speed optical scanners and gantry machine tool. Robotics and Computer-Integrated Manufacturing, 2017. 48: p. 113-120.

21. Diaci, J., et al., Rapid and flexible laser marking and engraving of tilted and curved surfaces. Optics and Lasers in Engineering, 2011. 49(2): p. 195-199.

22. Wang, X.Z., et al., Study of laser precision ablating texture patterns on large-scale freeform surface. International Journal of Advanced Manufacturing Technology, 2017. 92(9-12): p. 4571-4581.

23. Stroud, I. and P.C. Xirouchakis, STL and extensions. Advances in Engineering Software, 2000. 31(2): p. 83-95.

24. Dimitrov, D., et al., Investigating the achievable accuracy of three dimensional printing. Rapid Prototyping Journal, 2006. 12(1): p. 42-52.

25. Giorleo, L., E. Ceretti, and C. Giardini, Ti surface laser polishing: effect of laser path and assist gas. 9th Cirp Conference on Intelligent Computation in Manufacturing Engineering - Cirp Icme '14, 2015. 33: p. 446-451.

26. Wenninger, M.J., Spherical models. 1979, Cambridge Eng. ; New York: Cambridge University Press. xii, 147 p.

27. Meschede, D., Optics, Light, and Lasers: The Practical Approach to Modern Aspects of Photonics and Laser Physics. Optics, Light, and Lasers: The Practical Approach to Modern Aspects of Photonics and Laser Physics, 2017: p. 1-528.

28. Overmeyer, L., et al., Laser patterning of thin film sensors on 3-D surfaces. Cirp Annals-Manufacturing Technology, 2012. 61(1): p. 215-218.

29. Penchev, P., et al., Generic software tool for counteracting the dynamics effects of optical beam delivery systems. Proceedings of the Institution of Mechanical Engineers Part B-Journal of Engineering Manufacture, 2017. 231(1): p. 48-64.

30. Reif, J., O. Varlamova, and F. Costache, Femtosecond laser induced nanostructure formation: self-organization control parameters. Applied Physics a-Materials Science & Processing, 2008. 92(4): p. 1019-1024.

31. Prokhorov, A.M., et al., Excitation and Resonant Transformation of a Surface Electromagnetic Wave during Irradiation of a Solid by High-Power Laser Radiation. Kvantovaya Elektronika, 1983. 10(5): p. 906-912.

32. Deng, T., J. Li, and Z. Zheng, Fundamental aspects and recent developments in metal surface polishing with energy beam irradiation. International Journal of Machine Tools and Manufacture, 2020. 148: p. 103472.

CHAPTER 6: CONTRIBUTIONS, CONCLUSIONS AND FUTURE RESEARCH

This chapter summarises the main conclusions and contributions to knowledge claimed in this research. Furthermore, future steps and research directions are discussed in the chapter.

6.1 Conclusions

1. Saos-2 cell adhesion occurred on all the CoCr surfaces and the surface topography was an important factor governing both cell morphology and proliferation.

2. A higher roughness encourages initial cone-like cell adhesion however smoother/planner surfaces facilitate cell proliferation.

3. The highest Saos-2 cell metabolic activity occurred on Day 7 on the NT surface, as shown by the MTT assay. This can be attributed to both the anchoring effects of the sub-micron textures and also the high proliferation levels of smooth surfaces. In addition, the cells on the NT samples that had bio-inspired sub-micron topography did not show any signs of directionality.

4. Surface topography is a more significant factor than surface energy in Saos-2 cell attachment and proliferation. Controlling the micron (cell size) and sub-micron scales of implant surfaces could lead to much improved biological responses.

5. Correlation between CA and cell proliferation is only valid when both the wetting behaviours and surface roughness values are comparable.

6. Long lasting super hydrophilic, 0˚ CA, surfaces can be produced via ultrashort pulsed laser structuring, namely by producing micro grooves with hierarchical micro/nano topography at the bottom, FS samples.

7. Saos-2 cells grew in the micro-grooves produced with the longer 220ns laser pulses but not in the ones produced with the ultrashort pulses, in fact the FS grooves inhibited cell attachment and growth. This suggests that the self-organized hierarchical micro/nano structures found in the FS grooves could be used to potentially control cell migration.

8. In general, the LIPSS treatments enhanced the Saos-2 cells proliferation on the CoCrMo disks while their wettability decreased.

9. Irrespective of initial surface roughness there were substantial improvements in Saos-2 cells proliferation.

10. The biological response of laser-processed biomaterials is more sensitive to BIA changes compared with the effects of FOD variations, i.e. Saos-2 cells were more affected by changes in the periodicity of the sub-micron ripples rather than their depth

11. The biological performance of biomaterials can be correlated to their wettability when the surfaces are chemically and topographically comparable.

12. Geometrical tolerances can be set for partitioning 3D parts by investigating the effects of laser processing disturbances, i.e. those present in performing LP and LST operations, and thus to polish and texture large 3D surfaces consistently and uniformly.

13. 3D printed components, i.e. LPBF Ti-6Al-4V parts, can be successfully laser polished and the resulting surface roughness is sufficient, <500 nm, for performing

sub-micron uniformed texturing, in particular for covering large 3D surface areas with LIPSS.

14. Laser polishing and texturing results over 3D surfaces can be impacted negatively by the varying FOD and BIA, especially leading to higher surface roughness values; it was found that 3D printed Ti-6Al-4V parts can be polished satisfactorily, i.e. with surface roughness (Sa) below 0.5 µm, by keeping FOD deviations and BIA below 0.5 mm and 40˚, respectively.

15. The uniformity of LP operations over large surface areas can be improved by introducing a controlled overlapping between the polishing fields and thus to minimise the negative effects at their borders, e.g. the formation of micro-scale trenches and surface cracks.

16. Geodesic-inspired partitioning of spherical surfaces can be used to represent them with a smaller number of triangles compared with those generated by common triangulation algorithms, e.g. for creating STL files; also, such surface representations include less different triangular shapes that can lead to a more efficient and consistent laser processing.

6.2 Contributions

The aim of this research was to investigate the capabilities and limitations of laser surface modification processes when applied on biomaterials for orthopaedics applications. More specifically, this approach was systematically studied and compared against competing technologies. Its limitations were quantified when it was applied on complex parts and a generic solution for its implementation was proposed and validated. The biological and wetting properties achievable on CoCrMo substrates

with 3 different LST methods were investigated in **Chapter 3** and compared with those obtainable by polishing, blasting and HA coating. Next, the effects of 3D processing disturbances in generating LIPSS on CoCrMo alloy on their morphologies and functionality were investigated and quantified in **Chapter 4.** Finally, a generic method for laser processing complex surface by partitioning them in fields was proposed and its pilot application demonstrated on additively manufactured spherical Ti-6Al-4V shells in **Chapter 5**.

The main objectives of this PhD research were achieved and the contributions to knowledge claimed in this thesis are as follows:

i. Investigate the biological (Saos-2 cells proliferation) and wetting properties of LST surfaces and compare them with those achievable after polishing, blasting and hydroxyapatite (HA) coating when applied on a surgical cobalt chromium molybdenum alloy (CoCrMo).

Three different LST strategies for improving the biocompatibility of a surgical cobalt chromium molybdenum alloy were proposed. A synergetic combination of different LST approaches was recommended, potentially bypassing the current need for not environmentally friendly and expensive coatings. The performance of the investigated LST strategies was assessed by measuring the metabolic activity of Saos-2 osteoblast-like cells on CoCrMo alloy disks and comparing it with that on commercial HA coating. These are the main findings from the conducted research (**Chapter 3)**:

- Micro-scale textures and higher surface roughness encouraged initial cell anchorage/adhesion, whereas smoother surfaces promoted cell growth and proliferation.
- The highest metabolic activity was achieved on Day 7 on the sub-micron textured surface. This was attributed to both the anchoring effects of the sub-micron textures as well as the ease in which cells proliferated on smooth surfaces. In addition, the cells on the NT samples that had a bio-inspired sub-micron topography did not show any signs of directionality.

ii. *Investigate the influence of 3D processing disturbances on the resulting surface topography and functionality of sub-micron LST patterns on CoCrMo substrates.*

A systematic method for investigating the impact of 3D processing disturbances, i.e. Focal Offset Distance (FOD) and Beam Incedent Angle (BIA), on sub-micron topographies of laser textured surfaces and also on their functional response was proposed. A pilot implementation of this method was carried out by analysing the the effects of these disturbances on the biological and wetting properties of CoCrMo alloy disks. The main findings of this pilot implementation were (**Chapter 4)**:

- The LIPSS treatment improved the biological response of the CoCrMo disks irrespective of the initial surface quality.
- FOD and BIA variations affected the biological response of the treated surface negatively. This was evident from the reduced metabolic activities of the Saos-

2 cells when compared with those obtained on samples processed in-focus and with normal BIA to the substrates.

- A correlation between surface wettability and cell growth and proliferation was observed on the laser treated disks. Such correlation was not observed on unstructured/untreated surfaces.

iii. *Develop a generic methodology for applying laser surface modifications, e.g. LST and LP operations, on complex parts and freeform surfaces.*

A novel method for laser processing freeform surfaces was developed. The method takes into account the limitations of 3D laser processing when partitioning freeform surfaces and thus to ensure processing uniformity over 3D parts. In a pilot study the method was implemented for polishing and texturing 3D printed spherical Ti-6Al-4V shells **(Chapter 5)** and these were the main findings:

- 3D printed components produced by Laser Powder Bed Fusion can be polished with a pulsed NIR fibre laser to a surface finish level that is sufficient for subsequent sub-micron texturing using a fs laser source.
- FOD and BIA variations affected negatively the laser polishing performance on 3D printed Ti-6Al-4V parts.
- Overlapping of LP fields can alleviate some of the stitching marks left after the polishing operation on large surface areas.
- Geodesic polyhedra can serve as an efficient partitioning method for spherical surfaces, yielding a smaller number of triangular fields than common STL

algorithms. Furthermore, the triangular fields are more homogeneous and this translate to a more uniform laser processing.

6.3 Future research

- Further in-vitro assessments of the LST effects on the biological response of CoCrMo alloys are required as most of the research reported so far is focused on titanium alloys. In particular, fluorescence microscopy could better visualise fibroblast morphology on laser treated samples while osteogenic differentiation could give indications of any enhanced bone formation on laser treated surfaces.
- Biomechanical modelling of osteoblast cells' interaction with the micro-environment around them can lead to optimized micro-topographies for a better anchorage and proliferation, and thus to reduce the need for trial and error optimisation studies.
- A correlation between surface wettability and cell proliferation was identified in **Chapter 4.** However, it was observed that this correlation was depended on surface topography. Identifying and understanding the limits of these interdependences would determine how wettability can be used to judge indirectly about cellular activities on laser treated surfaces.
- Functional characterisation of laser treated freeform surfaces is required to better assess the transferability of obtained functionalities planar samples to real 3D parts. Some LST 'recipes' can be applied to 3D parts by employing different laser processing strategies and thus it will be possible to investigate the capabilities and limitations of those 3D processing approaches (productivity, functional performance, etc.) and the resulting surface properties compared.

- Investigate other approaches for improving the stitching quality between the triangular fields on complex surfaces, namely to eliminate the polishing-induced cracks. For example, randomizing the overlap between scanning vectors and their position in the joining area, in order to mask their presence. Another potential solution could be to tune the laser parameters near the edge of laser polishing fields in order to reduce thermal stresses.
- While the combined effect of FOD and BIA present in 3D laser processing could be measured empirically for a given laser task, greatly increasing the number of initial experiments, modelling the beam energy distribution over the 3D part could potentially help better understand and quantify its effects before tessellating the surface accordingly.

Appendix 5.1

MATLAB Code

```
clear all
clc
close all

prompt = 'Please specify the sphere radius in mm: ';
r=input(prompt);
prompt = 'What is the laser process focal offset tolerance in mm: ';
fod=input (prompt);
prompt = 'What is the laser process incident angle tolerance in degrees: ';
bia=input(prompt);
bia=bia*pi/180;

%%Check Icosahedral arrangement

ico=r/sin(2*pi/5); %%First frequency side
hico=ico*sqrt(3)/2; %%First frequency height
ti1=ico;
ti2=ico;
hti1=hico;
hti2=hti1;
bti=ico;
ni=20; %%First frequency number of triangles
dihico=acos(-sqrt(5)/3);
 if hti1>=hti2
    yorthi=(2/3)*hti1-((1/(2*hti1))*(bti^2/4+hti1^2));
    hci=r-sqrt(r^2-(2*(2/3*hti1-yorthi))^2/4);
    hangi=(2/3)*hti1-yorthi;
    else
    yorthi=(2/3)*hti2-((1/(2*hti2))*(bti^2/4+hti2^2));
    hci=r-sqrt(r^2-(2*(2/3*hti2-yorthi))^2/4);
    hangi=(2/3)*hti2-yorthi;
    end

for i=1:2

    if hci<=2*fod && atan(hci/hangi)<=bia
        break
    end

    if i==1
        a=2/3*hico;
        b=r^2-a^2;
        c=sqrt(b);
        hti1=(3/2)*r*cos(dihico/2);
```

```
    d=hti1/3;
    e=sqrt(c^2+d^2);
    f=(1/3)*hico*tan(dihico/2);
    g=e*f/c;
    h=f/g;
    ii=asin(h);
    j=e-g;
    k=0.5*hico;
    hti2=sqrt(j^2+k^2-2*j*k*cos(ii));
    ti1=hti1/sin(1.047197551);
    bti=ti1;
    ti2=sqrt(bti^2/4+hti2^2);
    ni=20*(i+1)^2;
     if hti1>=hti2
yorthi=(2/3)*hti1-((1/(2*hti1))*(bti^2/4+hti1^2));
hci=r-sqrt(r^2-(2*(2/3*hti1-yorthi))^2/4);
hangi=(2/3)*hti1-yorthi;
else
yorthi=(2/3)*hti2-((1/(2*hti2))*(bti^2/4+hti2^2));
hci=r-sqrt(r^2-(2*(2/3*hti2-yorthi))^2/4);
hangi=(2/3)*hti2-yorthi;
end
end
if i==2
    a=1/3*hico;
    b=1/3*ico;
    c=ico/2/r;
    d=acos(c);
    e=sqrt(r^2+b^2-2*r*b*c);
    bti=r*b/e;
    f=b/2/e;
    g=acos(f);
    h=r-e;
    ti1=sqrt(h^2+b^2-2*h*b*f);
    hti1=sqrt(ti1^2-bti^2/4);
    ii=a/cos(dihico/2);
    j=sqrt(ii^2-a^2);
    k=j/ii;
    l=acos(k);
    m=(a^2+ii^2-r^2)/(2*a*ii);
    n=acos(m);
    o=pi-n;
    p=sin(o)*a/hti1;
    q=asin(p);
    rr=pi-q-o;
    s=sin(rr)*hti1/sin(o);
    hti2=sqrt(r^2+(ii+s)^2-2*r*(ii+s)*k);
    ti2=sqrt(hti2^2+bti^2/4);
```

```
      ni=20*(i+1)^2;
       if hti1>=hti2
   yorthi=(2/3)*hti1-((1/(2*hti1))*(bti^2/4+hti1^2));
   hci=r-sqrt(r^2-(2*(2/3*hti1-yorthi))^2/4);
   hangi=(2/3)*hti1-yorthi;
   else
   yorthi=(2/3)*hti2-((1/(2*hti2))*(bti^2/4+hti2^2));
   hci=r-sqrt(r^2-(2*(2/3*hti2-yorthi))^2/4);
   hangi=(2/3)*hti2-yorthi;
   end
   end
end

%%Check Octahedral arrangement

oct=2*r/sqrt(2); %%First frequency side
hoct=oct*sqrt(3)/2; %%First frequency height
to1=oct;
to2=to1;
hto1=hoct;
hto2=hto1;
bto=oct;
no=8; %%First frequency number of triangles
dihoct=acos(-1/3);
 if hto1>=hto2
   yortho=(2/3)*hto1-((1/(2*hto1))*(bto^2/4+hto1^2));
   hco=r-sqrt(r^2-(2*(2/3*hto1-yortho))^2/4);
   hango=(2/3)*hto1-yortho;
   else
   yortho=(2/3)*hto2-((1/(2*hto2))*(bto^2/4+hto2^2));
   hco=r-sqrt(r^2-(2*(2/3*hto2-yortho))^2/4);
   hango=(2/3)*hto2-yortho;
   end

for i=1:2

   if hco<=2*fod && atan(hco/hango)<=bia
      break
   end

   if i==1
      hto1=(3/2)*r*cos(dihoct/2);
      to1=hto1/sin(1.047197551);
      bto=to1;
      a=(r/2)/hto1;
      b=asin(a);
      c=2*b;
      d=hoct/2;
```

```
        e=hto1-d;
        f=hoct/2;
        hto2=sqrt(e^2+f^2-2*e*f*cos(c));
        to2=sqrt((bto^2/4)+hto2^2);
        no=8*(i+1)^2;
         if hto1>=hto2
    yortho=(2/3)*hto1-((1/(2*hto1))*(bto^2/4+hto1^2));
    hco=r-sqrt(r^2-(2*(2/3*hto1-yortho))^2/4);
    hango=(2/3)*hto1-yortho;
    else
    yortho=(2/3)*hto2-((1/(2*hto2))*(bto^2/4+hto2^2));
    hco=r-sqrt(r^2-(2*(2/3*hto2-yortho))^2/4);
    hango=(2/3)*hto2-yortho;
    end
    end

    if  i==2
        a=1/3*oct;
        b=45*pi/180;
        c=sqrt(r^2+a^2-2*r*a*cos(b));
        bto=r*a/c;
        d=(oct/6)/c;
        e=acos(d);
        f=r-c;
        to1=sqrt(f^2+a^2-2*f*a*d);
        hto1=sqrt(to1^2-bto^2/4);
        g=hoct/3*sin(dihoct/2)/hto1;
        h=asin(g);
        ii=pi-h-dihoct/2;
        j=hoct/3*sin(ii)/g;
        k=pi/2-dihoct/2;
        hto2=sqrt(r^2+(0.5*oct+j)^2-2*r*(0.5*oct+j)*cos(k));
        to2=sqrt(hto2^2+bto^2/4);
        no=8*(i+1)^2;
         if hto1>=hto2
    yortho=(2/3)*hto1-((1/(2*hto1))*(bto^2/4+hto1^2));
    hco=r-sqrt(r^2-(2*(2/3*hto1-yortho))^2/4);
    hango=(2/3)*hto1-yortho;
    else
    yortho=(2/3)*hto2-((1/(2*hto2))*(bto^2/4+hto2^2));
    hco=r-sqrt(r^2-(2*(2/3*hto2-yortho))^2/4);
    hango=(2/3)*hto2-yortho;
    end
    end
end

%%Check Tetrahedral arrangement
```

```
tet=4*r/sqrt(6); %%First frequency side
htet=tet*sqrt(3)/2; %%First frequency height
tt1=tet;
tt2=tt1;
htt1=htet;
htt2=htt1;
btt=tet;
nt=3; %%First frequency number of triangles
dihtet=acos(1/3);
if htt1>=htt2
    yortht=(2/3)*htt1-((1/(2*htt1))*(btt^2/4+htt1^2));
    hct=r-sqrt(r^2-(2*(2/3*htt1-yortht))^2/4);
    hangt=(2/3)*htt1-yortht;
    else
    yortht=(2/3)*htt2-((1/(2*htt2))*(btt^2/4+htt2^2));
    hct=r-sqrt(r^2-(2*(2/3*htt2-yortht))^2/4);
    hangt=(2/3)*htt2-yortht;
    end

for i=1:2



    if hct<=2*fod && atan(hct/hangt)<=bia
        break
    end

    if i==1
        htt1=(3/2)*r*cos(dihtet/2);
        tt1=htt1/sin(1.047197551);
        btt=tt1;
        a=sqrt(htt1^2-r^2);
        b=r/htt1;
        c=asin(b);
        d=a*0.5*htet/htt1;
        e=a-d;
        f=htet/2;
        htt2=sqrt(e^2+f^2-2*e*f*cos(c));
        tt2=sqrt((btt^2/4)+htt2^2);
        nt=4*(i+1)^2;
        if htt1>=htt2
    yortht=(2/3)*htt1-((1/(2*htt1))*(btt^2/4+htt1^2));
    hct=r-sqrt(r^2-(2*(2/3*htt1-yortht))^2/4);
    hangt=(2/3)*htt1-yortht;
    else
    yortht=(2/3)*htt2-((1/(2*htt2))*(btt^2/4+htt2^2));
    hct=r-sqrt(r^2-(2*(2/3*htt2-yortht))^2/4);
    hangt=(2/3)*htt2-yortht;
```

```
    end
    end
    if i==2
        a=sqrt(htet^2-0.25*tet^2);
        b=sqrt((0.5*a)^2+(1/6*tet)^2);
        btt=(r*1/3*tet)/b;
        c=0.5*a/b;
        d=asin(c);
        tt1=sqrt((r-b)^2+(1/3*tet)^2-2*(r-b)*(1/3*tet)*cos(d));
        htt1=sqrt(tt1^2-0.25*btt^2);
        e=(1/3)*r/(0.5*a);
        f=asin(e);
        g=htet/3*e/htt1;
        h=pi-asin(g);
        ii=pi-h-f;
        j=htt1*sin(ii)/e;
        k=(0.5*a+j)*cos(f);
        l=k*tan(f)-(1/3)*r;
        m=r-l-r/3;
        htt2=sqrt(m^2+k^2);
        tt2=sqrt(htt2^2+btt^2/4);
        nt=4*(i+1)^2;
        if htt1>=htt2
    yortht=(2/3)*htt1-((1/(2*htt1))*(btt^2/4+htt1^2));
    hct=r-sqrt(r^2-(2*(2/3*htt1-yortht))^2/4);
    hangt=(2/3)*htt1-yortht;
    else
    yortht=(2/3)*htt2-((1/(2*htt2))*(btt^2/4+htt2^2));
    hct=r-sqrt(r^2-(2*(2/3*htt2-yortht))^2/4);
    hangt=(2/3)*htt2-yortht;
    end
    end
end

%%Choose the arrangement with the smallest number of patches

if  hci<=2*fod && atan(hci/hangi)<=bia
    t1=ti1;
    t2=ti2;
    ht1=hti1;
    ht2=hti2;
    bt=bti;
    arr='Icosahedral';
    n=ni;
    dih=acos(-sqrt(5)/3)*180/pi;
end
if  hco<=2*fod && atan(hco/hango)<=bia && no<ni
    t1=to1;
```

```
    t2=to2;
    ht1=hto1;
    ht2=hto2;
    bt=bto;
    arr='Octahedral';
    n=no;
    dih=acos(-1/3)*180/pi;
end
if  hct<=2*fod && atan(hct/hangt)<=bia && nt<no
    t1=tt1;
    t2=tt2;
    ht1=htt1;
    ht2=htt2;
    bt=btt;
    arr='Tetrahedral';
    n=nt;
    dih=acos(1/3)*180/pi;
end

    if hci>2*fod || atan(hci/hangi)>bia
       disp 'The laser processing tolerances are too small'
    return
    end

%%TRIANGLE 1

%%line1
x1=(-bt/2:0.01:bt/2);
x1(end)=bt/2;
y1=ones(size(x1))*-1/3*ht1;

%%line2
x2=(0:0.005:bt/2);
x2 (end)=bt/2;
y2=(-2*ht1/bt)*x2+(2/3*ht1);
y2(end)=-1/3*ht1;

%%line3
x3=(-bt/2:0.005:0);
x3(end)=0;
y3=(2*ht1/bt)*x3+(2/3*ht1);
y3(end)=2/3*ht1;

%%Find coordinates of CIRCUMCENTRE
%%Distance from vertice
dcircum1=(1/(2*ht1))*(bt^2/4+ht1^2);
yorth1=(2/3)*ht1-dcircum1;
```

```
%%Altitude above triangle

hc1=r-sqrt(r^2-(2*(2/3*ht1-yorth1))^2/4);

%%TRIANGLE 2

%%line1
ix1=(-bt/2:0.01:bt/2);
ix1(end)=bt/2;
iy1=ones(size(x1))*-1/3*ht2;

%%line2
ix2=(0:0.005:bt/2);
ix2 (end)=bt/2;
iy2=(-2*ht2/bt)*x2+(2/3*ht2);
iy2(end)=-1/3*ht2;

%%line3
ix3=(-bt/2:0.005:0);
ix3(end)=0;
iy3=(2*ht2/bt)*x3+(2/3*ht2);
iy3(end)=2/3*ht2;

%%Find coordinates of CIRCUMCENTRE
dcircum2=(1/(2*ht2))*(bt^2/4+ht2^2);
yorth2=(2/3)*ht2-dcircum2;

%%Altitude above triangle

hc2=r-sqrt(r^2-(2*((2/3)*ht2-yorth2))^2/4);

%%Distortion Triangle 1

%%Distance circumcenter to line 1
lx1=length(x1);
if rem(lx1,2)==0
dl1=sqrt(x1(lx1/2)^2+(y1(lx1/2)-yorth1)^2);
else
   dl1=sqrt(x1(lx1/2+0.5)^2+(y1(lx1/2+0.5)-yorth1)^2);
end

%%Distance circumcenter to line 2
lx2=length(x2);
if rem(lx2,2)==0
dl2=sqrt(x2(lx2/2)^2+(y2(lx2/2)-yorth1)^2);
else
   dl2=sqrt(x2(lx2/2+0.5)^2+(y2(lx2/2+0.5)-yorth1)^2);
end
```

```
%%Distance circumcenter to line 3
lx3=length(x3);
if rem(lx3,2)==0
dl3=sqrt(x3(lx3/2)^2+(y3(lx3/2)-yorth1)^2);
else
   dl3=sqrt(x3(lx3/2+0.5)^2+(y3(lx3/2+0.5)-yorth1)^2);
end

%%Arc 1
ha1=hc1*dl1/(r-hc1);
ra1=ha1/2+bt^2/(8*ha1);
syms xc1 yc1
sht1=sym(ht1);
sra1=sym(ra1);
sbt=sym(bt);
equations = [ (-0.5*sbt-xc1)^2+(-1/3*sht1-yc1)^2==sra1^2 , (0.5*sbt-xc1)^2+(-
1/3*sht1-yc1)^2==sra1^2];
answers = [xc1 yc1];
sol1 = solve(equations, answers);
%%sol1.xc1, sol1.yc1
xc1=0;
if sol1.yc1(1)>-1/3*ht1
   yc1=double(sol1.yc1(1));
else
   yc1=double(sol1.yc1(2));
end

for i=1:length(x1)
yarc1(i)=-sqrt(ra1^2-(x1(i)-xc1).^2)+yc1;
end

%%Arc 2
ha2=hc1*dl2/(r-hc1);
ra2=ha2/2+t1^2/(8*ha2);
syms xc2 yc2
sht1=sym(ht1);
sra2=sym(ra2);
sbt=sym(bt);
equations = [ xc2^2+(2/3*sht1-yc2)^2==sra2^2 , (0.5*sbt-xc2)^2+(-1/3*sht1-
yc2)^2==sra2^2];
answers = [xc2 yc2];
sol2 = solve(equations, answers);
%%sol2.xc2, sol2.yc2
if sol2.xc2(1)>sol2.xc2(2)
   xc2=double(sol2.xc2(2));
else
   xc2=double(sol2.xc2(1));
```

```
end
if sol2.yc2(1)>sol2.yc2(2)
    yc2=double(sol2.yc2(2));
else
    yc2=double(sol2.yc2(1));
end

if yc2<0
ang2=asin((-(1/3)*ht1-yc2)/ra2):0.01:asin(((2/3)*ht1-yc2)/ra2);
else
ang2=asin((-(1/3)*ht1-yc2)/ra2):0.01:pi-asin(((2/3)*ht1-yc2)/ra2);
end
xarc2=ra2*cos(ang2);
xarc2=xarc2+xc2;
xarc2(1)=bt/2;
xarc2(end)=0;
yarc2=ra2*sin(ang2);
yarc2=yarc2+yc2;
yarc2(1)=-1/3*ht1;
yarc2(end)=2/3*ht1;


%%Arc 3
ha3=hc1*dl3/(r-hc1);
ra3=ha3/2+t1^2/(8*ha3);
syms xc3 yc3
sht1=sym(ht1);
sra3=sym(ra3);
sbt=sym(bt);
equations = [ xc3^2+(2/3*sht1-yc3)^2==sra3^2 , (-0.5*sbt-xc3)^2+(-1/3*sht1-
yc3)^2==sra3^2];
answers = [xc3 yc3];
sol3 = solve(equations, answers);
%%sol3.xc3, sol3.yc3
if sol3.xc3(1)>sol3.xc3(2)
    xc3=double(sol3.xc3(1));
else
    xc3=double(sol3.xc3(2));
end
if sol3.yc3(1)>sol3.yc3(2)
    yc3=double(sol3.yc3(2));
else
    yc3=double(sol3.yc3(1));
end

ang3=acos((-xc3)/(ra3)):0.01:pi-asin((-(1/3)*ht1-yc3)/ra3);
xarc3=ra3*cos(ang3);
xarc3=xarc3+xc3;
```

```
xarc3(end)=-bt/2;
xarc3(1)=0;
yarc3=ra3*sin(ang3);
yarc3=yarc3+yc3;
yarc3(end)=-1/3*ht1;
yarc3(1)=2/3*ht1;

%Distortion Triangle 2

%Distance circumcenter to line 1
lx1=length(ix1);
if rem(lx1,2)==0
dl1=sqrt(ix1(lx1/2)^2+(iy1(lx1/2)-yorth2)^2);
else
   dl1=sqrt(ix1(lx1/2+0.5)^2+(iy1(lx1/2+0.5)-yorth2)^2);
end

%Distance circumcenter to line 2
lx2=length(ix2);
if rem(lx2,2)==0
dl2=sqrt(ix2(lx2/2)^2+(iy2(lx2/2)-yorth2)^2);
else
   dl2=sqrt(ix2(lx2/2+0.5)^2+(iy2(lx2/2+0.5)-yorth2)^2);
end

%Distance circumcenter to line 3
lx3=length(ix3);
if rem(lx3,2)==0
dl3=sqrt(ix3(lx3/2)^2+(iy3(lx3/2)-yorth2)^2);
else
   dl3=sqrt(ix3(lx3/2+0.5)^2+(iy3(lx3/2+0.5)-yorth2)^2);
end

%Arc 1
ha1=hc2*dl1/(r-hc2);
ra1=ha1/2+bt^2/(8*ha1);
syms ixc1 iyc1
sht2=sym(ht2);
sra1=sym(ra1);
sbt=sym(bt);
equations = [ (-0.5*sbt-ixc1)^2+(-1/3*sht2-iyc1)^2==sra1^2 , (0.5*sbt-ixc1)^2+(-
1/3*sht2-iyc1)^2==sra1^2];
answers = [ixc1 iyc1];
sol1 = solve(equations, answers);
%sol1.ixc1, sol1.iyc1
ixc1=0;
if sol1.iyc1(1)>-1/3*ht2
   iyc1=double(sol1.iyc1(1));
```

```
else
    iyc1=double(sol1.iyc1(2));
end

for i=1:length(ix1)
iyarc1(i)=-sqrt(ra1^2-(ix1(i)-ixc1).^2)+iyc1;
end

%Arc 2
ha2=hc2*dl2/(r-hc2);
ra2=ha2/2+t2^2/(8*ha2);
syms ixc2 iyc2
sht2=sym(ht2);
sra2=sym(ra2);
sbt=sym(bt);
equations = [ ixc2^2+(2/3*sht2-iyc2)^2==sra2^2 , (0.5*sbt-ixc2)^2+(-1/3*sht2-
iyc2)^2==sra2^2];
answers = [ixc2 iyc2];
sol2 = solve(equations, answers);
%sol2.ixc2, sol2.iyc2
if sol2.ixc2(1)>sol2.ixc2(2)
    ixc2=double(sol2.ixc2(2));
else
    ixc2=double(sol2.ixc2(1));
end
if sol2.iyc2(1)>sol2.iyc2(2)
    iyc2=double(sol2.iyc2(2));
else
    iyc2=double(sol2.iyc2(1));
end

if iyc2<0
ang2=asin((-(1/3)*ht2-iyc2)/ra2):0.01:asin(((2/3)*ht2-iyc2)/ra2);
else
ang2=asin((-(1/3)*ht2-iyc2)/ra2):0.01:pi-asin(((2/3)*ht2-iyc2)/ra2);
end
ixarc2=ra2*cos(ang2);
ixarc2=ixarc2+ixc2;
ixarc2(1)=bt/2;
ixarc2(end)=0;
iyarc2=ra2*sin(ang2);
iyarc2=iyarc2+iyc2;
iyarc2(1)=-1/3*ht2;
iyarc2(end)=2/3*ht2;

%Arc 3
ha3=hc2*dl3/(r-hc2);
ra3=ha3/2+t2^2/(8*ha3);
```

```
syms ixc3 iyc3
sht2=sym(ht2);
sra3=sym(ra3);
sbt=sym(bt);
equations = [ ixc3^2+(2/3*sht2-iyc3)^2==sra3^2 , (-0.5*sbt-ixc3)^2+(-1/3*sht2-
iyc3)^2==sra3^2];
answers = [ixc3 iyc3];
sol3 = solve(equations, answers);
%sol3.ixc3, sol3.iyc3
if sol3.ixc3(1)>sol3.ixc3(2)
   ixc3=double(sol3.ixc3(1));
else
   ixc3=double(sol3.ixc3(2));
end
if sol3.iyc3(1)>sol3.iyc3(2)
   iyc3=double(sol3.iyc3(2));
else
   iyc3=double(sol3.iyc3(1));
end

ang3=acos((-ixc3)/(ra3)):0.01:pi-asin((-(1/3)*ht2-iyc3)/ra3);
ixarc3=ra3*cos(ang3);
ixarc3=ixarc3+ixc3;
ixarc3(end)=-bt/2;
ixarc3(1)=0;
iyarc3=ra3*sin(ang3);
iyarc3=iyarc3+iyc3;
iyarc3(end)=-1/3*ht2;
iyarc3(1)=2/3*ht2;

%OUTPUTS

fprintf('\n')
disp 'The size of Triangle1 is:'
t1
ht1
bt
disp 'The size of Triangle2 is:'
t2
ht2
bt
disp 'The number of patches needed to process entire sphere is: '
fprintf('\n')
disp (n)
disp 'The distance between the circumcenter and half-height for normal Triangle1: '
fprintf('\n')
hh1=0.5*ht1-((1/3)*ht1-yorth1);
disp (hh1)
```

```
disp 'The distance between the circumcenter and half-height for normal Triangle2: '
fprintf('\n')
hh2=0.5*ht2-((1/3)*ht2-yorth2);
disp (hh2)
disp 'The distance between the circumcenter and half-height for distorted Triangle1: '
fprintf('\n')
dhh1=0.5*(ht1-min(yarc1))-(1/3)*ht1-yorth1;
disp (dhh1)
disp 'The distance between the circumcenter and half-height for distorted Triangle2: '
fprintf('\n')
dhh2=0.5*(ht2-min(iyarc1))-(1/3)*ht2-yorth2;
disp (dhh2)
disp 'The geometrical arrangement of the triangular laser patches is: '
fprintf('\n')
disp (arr)
fprintf('\n')
disp 'The dihedral angle for this arrangement is: '
fprintf('\n')
disp(dih)
disp 'The focal plane distance from the surface of the sphere (Triangle1) is: '
foci=hc1/2;
fprintf('\n')
disp (foci)
disp 'The focal plane distance from the surface of the sphere (Triangle2) is: '
foc=hc2/2;
fprintf('\n')
disp (foc)

%PLOTS

%Sphere

x=(-r:0.1:r);
y=sqrt(r^2-x.^2)-sqrt(r^2-t2^2/4);
f=0.5*(r-sqrt(r^2-t2^2/4));

figure('name','Sphere Patch Tolerances')
plot(x,y,'k')
hold on
plot(x,ones(size(x))*0,'b')
hold on
plot(x,ones(size(x))*f,'r')
hold on
plot(x,ones(size(x))*(f+fod),'--r')
hold on
plot(x,ones(size(x))*(f-fod),'--r')

%Triangle 1 and Distortion
```

```
figure('name','Triangle 1')

subplot(1,2,1)

plot(x1,y1,'k')
hold on
plot (x2,y2,'k')
hold on
plot(x3,y3,'k')


subplot(1,2,2)

plot(x1,y1,'k')
hold on
plot (x2,y2,'k')
hold on
plot(x3,y3,'k')
hold on
plot(x1,yarc1,'k')
hold on
plot (xarc2,yarc2,'k')
hold on
plot(xarc3,yarc3,'k')


%Triangle 2 and Distortion

figure('name','Triangle 2')

subplot(1,2,1)

plot(ix1,iy1,'k')
hold on
plot (ix2,iy2,'k')
hold on
plot(ix3,iy3,'k')


subplot(1,2,2)

plot(ix1,iy1,'k')
hold on
plot (ix2,iy2,'k')
hold on
plot(ix3,iy3,'k')
hold on
```

```
plot(ix1,iyarc1,'k')
hold on
plot (ixarc2,iyarc2,'k')
hold on
plot(ixarc3,iyarc3,'k')

prompt = 'Please specify an overlap percentage % if you wish: ';
over=input(prompt);
over=over/100;

%%Distances centroid T1

%%get distances between centroid and side1 and extend it
d1=(rand:length(x1));
for i=1:length(x1)
   d1(1,i)=sqrt((x1(1,i))^2+(yarc1(1,i))^2);
end
d1=d1*(1+over);

%%get distances between centroid and side2 and extend it
d2=(rand:length(xarc2));
for i=1:length(xarc2)
   d2(1,i)=sqrt((xarc2(1,i))^2+(yarc2(1,i))^2);
end
d2=d2*(1+over);

%%get distances between centroid and side3 and extend it
d3=(rand:length(xarc3));
for i=1:length(xarc3)
   d3(1,i)=sqrt((xarc3(1,i))^2+(yarc3(1,i))^2);
end
d3=d3*(1+over);

%%Distances centroid T2

%%get distances between centroid and side1 and extend it
id1=(rand:length(ix1));
for i=1:length(ix1)
   id1(1,i)=sqrt((ix1(1,i))^2+(iyarc1(1,i))^2);
end
id1=id1*(1+over);

%%get distances between centroid and side2 and extend it
id2=(rand:length(ixarc2));
for i=1:length(ixarc2)
   id2(1,i)=sqrt((ixarc2(1,i))^2+(iyarc2(1,i))^2);
end
id2=id2*(1+over);
```

```
%%get distances between centroid and side3 and extend it
id3=(rand:length(ixarc3));
for i=1:length(ixarc3)
   id3(1,i)=sqrt((ixarc3(1,i))^2+(iyarc3(1,i))^2);
end
id3=id3*(1+over);

%%New coordinates T1

%%solve polynomial for distorted coordinates of line1
rootx1=ones(2,length(d1));
rooty1=ones(2,length(d1));
for i=1:length(d1)
px1=[(1+yarc1(i)^2/(x1(i))^2) 0 (-d1(i)^2)];
rootx1(:,i)=roots(px1);
py1=[(1+x1(i)^2/yarc1(i)^2) 0 (-d1(i)^2)];
rooty1(:,i)=roots(py1);
end
dx1=ones(1,length(x1));
for i=1:length(rootx1)
   if x1(i)<=0
      dx1(i)=rootx1(2,i);
   else
      dx1(i)=rootx1(1,i);
   end
end
dy1=ones(1,length(yarc1));
for i=1:length(rooty1)
   if y1(i)<=0
      dy1(i)=rooty1(2,i);
   else
      dy1(i)=rooty1(1,i);
   end
end

%%solve polynomial for distorted coordinates of line2
rootx2=ones(2,length(d2));
rooty2=ones(2,length(d2));
for i=1:length(d2)
   px2=[(1+yarc2(i)^2/xarc2(i)^2) 0 (-d2(i)^2)];
   py2=[(1+xarc2(i)^2/yarc2(i)^2) 0 (-d2(i)^2)];
   if xarc2(i)==0
   rootx2(:,i)=[0;0];
   rooty2(:,i)=roots(py2);
   else
     rootx2(:,i)=roots(px2);
     rooty2(:,i)=roots(py2);
```

```
    end
end
dx2=ones(1,length(xarc2));
for i=1:length(rootx2)
    if xarc2(i)<=0
        dx2(i)=rootx2(2,i);
    else
        dx2(i)=rootx2(1,i);
    end
end
dy2=ones(1,length(yarc2));
for i=1:length(rooty2)
    if yarc2(i)<=0
        dy2(i)=rooty2(2,i);
    else
        dy2(i)=rooty2(1,i);
    end
end

%%solve polynomial for distorted coordinates of line3
rootx3=ones(2,length(d3));
rooty3=ones(2,length(d3));
for i=1:length(d3)
    px3=[(1+yarc3(i)^2/xarc3(i)^2) 0 (-d3(i)^2)];
    py3=[(1+xarc3(i)^2/yarc3(i)^2) 0 (-d3(i)^2)];
    if xarc3(i)==0
    rootx3(:,i)=[0;0];
    rooty3(:,i)=roots(py3);
    else
    rootx3(:,i)=roots(px3);
    rooty3(:,i)=roots(py3);
    end
end
dx3=ones(1,length(xarc3));
for i=1:length(rootx3)
    if xarc3(i)<=0
        dx3(i)=rootx3(2,i);
    else
        dx3(i)=rootx3(1,i);
    end
end
dy3=ones(1,length(yarc3));
for i=1:length(rooty3)
    if yarc3(i)<=0
        dy3(i)=rooty3(2,i);
    else
        dy3(i)=rooty3(1,i);
    end
```

```
end

%%New coordinates T2

%%solve polynomial for distorted coordinates of line1
irootix1=ones(2,length(id1));
irootiy1=ones(2,length(id1));
for i=1:length(id1)
pix1=[(1+iyarc1(i)^2/(ix1(i)+0.000001)^2) 0 (-id1(i)^2)];
irootix1(:,i)=roots(pix1);
piy1=[(1+ix1(i)^2/iyarc1(i)^2) 0 (-id1(i)^2)];
irootiy1(:,i)=roots(piy1);
end
dix1=ones(1,length(ix1));
for i=1:length(irootix1)
   if ix1(i)<=0
      dix1(i)=irootix1(2,i);
   else
      dix1(i)=irootix1(1,i);
   end
end
diy1=ones(1,length(iyarc1));
for i=1:length(irootiy1)
   if iyarc1(i)<=0
      diy1(i)=irootiy1(2,i);
   else
      diy1(i)=irootiy1(1,i);
   end
end

%%solve polynomial for distorted coordinates of line2
irootix2=ones(2,length(id2));
irootiy2=ones(2,length(id2));
for i=1:length(id2)
   pix2=[(1+iyarc2(i)^2/ixarc2(i)^2) 0 (-id2(i)^2)];
   piy2=[(1+ixarc2(i)^2/iyarc2(i)^2) 0 (-id2(i)^2)];
   if ixarc2(i)==0
   irootix2(:,i)=[0;0];
   irootiy2(:,i)=roots(piy2);
   else
     irootix2(:,i)=roots(pix2);
     irootiy2(:,i)=roots(piy2);
   end
end
dix2=ones(1,length(ixarc2));
for i=1:length(irootix2)
   if ixarc2(i)<=0
      dix2(i)=irootix2(2,i);
```

```
    else
        dix2(i)=irootix2(1,i);
    end
end
diy2=ones(1,length(iyarc2));
for i=1:length(irootiy2)
    if iyarc2(i)<=0
        diy2(i)=irootiy2(2,i);
    else
        diy2(i)=irootiy2(1,i);
    end
end

%%solve polynomial for distorted coordinates of line3
irootix3=ones(2,length(id3));
irootiy3=ones(2,length(id3));
for i=1:length(id3)
    pix3=[(1+iyarc3(i)^2/ixarc3(i)^2) 0 (-id3(i)^2)];
    piy3=[(1+ixarc3(i)^2/iyarc3(i)^2) 0 (-id3(i)^2)];
    if ixarc3(i)==0
    irootix3(:,i)=[0;0];
    irootiy3(:,i)=roots(piy3);
    else
    irootix3(:,i)=roots(pix3);
    irootiy3(:,i)=roots(piy3);
    end
end
dix3=ones(1,length(ixarc3));
for i=1:length(irootix3)
    if ixarc3(i)<=0
        dix3(i)=irootix3(2,i);
    else
        dix3(i)=irootix3(1,i);
    end
end
diy3=ones(1,length(iyarc3));
for i=1:length(irootiy3)
    if iyarc3(i)<=0
        diy3(i)=irootiy3(2,i);
    else
        diy3(i)=irootiy3(1,i);
    end
end

%Plot Overlap Triangles

figure('name','Overlap Triangles')
```

```
subplot(1,2,1)

plot(dx1,dy1,'k')
hold on
plot(dx2,dy2,'k')
hold on
plot(dx3,dy3,'k')


subplot(1,2,2)

plot(dix1,diy1,'k')
hold on
plot (dix2,diy2,'k')
hold on
plot(dix3,diy3,'k')

%%COPY TO EXCEL

x1=transpose(x1);
y1=transpose(yarc1);
x2=transpose(xarc2);
y2=transpose(yarc2);
x3=transpose(xarc3);
y3=transpose(yarc3);
xx1=transpose(ix1);
yy1=transpose(iyarc1);
xx2=transpose(ixarc2);
yy2=transpose(iyarc2);
xx3=transpose(ixarc3);
yy3=transpose(iyarc3);
```